

Geo-information Science and Remote Sensing

Thesis Report GIRS-2019-28



NEXT GENERATION PHENOTYPING WITH UAVS

FIELD PHENOTYPING OF WINTER BARLEY WITH DRONES DETECTING BROWN RUST

AUTHOR | FLEUR JONKER

DATE | 8TH OF JULY, 2019



NEXT GENERATION PHENOTYPING WITH UAVS

FIELD PHENOTYPING OF WINTER BARLEY WITH DRONES DETECTING BROWN RUST

AUTHOR | F.A. JONKER - 930923410040

SUPERVISORS | LAMMERT KOOISTRA & SANDER MÜCHER

M.SC. THESIS | LABORATORY OF GEO-INFORMATION SCIENCE AND REMOTE SENSING

REPORT NO. | GIRS-2019-28

**WAGENINGEN UNIVERSITY & RESEARCH CENTRE
THE NETHERLANDS**

JULY 2019



ABSTRACT

This thesis study focuses on the relevance of phenotyping efforts using unmanned aerial vehicle remote sensing platforms (UAV-RSPs), relative to conventional phenotyping efforts. Plant phenotyping aims at the acquisition of phenotypic information of plants or cells in different environments – as accurately and rapidly as possible. Major advances in plant phenotyping are required in order to improve plant characteristics linked to for example increased yield, productivity, biomass and resource efficiency. In the light of current trends as growing world population and climate change, these plant characteristics are of increasing importance.

Due to both the relative short time span and limited available data, the focus of this research has been placed upon one specific crop and plant trait. UAV-derived hyperspectral datasets containing the imagery of winter barley test field located in the province of Zeeland in The Netherlands were used to explore the usefulness of UAV data in the detection and categorization of the common fungal plant disease brown rust on winter barley. With this categorical information, insight in the susceptibility of this crop species for brown rust – a plant trait – is provided, helping breeders improve the genotype selection process. The spectral data used consists of 16 bands, covering wavelengths from 609 to 872 nm, and was produced on the 14th of July in 2017.

First step in this research was to determine how strong index values of existing vegetation indices are correlated to the validation brown rust scores – which were obtained by manual scoring. Indices included in the research are the ND 790/670, NDVI, NDRE, PVI and SAVI. For the index calculations, average reflections of the wavelengths in the red, red edge and NIR were used. For all correlations, a trend was evident. However, a strong variation on the y-axis indicates variability in the data. As this research is performed on an operational trial field, where operational scoring was conducted by the breeding company and many external variables were not accounted for – as they would be in an experimental set-up – this variability was expected. The PVI performs best with a Pearson correlation coefficient of -0.341 on the full dataset. After reducing the data to winter barley plots scored with a '1' for lodging – an external variable which was expected to influence the reflection significantly – the correlation between the index values and brown rust scores increased to -0.404. The R^2 values were respectively 0.116 and 0.164.

Secondly, the possibilities of constructing a spectral disease index (SDI) using lambda-lambda matrices were explored. These so-called redundancy plots were created to the methods of Aasen, Gnype et al. (2014) and visualize the R^2 values of index values based upon the index calculations using the bands indicated on the x- and y-axis and the brown rust scores. For these calculations the reflectances of all winter barley plots were used. The matrices were made for three different types of indices; normalize difference (1), orthogonal (2) and soil-adjusted (3). The best individual R^2 of 0.159 was found for the orthogonal index using the wavelengths of 833 and 872 nm; the corresponding correlation coefficient for these bands is -0.399. To further explore the potential of this index type, a random forest model using the indices based on the 30 best band combinations – with the highest R^2 values – as predictors was created. The predicted brown rust scores correlated with a value of 0.517 with the scores from the validation dataset.

From this research, several important conclusions can be drawn. Firstly, there was a lot of noise in the data; further research might best have a more experimental set-up. At least the variability in the validation data – partially caused by the date of data acquisition and bias that comes with the scorer(s) – should be accounted for. Secondly, the narrowband indices performed better than the existing vegetation indices calculated using the mean reflection over the bands in the red, red edge and NIR. Therefore, as stated in existing literature (Mahlein, Rumpf et al. 2013), multispectral imagery does not seem to be suitable for identification and quantification of specific diseases.

The results of this thesis are a step forward in the identification of important wavelengths and index types for the purpose of classifying the brown rust fungal disease on winter barley.

I would like to thank Lammert and Sander for their infinite patience and time, input and thoughtfulness in guiding me. This year has been like no other year for me. Without you both, writing this thesis would have felt like a heavy burden – particularly in the last long months. Thank you for ‘infecting’ me with your enthusiasm and optimism, I have enjoyed writing my thesis with you as my supervisors!

TABLE OF CONTENTS

1. Introduction	4
1.1 Research proposition	4
1.2 Context and background	4
1.2.1 Plant phenotyping.....	4
1.2.2 Field phenotyping and UAV-RSPs	5
1.2.3 Hyperspectral data and disease detection	5
2. Problem definition	7
3. Research objectives and questions	9
4. Literature study.....	10
4.1 Winter barley.....	10
4.2 Plant traits for breeding	10
4.3 Brown rust.....	11
4.4 Hyperspectral versus multispectral imaging.....	12
4.5 Spectral Vegetation Indices (SVIs).....	13
4.5.1 Types of SVIs.....	15
4.5.2 Hyperspectral narrowband vegetation indices.....	16
4.5.3 SVIs and plant diseases	16
4.6 Spectral disease indices (SDIs).....	17
4.7 Hyperspectral data – concepts, applications and analysis	17
4.7.1 Scale of application	17
4.7.2 Classification.....	18
4.7.3 Dimensionality reduction	18
4.7.4 PCA based band prioritization	19
4.7.5 Multi-Correlation Matrix strategy.....	19
5. Data description	24
5.1 Data collection and test site	24
6.2 Hyperspectral datasets.....	25
6.2.1 Data restrictions	26
6.3 In-situ data	26
6. Methodology.....	27
6.1 Pre-processing	27
6.2 Statistical analysis	28
6.2.1 Sub-research question one.....	28
6.2.2 Sub-research question two.....	29
7. Results.....	32

7.1 classification accuracy of existing spectral vegetation indices	32
7.1.1 Influence of brown rust on mean reflectance	32
7.1.2 Brown rust scores and existing vegetation indices	33
7.2 Constructing a spectral disease index (SDI) for winter barley brown rust	36
8. Discussion	39
8.1 Key findings & interpretations.....	39
8.2 Implications	40
8.3 Limitations	40
9. Conclusion.....	42
10. References.....	44
Glossary	47
Abbreviations	49
Abbreviations of statistical terms.....	51
11. List of figures	52
12. List of tables	54
13. Appendices.....	55
Annex A.....	55
Annex B.....	57
Annex C.....	58
Annex D.....	60
Annex E	62
Annex F	64
Annex G.....	65
Annex H.....	71
Annex I	76
Annex J.....	79
Annex K.....	80
Annex L	87
Annex M.....	89
Annex N.....	91

1. INTRODUCTION

In the world of today, requirements for food, feed and raw materials are increasing (EPPN 2017). Two major trends, the growing world population (1) and climate change (2), underline this. The current world population of 7.6 billion is expected to reach 8.6 billion in 2030 (UN 2017) and the discussion concerning climate change is ongoing; global interest in climate-conscious production increases.

The above mentioned trends emphasize the urge of developing sustainable plant production with a higher yield (1) and the use of limited resources (2). The scientific challenge of the coming years lies in making further progresses in molecular and genetic approaches and the quantitative analysis of plant phenotypes – the latter has already proven to be a major bottleneck (EPPN 2017).

A development that might be a very promising factor in making further progression in plant phenotyping efforts is the use of unmanned aerial vehicle remote sensing platforms (UAV-RSPs). These UAVs – equipped with various types of sensors – allow for high-throughput crop phenotyping, also called '*phenomics*'. However, these systems come with limitations as well; collected datasets need to be pre-processed and analysed before breeders can derive the information they need (Jones, Serraj et al. 2009). Development of successful methods to do this will vary with the crop type, sensor(s) used and plant traits of interest for particular phenotyping purposes.

1.1 RESEARCH PROPOSITION

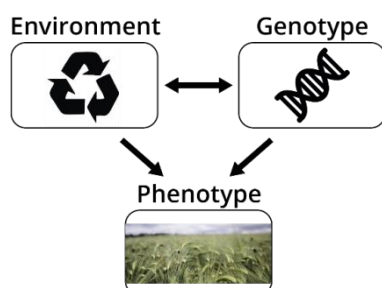
In this thesis, UAV-derived hyperspectral datasets containing the imagery of winter barley plots located in the province of Zeeland in The Netherlands will be used to explore the usefulness of UAV data in the detection and categorization of the plant disease brown rust – a common fungus – on winter barley. Detecting this plant disease and categorizing the plots with varying species of winter barley based on severity of infection, helps breeders to get insight in the susceptibility of the crop species for brown rust. Conventional detection and classification efforts of the brown rust disease are taken with the – though trained – naked eye of breeders. Ultimately, the information obtained by making UAV-phenotyping efforts helps to improve the companies' selection process.

1.2 CONTEXT AND BACKGROUND

This section briefly discusses the main concepts for further understanding of the background of the problem definition and research objectives/questions as defined in chapters 3 and 4.

1.2.1 PLANT PHENOTYPING

Plant phenotyping is a relatively “young” science, it is aiming at acquiring phenotypic information of plants or cells in different environments as accurately and rapidly as possible. It links genomics with plant ecopsychology and agronomy (EPPN 2017). When a genotype interacts with its environment, a functional plant body – or phenotype – develops from that (figure 2). This functional plant body has characteristics that determine its



performance, productivity, biomass, commercial yield and resource use efficiency (EPPN 2017). To improve one of these characteristics, firstly the relationship between environment, genotype and phenotype needs to be mapped thoroughly. Understanding the link between these concepts requires major advances in plant phenotyping (EPPN 2017). For this reason, plant phenotyping is a core activity of today's breeders and plant researchers.

Figure 1 | Relationship between the environment, genotype and phenotype.

1.2.2 FIELD PHENOTYPING AND UAV-RSPS

Crop science research is ultimately aimed at the maximization of the crop yield; breeding is largely directed to developing genotypes characterized with increased yield potential (Przulj, Momcilovic et al. 2014). Field phenotyping efforts for plant breeding are a critical component in the determination of the association of genomic and phenotypic information of crops and therefore play an important role within this science. According to White, Andrade-Sanchez et al. (2012) and Araus and Cairns (2014), field phenotyping is the ultimate expression of the relative effects of genetic factors, environmental factors and their interaction on critical production traits such as yield potential and tolerance to abiotic/biotic stress.

Crop traits (such as plant height, leaf color, chlorophyll content, sensitivity to diseases, biomass and yield) are traditionally acquired through techniques relying on manual sampling – which is both a time-consuming and a laborious activity (Furbank and Tester 2011, White, Andrade-Sanchez et al. 2012, Joshua, Genevieve et al. 2013), and thus costly.

The past years, alternative techniques for field based phenotyping have been considered, including ground- and field-based platforms. Though these platforms have important benefits (Annex B), there are some challenges that could limit their potential. A lot of these challenges can be addressed by using UAVs instead. For example, issues as non-simultaneous parameter measurement of different plots – this can take up to hours (1), vibrations that result from uneven terrain surfaces (2) and soil compaction (3) can be addressed by the replacing the ground-based platforms by high resolution, low altitude UAVs (Sankaran, Khot et al. 2015).

Unmanned aerial vehicle remote sensing platforms (UAV-RSPs), equipped with for example hyperspectral sensors or laser scanners allow for phenomics and are characterized by their non-destructivity, flexibility, convenient operation, on-demand access to data and high spatial resolution (Sankaran, Khot et al. 2015). Nevertheless, using UAVs in phenomics has its limitations as well. Think of non-operability during windy and/or rainy conditions, limited flight time or insufficient or unstable speed (Sankaran, Khot et al. 2015). In all cases, obtained datasets need to be – depending on the information that is desired – normalized, calibrated, validated and/or analysed for breeders to derive the information they need from the raw imagery that is collected (Jones, Serraj et al. 2009). When it comes to phenotyping efforts for breeding purposes, calibration might not always be strictly necessary; absolute values are of lesser interest than relative differences among genotypes (Jones, Serraj et al. 2009) – upon which decisions on selection are ultimately made.

In addition to the above mentioned, UAV-RSP-based sensing is as well applied to easily detect the influence of other factors as soil compaction, field anomalies due to earlier production practices – deficit of certain nutrients, presence of weeds and soil variability (Sankaran, Khot et al. 2015). On top of that, apart from being an alternative to manual field and ground-based platform phenotyping techniques, UAV-RSPs may also account better for environmental variations – think of rainfall, soil characteristics, temperature, weather – than earlier techniques. This way, selection efficiency increases (Sankaran, Khot et al. 2015).

Annex B provides an overview of main advantages and disadvantages of manual sampling, sampling using ground-based platforms and UAV-RSP sampling. Annex C provides application examples of high-resolution aerial sensing in field phenomics. Note that many of these applications and technologies - in particular those of the plant biotic stress – are still under development.

1.2.3 HYPERSPECTRAL DATA AND DISEASE DETECTION

Within agricultural sites, remote sensing can be very useful to monitor the heterogeneity and vitality of crops. In case of a fungal infection, detection at an early growth stage is very important to successfully address the disease (Tischler, Thiessen et al. 2018). Knowledge on spatio-temporal dynamics of – fungal – crop diseases allows for the implementation of site-specific fungicide applications (Franke and Menz 2007), reducing the impact on the crop yield. The past years, advances have been made in detecting and identifying plant diseases using

hyperspectral data (Mahlein, Oerke et al. 2012, Mahlein 2016, Thomas, Kuska et al. 2018). As significant information on a particular disease might be present on a narrow part or band of the spectrum, hyperspectral imagery is very suitable for the development of spectral disease indices (SDIs; Mahlein, Steiner et al. 2012). In the latter study, the authors have detected and differentiated several diseases through spectral signatures of sugar beet leaves. Krichna, Sahoo et al. (2014) have used hyperspectral reflectance data to classify winter wheat in the fields of the Haryana and Punjab states of India on yellow rust – a fungal disease – infection. They measured reflectances in the spectral range of 350-2500nm – visible near-infrared (VNIR and shortwave infrared (SWIR), using a spectroradiometer. Based on the spectral data, a robust model was derived by means of partial least squares (PLS) regression showing strong correlation and low error. Three highly significant spectra – 428 nm, 670 nm and 1399 nm – were identified for this particular use case. Next to the above-mentioned leaf-level studies, increasingly there are examples of disease detection using airborne, high resolution hyperspectral imagery. For instance, in order to detect Verticillium wilt – a disease that can only be controlled if detected in early development stages – on olive trees, Calderón, Navas-Cortés et al. (2015) used linear discriminant analysis (LDA) and support vector machine (SVM) methods on both high-resolution thermal and hyperspectral imagery covering a 3000 ha commercial olive area. They found that, among other indices, normalized canopy temperature, chlorophyll fluorescence, carotenoid and disease indices perform well as indicators for early and advanced stage infection of Verticillium wilt. Methods of other, smaller scale studies (Calderón Madrid, Navas Cortés et al. 2013) have shown to be valid for the larger area of this study.

2. PROBLEM DEFINITION

For plant breeders, UAV-RSPs offer very promising alternatives to traditional techniques to acquire plant traits. Still, a lot of the acquired data products are left to be validated – on the basis of ground data/measurements. Before that, obtained imagery needs to be analysed to develop methods to derive information from them (Furbank and Tester 2011, Zaman-Allah, Vergara et al. 2015). In addition to deriving individual plant traits, it should be determined which (combination of) plant traits or varieties correlate best with the grain yield of particular crops (Lalic 2006, Miroslavljević, Pržulj et al. 2015). The latter however, falls outside the scope of this thesis. UAV-obtained data need to be processed, validated and analysed in order to explore the usefulness of integrating this type of data in the workflow of breeders. Subsequently, the UAV-derived plant trait data can be correlated to the harvest yield. The main issue is that proper classification methods for particular plant traits on the basis of UAV-derived data are still to be identified or constructed – in many cases per crop and per trait, as particular traits require different sensors for detection and/or classification (Yang, Liu et al. 2017). As relevant plant traits for breeding have varying parameters, different techniques and instruments are needed to collect data on them. In some cases hyper- and/or multispectral data contains relevant information – when mapping crop physiology for example, whereas in other cases it might be LiDAR data – suitable to measure crop traits such



Figure 2 | WENR flying with the UAV-RSP above the winter barley plots at the location of Rilland (Limagrain).

as height. A combination or fusion of different techniques or instruments for trait identification and classification might be theoretically the most accurate approach in many cases, commercial companies such as Limagrain however might prefer the use of merely one instrument – a cost-benefit analysis will determine the best choice in this.

In the light of the current technical developments, Limagrain breeding company is interested in the possibilities that UAV-RSPs offer to their crop trait classification efforts. The company collaborates with Aurea Imaging and Wageningen Environmental Research (WENR) in a public private partnership to explore the potential of integrating the use of UAV-RSPs into their phenotyping activities – for more information see Annex A. The breeding activities of Limagrain cover the phenotyping of several crops, among which is winter barley. This cultivated grain belongs to the *Poaceae* or grass family and varieties are known to be susceptible to the fungal plant disease of barley brown rust – *Puccinia hordei* – to varying degrees

Attacks of brown rust are irregular (figure 4) and can ultimately cause early senescence of the crop (Melville 1979). Usually, summer varieties of barley are more likely to get affected by brown rust than winter barley; especially during warmer growth seasons, the fungus is prevalent. With the current climatological developments, the relevance of early detection of winter barley brown rust increases. A heavily affected crop might lead to a reduction of 30% of the so-called Thousand-Grain-Weight (TGW) and results in a decrease of the amount of grains per ear (BASF 2018). Based on visible symptoms, the infection can be divided into three stages; flecking (1), sporulation (2) and green island (3). The tables D1-D3 in Annex D present the results of a study by Scholes and Farrar (1987), showing the changes in distribution of fungal mycelium and concentration of chlorophyll in relation to the three visible symptoms of brown rust. The study showed that particularly at high pustule density, the reduction in the concentration of chlorophyll as a result of brown rust infection of leaves is present. This loss occurs mainly in regions between the pustules and at a later stage green islands form wholly as a result of the synthesis of net chlorophyll.

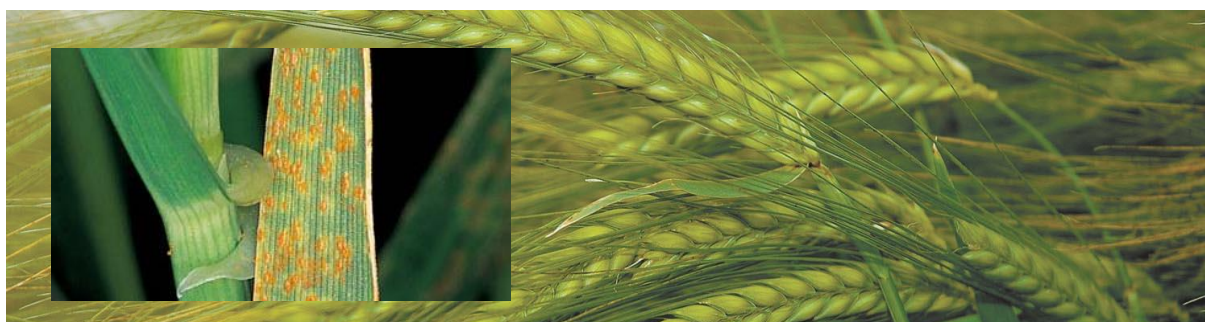


Figure 3 | Healthy winter barley versus brown rust infected leaves (source: Bayer Crop Science, FarmingUK.com).

Fungal diseases affect crops physiologically after infection. Unfortunately, the first changes in the plant are not visible with the naked eye (Berryman, Eamus et al. 1991), which leaves breeders and arable farmers blind during this initial phase of the disease development. However, at least some of these physiological changes are spectroscopically measurable – a number even at an early stage (Berryman, Eamus et al. 1991). This knowledge underlines a relevant potential advantage of adopting hyperspectral data for detection and classification efforts compared to conventional – manual – scoring of brown rust. Hyperspectral data might allow Limagrain and other breeding companies for development of an “early warning” methodology. A specific study on the characteristics and spectral measurability of winter barley brown rust should be conducted to determine whether constructing such a methodology is feasible.

3. RESEARCH OBJECTIVES AND QUESTIONS

The main objective of this research is to explore the relevance of phenotyping efforts using UAV-RSPs relative to conventional phenotyping efforts. As the time span is relatively small, to meet this objective focus has been placed on one specific crop and plant trait. This thesis will be an exploration of the relevance of hyperspectral data in determining the susceptibility of different winter barley varieties for brown rust.

This research can further be divided in three sub-objectives. The first objective is to determine whether existing vegetation and disease indices might offer accurate detection and classification possibilities for brown rust on winter barley. The second objective is to investigate the possibilities of constructing a spectral disease index (SDI) for winter barley brown rust using band prioritization and decorrelation methods. Thirdly, two hyperspectral datasets are compared; do they allow for characterization of brown rust over time? The objectives are listed below:

- I. Study the correlation between brown rust infection severity and common vegetation indices.
- II. Explore the possibilities of constructing a spectral disease index (SDI) for winter barley brown rust using different band prioritization, selection and decorrelation methods.

The main research question for this thesis is defined as follows:

MRQ : What is the relevance of phenotyping efforts using UAV-RSPs relative to conventional phenotyping efforts for the detection of winter barley brown rust?

In order to answer the main research question, the following sub-questions have been defined:

SRQ1 : How strongly are the index values of existing vegetation indices correlated to the brown rust scorings?

SRQ2 : What are the possibilities of constructing a spectral disease index (SDI) for winter barley brown rust using band prioritization methods?

4. LITERATURE STUDY

In this chapter, some relevant – background – knowledge and literature is gathered and reviewed. The first paragraph includes a short characterization of winter barley, the crop which will be of interest in this thesis. Paragraph 4.2 presents some more background information and literature on the concept of phenotyping and the emerged role of UAVs within this activity is described. The last paragraph is dedicated to a short introduction of plant traits relevant for breeding in general and the plant trait of winter barley brown rust in particular.

4.1 WINTER BARLEY

In this thesis, focus has been placed on datasets obtained on winter barley plots. A very brief description of this grain is given in this paragraph.

Barley (*Hordeum vulgare*) is a cultivated grain, belonging to the *Poaceae* or grass family (figure 4). Barley has one of the first and best known domestication processes, which started already 10.000 years ago (Zohary 1988); particularly in Eurasia where the favourable temperate climate is present. *Hordeum vulgare* has an annual – summer barley – and biennial variety. In order to be able to flower in the second half of May, winter barley must have had enough cold during the winter. Usually, summer barley blooms a bit later. In the Netherlands, Winter barley is sown in the period end of September – mid-October, whereas summer barley is sown in the second half of February.

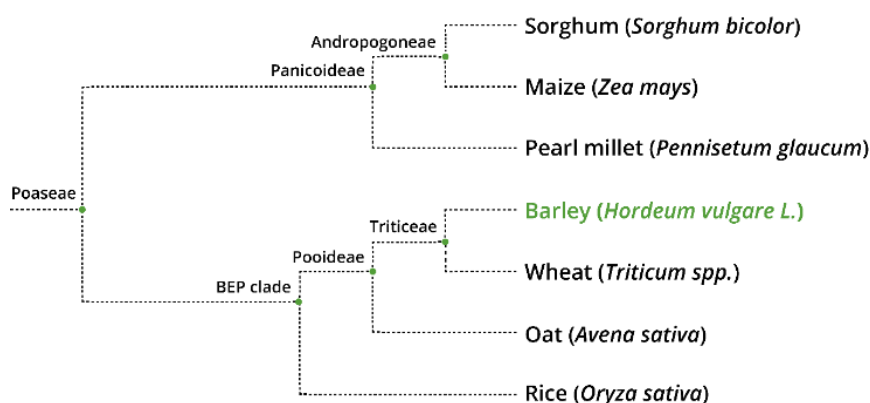


Figure 4 | Phylogenetic relationships among seven crop plants among which barley (*Hordeum vulgare*). Tree is built based on information from the Taxonomy database of the National Center for Biological Information (ncbi.nlm.nih.gov/taxonomy).

4.2 PLANT TRAITS FOR BREEDING

For breeding purposes, there are certain important plant traits to consider. As the main goal of breeding activities is the maximization of (grain) yield, it is the most important and universal – but also complex – trait in cereal breeding (Miroslavljević, Pržulj et al. 2015). Numerous plant traits have shown a significant correlation with harvest potential. Development of genotypes characterized with the increase of yield potential – high-yielding genotypes, wide adaptation and high responses to agronomic inputs are core activities of modern day barley breeding (Pržulj, Momcilovic et al. 2014).

The grain yield is depending upon a combination of a multitude of different plant traits. Proper understanding and analysis of the relationship between these traits is therefore essential for establishing an effective breeding programme (Yan and Kang 2003). Naturally, not all traits are correlated to harvest potential (yet) and determining the influence of every single trait is an immense – and likely unnecessary – task. Examples of agronomic and technological plant traits that are generally known to have a significant effect on barley grain yield and quality

include lodging, plant height, thousand kernel weight, hectolitre mass, grain protein content, susceptibility for diseases, yield, brackling, lodging, etc.

Thereby, assuming that direct selection for a certain trait could have a negative effect for other traits is reasonable (Lalic 2006). In fact, Lalic (2006) found that the selection for shorter stem length of barley had a negative effect on grain yield per plot (-18.99%), also the number of grains per spike dropped with 7,14%. In the same research, selection for higher grain yields per plot caused both an increase in stem length – which is a negative effect - and harvest index – a positive effect. This example emphasizes the fact that selection processes are very complex and that simply selecting on random traits related to a higher harvest index is not a guarantee for a successful breeding process.

4.3 BROWN RUST

Barley brown rust is caused by the fungus *Puccinia hordei* and should not be confused with brown rust of wheat (*Puccinia recondite*) – cross-infection between the two does not occur. The disease can affect various species of winter and spring barley. The occurrence of brown rust is irregular, however attacks – of which the course is influenced by the weather – can be very damaging (Melville 1979). Brown rust can only survive on living plants, however winter and spring barley can be infected by uredospores.

Depending on the resistance of the barley species, brown rust can ultimately cause early senescence of the crop. Visible symptoms start with the appearance of fungal growth on the leaves as orange-brown pustules (figure 7). Later, necrotic (dead) areas will loom up and leaves will start to wilt. Eventually, dead leaves will show a yellowed tint (CABI 2018). As illustrated by figure 7, the pustules spread irregularly, which makes it possible to distinguish brown rust from another fungus; yellow rust or *Puccinia striiformis*. Yellow rust is characterized by the fact that it's pustules occur in stripes as the disease progresses. The time needed for brown rust pustules to develop varies from 60 days when temperatures are around 5 °C and six days when the temperature is about 25 °C. Brown rust can affect the leaves, leaf sheaths and ears – in particular the awns of the ears.

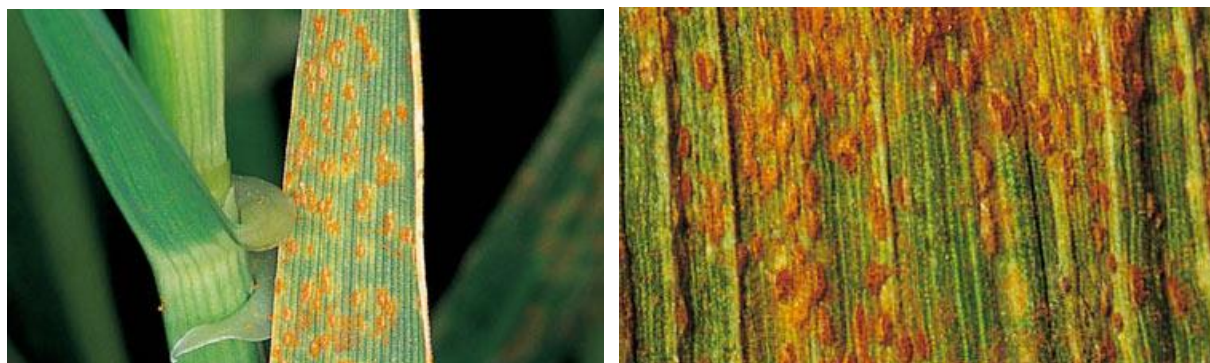
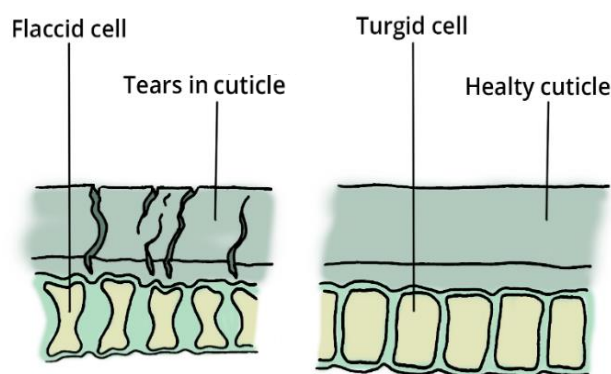


Figure 5 | Leaves infected with barley brown rust (Bayer Crop Science).

Brown rust is known to have a late-season development – this is related to both the temperature and time it takes for inoculum to build up. Though, especially when the winter has been relatively mild, brown rust can loom earlier. In the seasons of spring and summer, the fungus normally appears during the tillering and stem extension stages. However, usually the occurrence remains only slight until flag leaves emerge (Melville 1979). This is also the reason why brown rust rarely affects the plant size or amount of fertile tillers produced – as both are determined in early growth stages.

Brown rust causes shrivelled and/or undeveloped grain and therefore has a negative effect on both the quality of the grain and the grain yield (Melville 1979). None of the barley varieties are immune for brown rust, however they differ in their susceptibility to the disease; several breeding programmes aim at the development of species with a high brown rust resistance.



After the crop is infected, some spectroscopically measurable physiologic changes will occur. Firstly, five days after infection the cuticles – an extracellular hydrophobic layer covering the aerial epidermis of land plants – start to tear (Berryman, Eamus et al. 1991). This causes a decrease in turgor of the cells below; leaves lose their ability to maintain a favourable water status (figure 6).

Figure 6 | A leaf's lost ability to maintain favourable water status attributed by tears in the cuticle - which has a protective and hydrophobic function when intact (source: author).

Also, the blue and red absorbing chlorophyll content decreases as a result of the infection. Thirdly, as the photosynthesis process starts when sunlight is hitting chloroplasts, the photosynthesis decreases as well. This causes a final spectroscopically measurable change to occur; an increase in leaf temperature. In figure 7, the differences in the spectral signatures of healthy and rust infected barley leaves is visualized. The most apparent change is the increase in reflectance from the visible to the SWIR as a leaf gets infected.

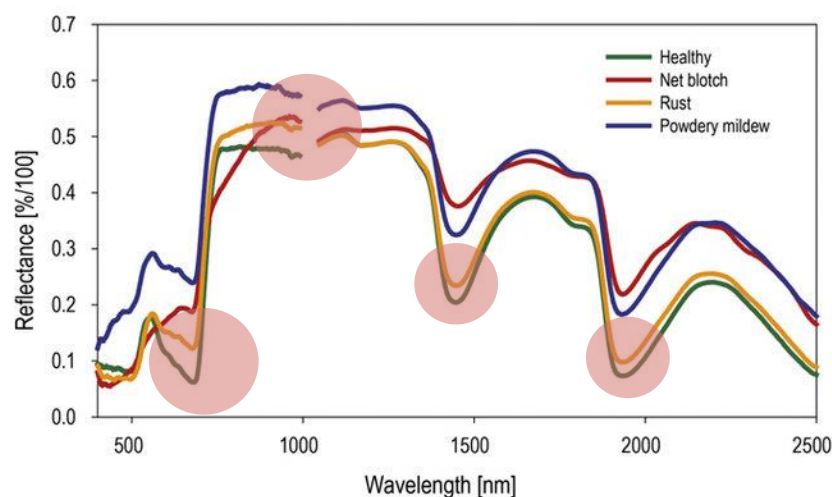
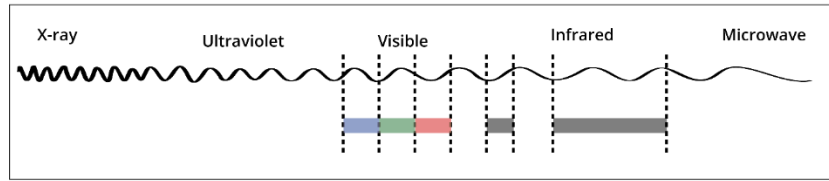


Figure 7 | Spectral signatures of sugar beet in healthy or diseased condition (source: Anne-Katrin Mahlein, Institute of Sugar Beet Research, University of Göttingen). Divergent reflectances marked with red circles.

4.4 HYPERSPECTRAL VERSUS MULTISPECTRAL IMAGING

Spectral imaging falls under the branch of spectroscopy, in which interactions between matter and electromagnetic radiation is studied. Hyperspectral imaging is different from multispectral imaging, as both techniques use a different number and width of spectral bands. Figure 8 provides a schematic overview of the differences between the two imaging types. Hyperspectral imaging uses more bands – tens to thousands – and narrower band widths – of one to several nanometres – than multispectral imaging in the same spectral range (Thenkabail and Lyon 2012). As an example, a sensor with merely 25 bands can be considered hyperspectral if it covers a range of 250 nm – each band being 10 nm wide, whereas a sensor with the same amount of discrete bands covering multiple parts of the spectrum – VIS, NIR, SWIR, MWIR, LWIR, is considered multispectral. The pixels within a hyperspectral image are typically described as data vectors, the entire image as an image cube (figure 9).

Multispectral imaging - small selection of wide bands



Hyperspectral imaging - hundreds-thousands of narrow bands

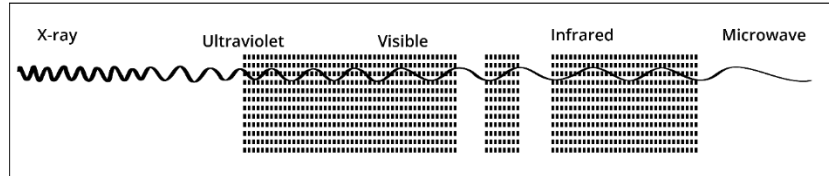


Figure 8 | Illustrative example of hyperspectral and multispectral imaging (source: author).

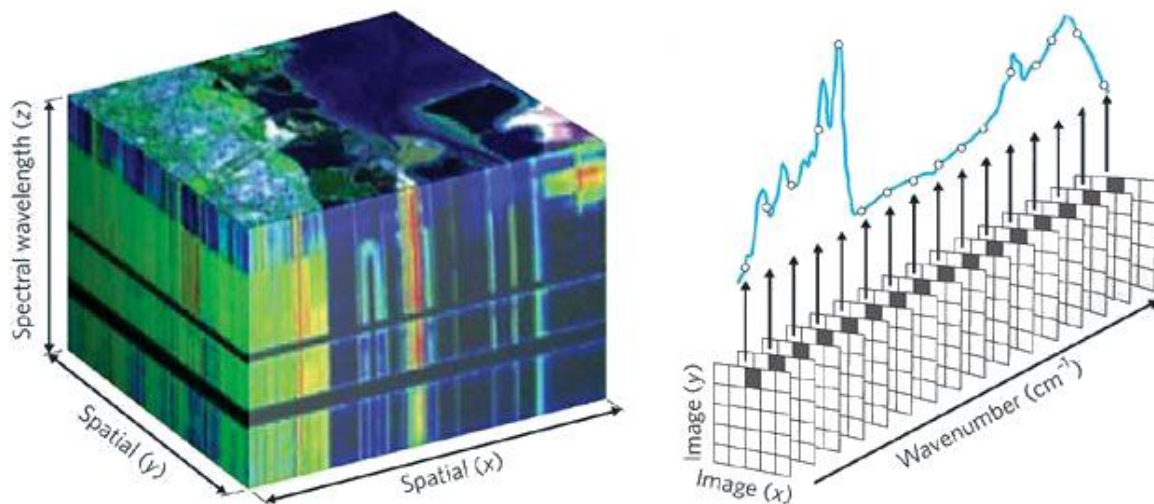


Figure 9 | Example of an hyperspectral image cube with two spatial dimensions (x , y) and multiple wavelengths (z) (Bannon 2009).

4.5 SPECTRAL VEGETATION INDICES (SVIS)

In remote sensing, spectral vegetation indices are widely used, they are simple and robust techniques to extract quantitative information on the amount of vegetation or greenness for every pixel in an image (Chuvieco 2016). It is assumed that the combined interaction between a small number of wavelengths sufficiently describes the biochemical or biophysical interaction between light and matter (Thenkabail and Lyon 2012). Typically, they involve the spectral transformation of a minimum of two spectral bands; one in the Red (R) and one in the Near-Infrared (NIR). The R (0.6-0.7 μm) being the chlorophyll-absorbing region and the NIR (0.7-1.1 μm) the non-absorbing. In the latter one, significant leaf scattering is present – which is quite unique to vegetation that is photosynthetically active (Chuvieco 2016). Figure 10 illustrates the difference in reflection in the NIR and IR between healthy (green) vegetation and senescent (brown) vegetation. The soil reflectance line indicates that there is almost no difference between the amount of reflectance in the R and (N)IR for soil pixels.

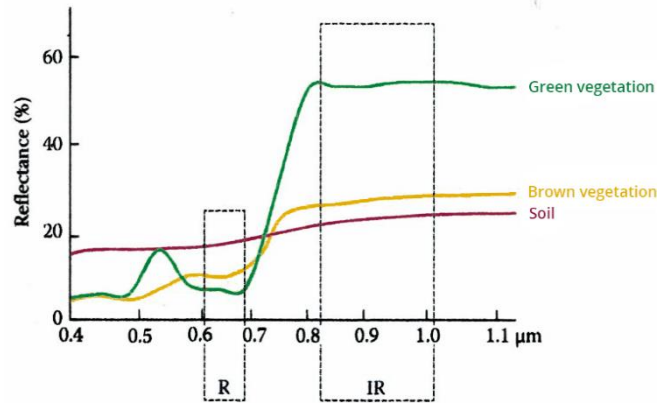


Figure 10 | Typical spectral signatures of healthy (green) vegetation, senescent (brown) vegetation and the soil. The R and NIR regions are indicated; most vegetation indices are based on these two bands (Chuvieco 2016).

Besides the determination of greenness and amount of vegetation of a feature of an image, SVIs are also used as proxy measurements of biophysical variables such as the Leaf Area Index (LAI), grains volume fraction (Fv), biomass and photosynthesis (Kerr and Ostrovsky 2003, Pettoirelli, Vik et al. 2005).

A SVI is best seen as an “integrator” of many variables that as a composite determine photosynthetically active vegetation signal (Baret and Guyot 1991, Huete, Didan et al. 2002). For this reason, differentiation between the multiple variables responsible for changes in the composite signal – the SVI – is generally not possible (Chuvieco 2016).

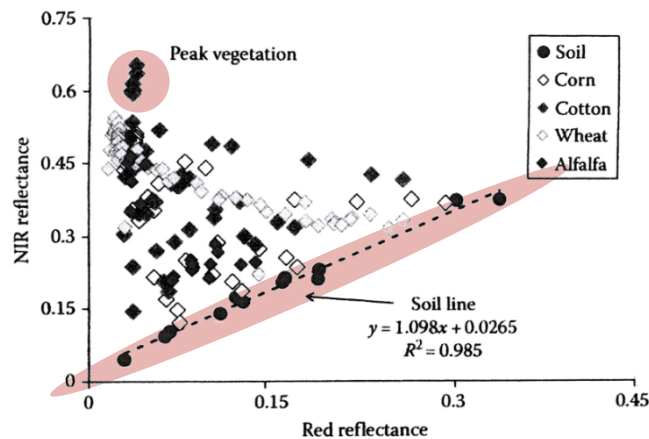


Figure 11 | Structure of vegetation spectra plotted in the R-NIR reflectance space (Source: Alfredo Huete). The peak vegetation – indicating very dense green vegetation – and the soil line are marked in red. Note that direction of the soil line depends on the dataset.

When vegetation spectra are plotted in Red and Near-Infrared space, points show a triangular pattern (figure 13). From this plot, several definitions can be made. Firstly, there is the soil line, extending linearly outward from the origin and where R and NIR reflectance is more or less equal – no vegetation is present. See equation 2.1 for the equation of the soil line, where a and b are respectively the best fit soil line slope and intercept for a range of soil backgrounds at different stages of wetting and drying, roughness and litter content (Chuvieco 2016). Closest to the origin water pixels are found, followed by dark soil and bright soil (furthest away from the origin) pixels.

$$NIR_{soil} = a * RED_{soil} + b$$

(4.1)

Secondly, the most densely vegetated pixels – “peak vegetation” – are characterized by a high reflectance in the NIR and low reflectance in the R.

4.5.1 TYPES OF SVIS

There are several types of SVIs, all related to some extent with various vegetation canopy properties, but significantly different in their depiction of greenness – and therefore their usefulness and complementariness (Chuvieco 2016). A ratio-based SVI – or ‘simple ratio’ – is created by rationing of the NIR with the R band. See the formula below, where ρ_{NIR} and ρ_R indicate the reflectance in the near-infrared and the red per pixel.

$$SR = \frac{\rho_{NIR}}{\rho_R} \quad (4.2)$$

The well-known Normalized Difference Vegetation Index (NDVI) is a functional variant of the simple ratio, ranging from -1 to 1 (Chuvieco 2016). Pixel values above 0,2 indicate living green vegetation (formula 4.3).

$$NDVI = \frac{(\rho_{NIR} - \rho_R)}{(\rho_{NIR} + \rho_R)} \quad (4.3)$$

The second type of SVIs are the optimized vegetation indices. Notwithstanding the usefulness of the NDVI for vegetation studies, it also responds to spatial and temporal variations in soils and atmospheric influences (Chuvieco 2016). The Soil Adjusted Vegetation Index (SAVI) is an example of an index which allows for the influence of the backscattered soil signal to be removed (Huete 1988). A parameter L , which is related to the differential optical penetration of R and NIR light through a vegetation canopy, is incorporated in the formula. L is the adjustment factor (Chuvieco 2016), see formula 4.4.

$$SAVI = \frac{\rho_{NIR} - \rho_R}{\rho_{NIR} + \rho_R + L} (1 + L) \quad (4.4)$$

Today, many variations on the SAVI are used. Examples are the transformed SAVI (TSAVI), which is based on SAIL model simulations (Verhoef 1984), the generalized SAVI or GSAVI (Gilabert, González-Piqueras et al. 2002), the modified SAVI (MSAVI), by Qi, Chehbouni et al. (1994). Today, the most popular soil-adjusted vegetation index is the MSAVI2, as it does not make use of the soil line and soil brightness correction factor.

The third group consists of orthogonal-based SVIs. These indices measure the contrast between the R and NIR spectral regions by the subtraction of linearly combination of R and NIR bands (Chuvieco 2016). The most elementary example of such an index is the DVI, the Difference Vegetation Index, which simply extracts the R from the NIR. Another example is the PVI or the Perpendicular Vegetation Index (Richardson 1977), which calculates the orthogonal distance of a certain pixel to the soil line. See formula 4.5, where a and b are respectively the slope and intercept of the soil line.

$$PVI = \frac{(\rho NIR - a * \rho R) - b}{(1 + a^2)^{\frac{1}{2}}}$$

(4.5)

The last (large) group of indices are the fluorescence indices. These indices are based on chlorophyll fluorescence and are more directly associated to diurnal changes in photosynthetic activity than common vegetation indices such as the NDVI – which are in fact associated with canopy structure (Chuvieco 2016).

Naturally, there are other spectral indices using varying combinations of spectral bands. Those indices can be used to emphasize different image features such as snow – the Normalized Difference Snow Index (NDSI) is used for snow monitoring (Chuvieco 2016). Also think of the detection of burned areas or discrimination of plant water content and/or diseases.

4.5.2 HYPERSPECTRAL NARROWBAND VEGETATION INDICES

Multispectral imagery has traditionally been used for agriculture remote sensing. Thanks to technological sensor developments of the past few decades, hyperspectral remote sensing imagery has started to provide agriculture with more opportunities for information extraction on a field level (Thenkabail and Lyon 2012). Hyperspectral images offer the potential to build more refined vegetation indices by the use of distinct narrow bands and improvement of the indices for the correction of the effects of soil background (Peng, Ruiliang et al. 2003).

Hyperspectral vegetation indices (HVIs) nowadays are developed and used for varying applications – not merely in the agricultural field. The most simple indices are based on individual bands and are suited to predict biomass, LAI (Elvidge and Chen 1995), nitrogen (N) stress (Daughtry, Walthall et al. 2000), chlorophyll concentrations (Blackburn 1998, Broge and Mortensen 2002) and more. A few examples of biophysical and biochemical properties are given in table 1.

Table 1 | Examples of biophysical and biochemical variables present in crops which are measurable through hyperspectral remote sensing (Mahlein 2010).

	Property	Relevant index wavelengths	Explanatory notes
Biophysical	LAI/crop cover (No units/%)	Red + NIR	Red; absorption region NIR; mesophyll scattering region
	Biomass (kg m ⁻¹)	350-2500nm	Similar effects on spectral characteristics as LAI
Biochemical	Nitrogen (%N)	VIS+SWIR SWIR (absorption region)	
	Chlorophyll content (µg cm ⁻²)	450, 680 and 700-740nm	450nm; chlorophyll absorption in the blue 680nm; chlorophyll absorption in the red 700-740nm; displacement of the red edge inflection point
	Leaf water content (%)	760, 970, 1450, 1940 and 2950nm	Wavelengths are water absorption regions

4.5.3 SVIS AND PLANT DISEASES

The past years, several SVIs have been studied by scientists and researchers with the aim to detect plant diseases (Moshou, Bravo et al. 2004, Hillnhütter, Mahlein et al. 2011, Zhang, Pu et al. 2012). Plant diseases – which have an effect on the pigments and structure of the organism – can be detected using spectroradiometric and remote sensing techniques (Zhang, Pu et al. 2012). Remote sensing technologies potentially provide an automatic and

objective alternative to visual disease assessment of plant diseases (Hillnhütter, Mahlein et al. 2011, Mahlein, Oerke et al. 2012). The potential of spectral sensor systems for the detection of fungal diseases – such as the brown rust fungus – is proven in several studies: see for example Hillnhütter, Mahlein et al. (2011), Mahlein, Oerke et al. (2012), Mahlein, Steiner et al. (2010), Mahlein, Steiner et al. (2012), Moshou, Bravo et al. (2004) and Steddom, Bredehoeft et al. (2005).

4.6 SPECTRAL DISEASE INDICES (SDIS)

As mentioned in the previous paragraph, SVIs are commonly used to analyse and detect changes in biophysical and biochemical variables – but also physiological changes – in vegetation. As plant diseases affect these variables, SVIs have the potential to detect plant diseases. However, the identification and quantification of specific diseases on the basis of common SVIs has not been done so far – as these indices lack disease specificity (Mahlein, Rumpf et al. 2013). For this, specific – hyperspectral – data analysis methods and algorithms on diseases are needed. Since diseases are known to have their own characteristic spectral signature (figure 9), combining different – narrow – wavelength bands in a spectral disease indices (SDIs) design allows for specific disease detection by the use of spectral sensors (Mahlein, Rumpf et al. 2013).

4.7 HYPERSPECTRAL DATA – CONCEPTS, APPLICATIONS AND ANALYSIS

This chapter contains a brief overview of relevant concepts, applications and statistical analysis methods concerning the hyperspectral data used for the use case of this thesis. The first paragraphs will handle important applications and characteristics of hyperspectral imagery. In the last paragraphs, some statistical steps that need to be traversed when constructing a (hyper)spectral disease index (SDI) are appointed

4.7.1 SCALE OF APPLICATION

Hyperspectral remote sensing is used for various applications, among which plant disease detection. Before taking hyperspectral images, the measurement scale needs to be defined. Thomas, Kuska et al. (2018) presented vision of a multi-scale model that integrates observations of the plant-pathogen interaction from the microscope up to airborne imaging (figure 12).

Metabolic changes during plant-pathogen interactions are measured on a tissue and leaf scale, resistance phenotyping and disease detection occur on a leaf, single plant and canopy scale (Thomas, Kuska et al. 2018). In practice, the experiments on the lowest scales are performed in the laboratory in the context of basic research and to a certain extent phenotyping as well. The scale of tissue is merely achieved by using hyperspectral microscope systems. More practical applications such as phenotyping and precision farming require measurement data from greenhouses and fields on leaf, single plant and canopy scale (Thomas, Kuska et al. 2018).

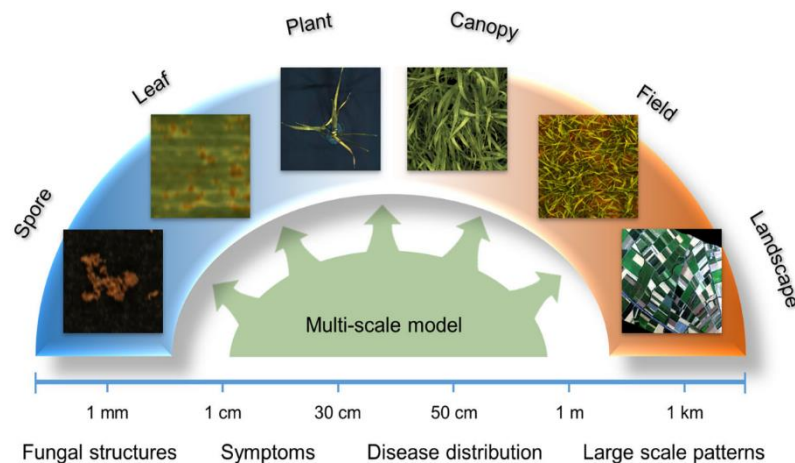


Figure 12 | Multi-scale model integrating observations of the plant-pathogen interaction from the microscope up to airborne imaging (Thomas, Kuska et al. 2018).

As barley brown rust (caused by the fungus of *Puccinia hordei*) can be detected on symptoms showing from a leaf level, it does not necessarily have to be detected on the observation of fungal spores on the tissue level. Though laboratories provide the most stable environmental conditions for hyperspectral experiments, these measurements can be performed in greenhouses or even the field as well (Thomas, Kuska et al. 2018). Fields allow for large-scale applications, for which the need is particularly prominent in applications such as plant breeding and non-invasive disease detection (David, Jose et al. 2014, Mahlein 2016).

4.7.2 CLASSIFICATION

Hyperspectral sensors can image areas with hundreds of different contiguous wavelength ranges, making the identification and classification of the composition of various materials on the land surface possible (Chein, Qian et al. 1999, Chuvieco 2016). In many areas, such as agriculture, minerology, surveillance, chemical imaging and automatic target recognition, hyperspectral data is becoming increasingly important as a classification tool (Chein, Qian et al. 1999). The high dimensionality of the hyperspectral data however, has its disadvantages as well (Chein, Qian et al. 1999); an increased computational complexity of classification (1), a negative impact of highly correlated features on the classification accuracy (2) and the Hughes effect (3), also having a negative impact on the classification accuracy when the number of training samples is insufficient for the amount of features that need to be classified. Adding features in this case can have a considerably negative impact on the accuracy of classification (Chein, Qian et al. 1999).

4.7.3 DIMENSIONALITY REDUCTION

As a significant amount of the hyperspectral data is correlated, it is possible to compress the data by removing redundant spectral information present in the multiband images – called dimensionality reduction – without losing a significant amount of original information (Chuvieco 2016). Eliminating bands to reduce computational cost, facilitate information representation, improve classification accuracy and accelerate knowledge discovery is a popular approach (Chein, Qian et al. 1999, Chuvieco 2016).

Dimensionality reduction methods can be broadly divided into feature extraction (1) and feature selection (2). Feature extraction methods are known to transform original data into a projected space. These methods include for example projection pursuit (PP), principal component analysis (PCA) and independent component analysis (ICA) (Preet 2015). Feature selection methods are used in an attempt to identify a subset of features containing fundamental characteristics of the data (Preet 2015); they are often preferred over feature extraction – as the latter method involves a transformation of the data, which might cause crucial information to be compromised

and distorted. The vast majority of unsupervised feature selection methods are based on feature ranking, in which an objective matrix is constructed and evaluated on the basis of a variety of criteria such as information divergence, maximum-variance principal component analysis (MVPCA) and mutual information (MI) (Preet 2015).

There are various feature selection methods for hyperspectral data, including the SVM recursive Feature Elimination (SVM-RFE), the Correlation based Feature Selection (CFS), Minimum Redundancy Maximum Relevance (MRMR) feature selection, Random Forests and a band prioritization scheme on the basis of Principal Component Analysis (PCA) and classification criterion (Chein, Qian et al. 1999, Preet 2015). Generally, these methods rank features on the basis of the comparison of information from the spectral bands and the ground truth or reference map (Preet 2015). The ground truth is based upon existing – a priori – knowledge on the spectral signatures of particular common (Preet 2015).

4.7.4 PCA BASED BAND PRIORITIZATION

The Principal Component Analysis (PCA) is one of the most commonly used feature selection methods. It transforms the original data into principal components, which have a projection that shows maximal variance (Preet 2015).

Chein, Qian et al. (1999) have presented a band-selection method that comprises a band prioritization and a band decorrelation. The band prioritization includes the prioritization of all bands according to the contained information to be used for classification. This, followed by a selection of bands based on their associated priorities. As the spectral correlation is not considered in the band prioritization (Chang 1997), they proposed a decorrelation using the divergence to decorrelate the prioritized bands. For the band prioritization, Chein, Qian et al. (1999) proposed an eigenanalysis-based method, exploiting its full usefulness by proposing PCA-based criteria and classification-based criteria. They revisited the band-prioritization approach of Te-Ming, Chin-Hsing et al. (1998), who constructed a loading-factors matrix via the eigen or spectral decomposition of an appropriate matrix, in which the loading factors were used to rank the priority of each band. The classification accuracy was determined by the number of bands that were selected – in decreasing order of priority. Additionally, Chein, Qian et al. (1999) propose two eigenanalysis-based criteria for band prioritization; the PCA-based criteria (1) and the classification-based criteria (2). For the PCA-based criteria they considered the maximum-variance PCA (MVPCA; 1) and the maximum-SNR PCA (MSNRPCA; 2). Two classification-based criteria were derived as well: the minimum-misclassification canonical analysis (MMCA) – also known as the Fisher's discriminant analysis (1), and orthogonal-subspace (OSP) criteria (2). The sum of the loading factors that are produced by the bands in the selected band subset determine the classification power of a certain band (Chein, Qian et al. 1999). By dividing the classification power of the selected band subset by all bands that are being used, a band-power ratio for band selection can subsequently be defined (Chein, Qian et al. 1999). After prioritization of all bands, a divergence-based decorrelation follows in order get rid of either redundant or insignificant bands. In case there are two bands that diverge below a certain given threshold, the band with the lowest priority will be removed. Lastly, an eigenanalysis-based band prioritization can be coupled with a divergence-based band decorrelation to design the band-selection method that is desired (Chein, Qian et al. 1999, Preet 2015).

4.7.5 MULTI-CORRELATION MATRIX STRATEGY

A different strategy to select important bands or wavelength domains is the Multi-Correlation Matrix Strategy as developed by Aasen, Gnyo et al. (2014). Correlation matrices from hyperspectral vegetation indices help to select both important and redundant bands (Aasen, Gnyo et al. 2014). Aasen, Gnyo et al. have introduced the software HyperCor, which automates pre-processing of narrowband hyperspectral field data and computes correlation matrices. Additionally, their proposed multi-correlation matrix strategy combines these matrices from different datasets and uses more information from each matrix.

For their research, Aasen, Gnyp et al. (2014) had access to a large multi-temporal spectral library which they could derive vegetation indices and related regression models from. From a multi-year rice study, they could calibrate the models with data from three consecutive years and validate them with the data of two later years. The results – for the application of rice biomass detection in the tillering, stem elongation and heading – showed an improvement of the model performance by 10 to 62 percent after applying the multi-correlation matrix strategy.

As described in chapter 2.4, SDIs involve the spectral transformation of a minimum of two spectral bands; these spectral bands are linked through a mathematical formula (Aasen, Gnyp et al. 2014, Chuvieco 2016). The amount of spectral bands used determines the dimension of the SDI. Aasen, Gnyp et al. (2014) used three types of two-dimensional SDIs in HyperCor: the Ratio Vegetation Index (RVI; 4.6), Difference Vegetation Index (DVI; 4.7) and Normalized Difference Vegetation Index (NDVI; 4.3).

$$RVI = \frac{\rho_{NIR}}{\rho_R}$$
(4.6)

$$DVI = \rho_{NIR} - \rho_R$$
(4.7)

$$NDVI = \frac{\rho_{NIR} - \rho_R}{\rho_{NIR} + \rho_R}$$
(4.3)

The HyperCor software provides two pre-processing steps; limit the wavelengths to the range of interest by identification of the device that was used to collect the spectra for a given dataset (1) and eliminating the detector offset at the transition wavelengths from one detector to another (2). The latter step is taken as it strongly influences the calculated SDIs. There are multiple reasons for such an offset to occur and depends highly on the instrument, temperature for example can be of influence (Milton, Schaepman et al. 2009). Figure 13 shows an example of the spectra from different nitrogen levels before and after correction for the detector offset.

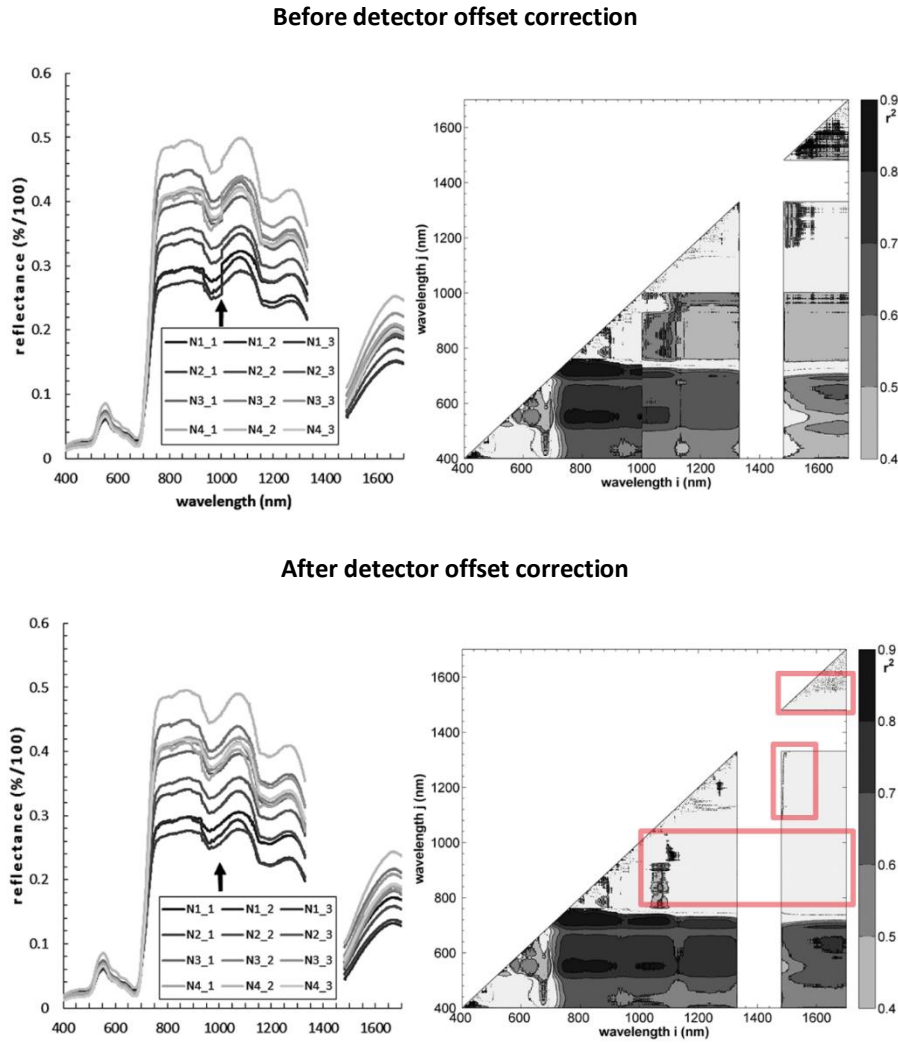


Figure 13 | These graphs show the spectral signatures from different nitrogen levels of a dataset of stem elongation stage in 2012 (left) and lambda by lambda correlation plots for biomass (right). High values (dark color) indicate that the wavelength which is set as the independent variable has high predictive value over the dependent wavelength. The red rectangles in the lower right graph indicate the main differences of before and after the detector offset in the correlation plots (Aasen, Gnyp et al. 2014).

After pre-processing, two steps are considerable to optimize the data analysis and focus on relevant parts of the spectrum. Firstly, the calculation of descriptive statistics of the input dataset help to identify important parts of the spectrum (Bajwa and Kulkarni 2011, Mahlein, Rumpf et al. 2013). Secondly, the redundancy matrices or lambda by lambda correlation plots (figure 15) help to determine the usefulness of all bands by calculation of the degree of redundancy between two spectral bands (Thenkabail, Smith et al. 2000, Thenkabail, Enclona et al. 2004a, Thenkabail, Enclona et al. 2004b, Aasen, Gnyp et al. 2014). A redundancy threshold can be set to exclude certain bands from further analysis; this way, the most useful hyperspectral narrow bands (HNBs) can be detected (Thenkabail, Enclona et al. 2004a, Thenkabail, Enclona et al. 2004b, Thenkabail, Mariotto et al. 2013).

Next, a procedure follows to identify optimal band combinations for HVIs, in the form of correlation matrices (Thenkabail, Mariotto et al. 2013). This matrix contains the correlations of band combinations for a chosen SVI type – HyperCor offers ratio, difference or normalized difference (Aasen, Gnyp et al. 2014). From this, best band combination lists and/or histograms can be retrieved.

It is possible that in one single correlation matrix (CM), a band combination or domain appears to be insignificant. For a CM, one dataset and one method (SVI type) is used. After combining this CM with one or other CMs, bands may start to show the information they contain. Aasen, Gnyp et al. (2014) developed the multi-correlation

matrices strategy (MCMS), which allows users to gain greater insight into the significance of individual bands. Ultimately, the MCMS allows for identification of potential bands to be used for HVI development. The function of this strategy, carried out cell wise, connects the informative content of multiple CMs. For the purpose of HVI construction, cells with the desired features can be selected from the multi-correlation matrix directly – additionally, the matrix can be used for further processing instead.

The study of Aasen, Gnyp et al. (2014) was aimed at developing HDIs predicting rice biomass at different growth stages and for the entire growth period – which was 2007-2009. The workflow of their study broadly consists of multiple steps (Annex N). Firstly, nine datasets representing a single growth stage in a single year (SGSY) and three datasets representing all data from a single year (SGAY) were exported for calibration. One dataset with combined data from all growth stages and calibration years (AGAY) was exported as well. First of all, the detector offset is corrected for all datasets, water absorption bands are removed and the spectral range is restricted to a range available for all data sets. Aasen, Gnyp et al. (2014). After obtaining the CMs and applying the MCMS and direct approach, band selection for the development of an HVI is ultimately done by determining the difference between the direct and MCMS approach. The models resulting from both approaches (figure 14) are validated with an independent dataset originated from the years 2011 and 2012.

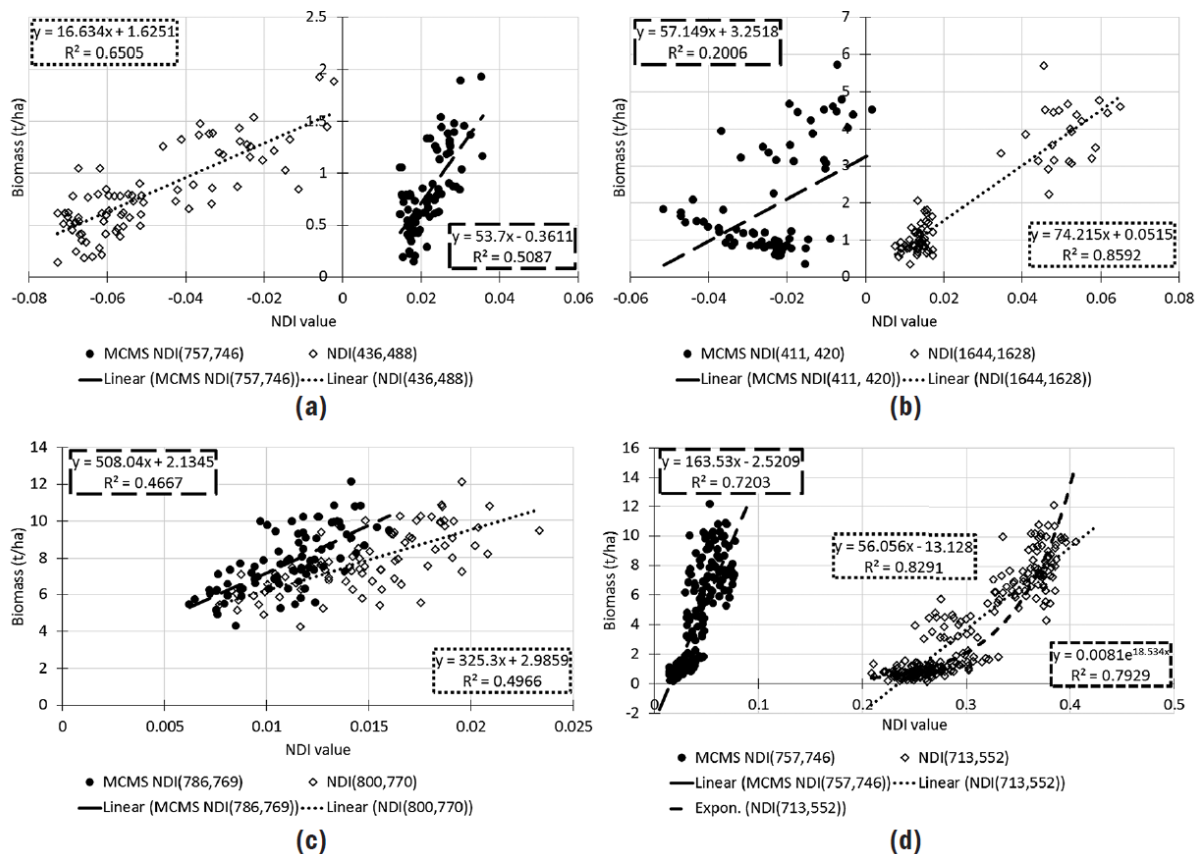


Figure 14 | Plots of biomass against the NDI values derived from the MCMS and direct approach together with their regression models: (a) tillering stage (b) stem elongation stage, (c) heading stage and across all stages (d) (Aasen, Gnyp et al. 2014).

The results of the study show that overall, the model from the MCMS approach had a better performance. Also, the wavelength identification differed depending on the growth stages and the approach. All but one of the identified band combinations were located in the visible and NIR region; the bands for the direct approach at stem elongation were situated in the SWIR (Aasen, Gnyp et al. 2014). All but one band combinations were situated in the same wavelength domain; only the band combination from the ‘Across All Stages’ model derived from the direct approach do not (Annex N). Overall, for the individual growth stages of the calibration dataset, the MCMS model performed weaker than the direct approach model. The R^2 of the MCMS model is averagely

lower and the SEE higher than those of the direct approach model (table 2). In the validation dataset however, the performance of the direct approach showed poorer than the performance of the MCMS model. The exponential models did not perform as well as the linear models; only for the direct approach applied to the 'Across All Stages' dataset the exponential model was perceived as advantageous by Aasen, Gnyp et al. (2014).

Table 2 | Results of MCMS (grey) and direct approach (white). For both calibration and validation are given: the coefficient of determination (R^2), standard error of the estimate (SEE) and the root mean square error (RMSE). The exponential regression model results are only achieved mentionable for the 'Across all stages' dataset (Aasen, Gnyp et al. 2014).

Stage	VI	MCMS R^2	Calibration		Validation	
			R^2	SEE (t/ha)	R^2	RMSE (t/ha)
Tillering	NDI(757,746)	0.40	0.51	0.28	0.85	0.22
	NDI(436,488)		0.65	0.23	0.23	1.18
Stem Elongation ¹	NDI(411,420)	0.25	0.20	1.27	0.67 ²	1.51
	NDI(1644,1628)		0.86	0.53	0.38 ¹	1.28 ¹
Heading	NDI(786,769)	0.31	0.47	1.21	0.60	1.21
	NDI(800,770)		0.50	1.18	0.37	1.40
Across All Stages	NDI(757,746)	0.27	0.72	1.78	0.82	1.22
	NDI(713,552)		0.83	1.39	0.64	2.34
	NDI(713,552) exp		0.79	NaN ³	0.72	2.17

¹ One extreme outlier from noise in the spectrum was eliminated before evaluation of the validation R^2 and RMSE

² Observed and predicted biomass inversely correlated

³ SSE not applicable for exponential model

5. DATA DESCRIPTION

As the feasibility and outcome of this study greatly depends on the potentials and restrictions that come with the available hyperspectral and reference data and statistical methods which will be used for the data analysis and SDI construction. Paragraphs 5.1 and 5.2. briefly discuss these restrictions.

5.1 DATA COLLECTION AND TEST SITE



Flights with the Rikola hyperspectral camera have been executed by WENR on the 14th and the 26th of June in 2017. Imagery were taken from a field of winter barley plots at Rilland, located near the Belgian border in the Dutch province of Zeeland (figure 17).

Data provided by Limagrain Nederland consists of field data and shapefiles – 2.823 fields in total. The shapefiles and field data – an Excel file containing among other attributes the brown rust scores for each plot – have been given plot IDs – which needed to be checked and linked correctly.

As the plots include so-called filling crops – “vulgewas” – and the imagery is not flawless, the amount of plot data that does fulfil the requirements for statistical analysis was not determined yet. During the phase of pre-processing, this would become evident for the most part.

Figure 15 | Location of the winter barley plots at Rilland, Zeeland (source: Aurea Imaging).

Annex F shows the different trial fields that were present within the winter barley field. The trial fields are filled with different genotypes. The different fields contain a minimum of 34 and a maximum of 921 plots.

Both the UAV and sensor used for obtaining the hyperspectral data are lightweight systems. The Rikola Snapshot Hyperspectral camera is currently used in agriculture, forestry, water research and for medical and forensic purposes. It is the only snapshot hyperspectral device available and provides real spectral response to each pixel. As the device is widely used in agriculture, the systems should be very well suitable for this thesis study.

The Altura Pro AT8 UAV was first used by WUR in 2012 and is still operative today. The most important disadvantage of this lightweight system is it's limited performance under windy conditions. Further specifications of the Rikola sensor system used are presented in Annex D.

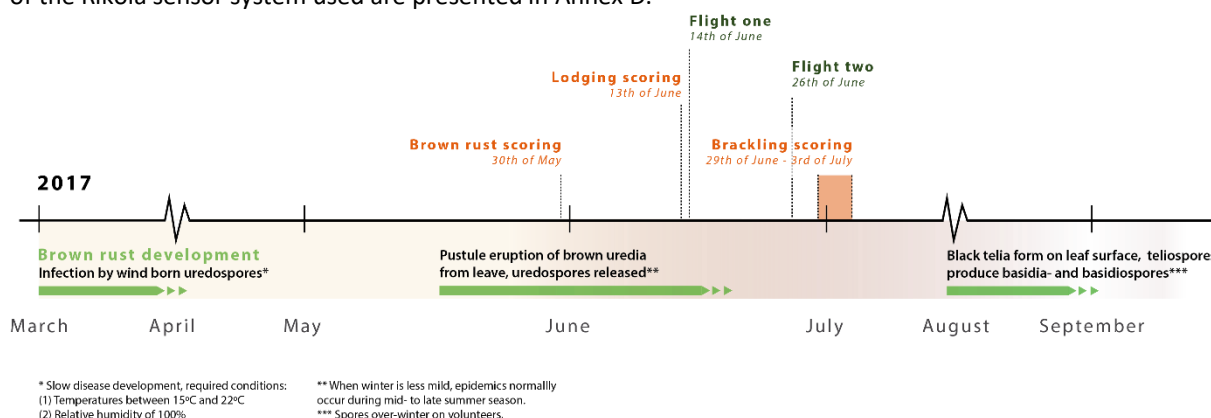


Figure 16 | Timeline marked with the collection of hyperspectral data (green) and validation brown rust, lodging and brackling scores (orange). The main development phases of the brown rust disease is indicated below the timeline.

The timeline of figure 16 illustrates the collection of the data that was used for this thesis. The brown rust scoring has been performed two weeks before the first flight. As both activities occurred within the same stage of development of the disease, no great developments took place within this timeframe – which means that the data is suitable enough for this thesis’ research purposes. The scoring of the lodging and brackling is included in figure 16 as they are important external variables included in this thesis study. For a visualization of the spreading of brown rust, lodging and brackling scores, reference is made to Annex E.

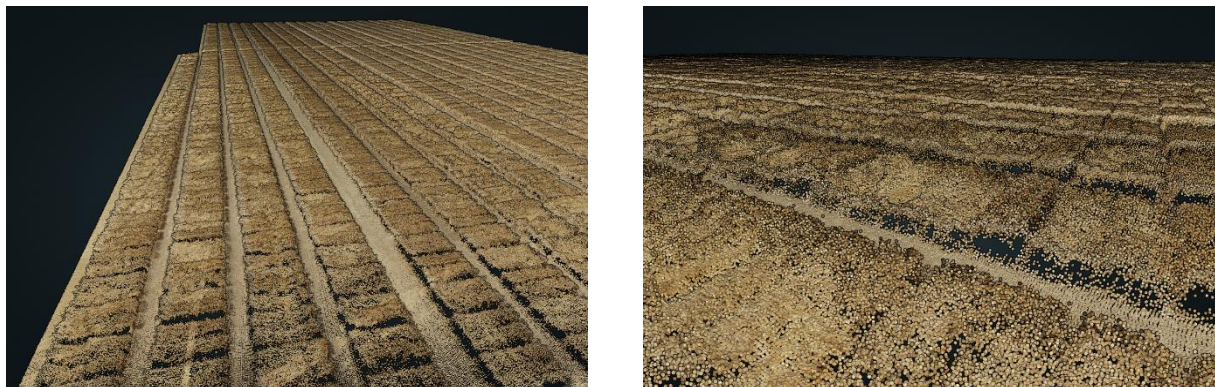


Figure 17 | LiDAR imagery of the winter barley plots, produced by WENR the 26th of June. On this imagery, the flattening effects of lodging and brackling become evident. Naturally, affected plots containing lodged or brackled crops have a very divergent spectral signature.

6.2 HYPERSPECTRAL DATASETS

For this study, two hyperspectral datasets obtained through UAV flights with a Rikola hyperspectral camera both executed in July 2017 are available. Each dataset contains imagery of the winter barley plots at the location of Rilland, Zeeland. Both datasets exist of 16 bands. Unfortunately, for some reason the camera settings for the second flight were different, causing the sensor to measure the reflections at wavelengths diverging from the first flight (table 3).

Table 3 | The sensor settings for both Rikola flights above Rilland in June of 2017 are divergent; reflectance is measured at different wavelengths. Closely spaced wavelengths of the two flights are highlighted – they are of particular interest in attempting to study the spatio-temporal development of the disease (SRQ3).

Band	Spectral region	Wavelength (nm) UAV flight 14-6-2018	Spectral region	Wavelength (nm) UAV flight 26-6-2018	Wavelength (nm) difference	Wavelength (nm) difference
1	YELLOW	609	YELLOW	514	95	
2	YELLOW	615	YELLOW	529	86	
3	RED	625	YELLOW	550	75	
4	RED	631	YELLOW	570	61	
5	RED	663	RED	630	33	1
6	RED	682	RED	669	13	
7	RED Edge	692	RED	680	12	2
8	RED Edge	696	RED Edge	690	6	2
9	RED Edge	715	RED Edge	700	15	
10	RED Edge	735	RED Edge	709	26	
11	NIR	764	RED Edge	720	44	
12	NIR	793	RED Edge	739	54	4
13	NIR	833	NIR	759	74	5
14	NIR	862	NIR	780	82	
15	NIR	872	NIR	800	72	7
16	NIR	887	NIR	869	18	3

6.2.1 DATA RESTRICTIONS

The restrictions of the data are related to a selection of factors as listed below:

1. Subjectivity of the validation data - as manual scoring was performed – a different view angle of the scoring Limagrain employees and the UAV-sensor might very well influence the data.
2. Time difference between the UAV-flights and manual scorings (figure 18).
3. Diverging sensor settings of the second UAV-flight.
4. Limited amount of bands – no bands in the blue and green spectral regions.
5. Heterogeneity of the data itself – many external variables influencing the reflectances.

Partly as a result of the variability between the two moments of recording, the imagery comes with both technical limitations as limitations due to the variability in the data itself. Though all data was gathered in the same growth stage of the brown rust, and therefore this should not cause major problems during the analysis phase, the second flight was conducted several days before harvest – meaning that the crop was brown of color. The imagery of the second flight is characterized by a typical signature for senescent vegetation, these reflectances are too divergent to allow for the addition of a proper spatio-temporal research aspect. For the difference in mean reflection between the two flight dates, reference is made to Annex J. The availability of spectral bands directs this study to the use of red, red edge and near-infrared spectral bands. Altogether, the data of the first flight and the validation data are useful enough for this thesis.

6.3 IN-SITU DATA

The validation or ground data (figure 18) was provided by Limagrain Nederland and consists of an Excel file with among other attributes, the plot codes and brown rust scoring given to each plot. These manual scorings were given by breeding experts of the company on the 30th of June in 2017 – two weeks before the first UAV-flight was executed.

In theory, the brown rust – even as the brackling and lodging – scores given by Limagrain vary between values from 1 to 10, respectively representing low to high severity. For this part of the study, assumed is that scores of 1 represent that the crop is not affected by the particular variable. In practice, scores from 1 to 8 were given to the plots.

Block	Plot Code	Location	Plot Code (2K-2V)	Plot Code (3K-3V)	Rep	Total group	WEI	YLD	YLD/Yield	BR1	BR2	BR3	HCM	Score
1	W7MV	66	4	FALSE	1	RIRI	RIRIW7MV6504	RIRIW7MV06004	1	Y26R61	572	848	4	2
2	W7MV	46	6	FALSE	1	RIRI	RIRIW7MV4606	RIRIW7MV04606	2	Y26R61	613	9077	4	1
3	W7MV	65	4	FALSE	2	RIRI	RIRIW7MV6504	RIRIW7MV06504	1	Y26R61	594	8804	3	1
4	W7MV	51	6	FALSE	2	RIRI	RIRIW7MV5106	RIRIW7MV05106	2	Y26R61	621	9203	4	1
5	W7MV	64	4	FALSE	3	RIRI	RIRIW7MV6404	RIRIW7MV06404	1	Y26R61	485	7191	5	1
6	W7MV	62	5	FALSE	3	RIRI	RIRIW7MV6205	RIRIW7MV06205	2	Y26R61	519	7692	6	1
7	W7MV	63	4	FALSE	4	RIRI	RIRIW7MV6304	RIRIW7MV06304	1	Y26R61	555	8216	3	2
8	W7MV	41	5	FALSE	4	RIRI	RIRIW7MV4105	RIRIW7MV04105	2	Y26R61	684	10129	2	3
9	W7MV	62	4	FALSE	5	RIRI	RIRIW7MV6204	RIRIW7MV06204	1	Y26R61	631	9347	4	3
10	W7MV	50	5	FALSE	5	RIRI	RIRIW7MV5005	RIRIW7MV05005	2	Y26R61	707	10476	4	3
11	W7MV	61	4	FALSE	6	RIRI	RIRIW7MV6104	RIRIW7MV06104	1	Y26R61	603	8926	3	3
12	W7MV	22	5	FALSE	6	RIRI	RIRIW7MV2205	RIRIW7MV02205	2	Y26R61	676	10015	3	3
13	W7MV	60	4	FALSE	7	RIRI	RIRIW7MV6004	RIRIW7MV06004	1	Y26R61	557	8256	2	3
14	W7MV	33	5	FALSE	7	RIRI	RIRIW7MV3305	RIRIW7MV03305	2	Y26R61	749	11104	3	3
15	W7MV	59	4	FALSE	8	RIRI	RIRIW7MV5904	RIRIW7MV05904	1	Y26R61	67	9929	1	2
16	W7MV	56	5	FALSE	8	RIRI	RIRIW7MV5605	RIRIW7MV05605	2	Y26R61	734	10868	3	2
17	W7MV	58	4	FALSE	9	RIRI	RIRIW7MV5804	RIRIW7MV05804	1	Y26R61	58	8597	2	1
18	W7MV	59	5	FALSE	9	RIRI	RIRIW7MV5905	RIRIW7MV05905	2	Y26R61	638	945	3	1
19	W7MV	57	4	FALSE	10	RIRI	RIRIW7MV5704	RIRIW7MV05704	1	Y26R61	578	856	2	2
20	W7MV	58	6	FALSE	10	RIRI	RIRIW7MV5806	RIRIW7MV05806	2	Y26R61	561	8305	3	1
21	W7MV	56	4	FALSE	11	RIRI	RIRIW7MV5604	RIRIW7MV05604	1	Y26R61	642	9505	3	3
22	W7MV	54	5	FALSE	11	RIRI	RIRIW7MV5405	RIRIW7MV05405	2	Y26R61	647	9581	4	3
23	W7MV	55	4	FALSE	12	RIRI	RIRIW7MV5504	RIRIW7MV05504	1	Y26R61	622	9216	1	2
24	W7MV	48	5	FALSE	12	RIRI	RIRIW7MV4805	RIRIW7MV04805	2	Y26R61	727	1077	3	1
25	W7MV	54	4	FALSE	13	RIRI	RIRIW7MV5404	RIRIW7MV05404	1	Y26R61	642	9513	2	1
26	W7MV	40	5	FALSE	13	RIRI	RIRIW7MV4005	RIRIW7MV04005	2	Y26R61	67	9919	3	2
27	W7MV	53	4	FALSE	14	RIRI	RIRIW7MV5304	RIRIW7MV05304	1	Y26R61	646	9572	2	1
28	W7MV	34	5	FALSE	14	RIRI	RIRIW7MV3405	RIRIW7MV03405	2	Y26R61	667	988	2	1

Figure 18 | Illustration of the Excel sheet with validation data provided by Limagrain Nederland BV. The brown rust scores are given in the second to last column of this screenshot.

6. METHODOLOGY

For this thesis, hyperspectral UAV imagery from the Rikola hyperspectral camera was tested on its relevance in the classification of winter barley plots on the basis of brown rust infection severity. Existing spectral vegetation and/or disease indices, statistical analysis and methods were used to achieve the research objectives as defined in chapter three. Validation of the results was done by use of the collected ground data – conventionally (manually) given brown rust scores – by Limagrain Nederland. See paragraph 5.1 for an introduction of the data and test site. The research design can be divided in four main phases or components:

1. Literature study
2. Pre-processing
3. Statistical analysis
4. Retrospect/discussion

The first, a literature research on the main concepts related to the subject, has been essential to get familiar with the problem – for this study, reference is made back to chapter four. The second component consists of the pre-processing of the data – paragraph 5.2 contains further specification of this part. The third component is aimed at answering the sub-research questions – producing the results of the research – using spectral vegetation indices and statistical methods – see paragraph 5.3. The last component concerns a conclusion and retrospect on the research.

6.1 PRE-PROCESSING

Before the provided data could be used for the statistical analysis, several pre-processing steps had to be taken. The storage settings for the two hyperspectral datasets is divergent and needed to be uniformized as much as possible. Thereby, the data obtained during the UAV flight of the 26th of June 2017 does not cover all plots. Additionally, the available shapefiles representing the area of the real plots still had to be fitted nicely over the imagery – naturally, for the data analysis it is essential to make sure that the pixels that fall within the shapefiles are in fact pixels that represent the different plots. The influence of plot border pixels – of which the reflectance contains more influence of the soil – and pixels from outside a plot is undesirable. Furthermore, the shapefile plots needed to be linked to the corresponding records of the ground data - initially, not all the IDs corresponded correctly. Finally, the reflections have been averaged per plot.

After the calculations performed during the former steps, a basic selection of usable winter barley plots took place. Some plots were not scored for brown rust and/or plot shapefiles did not cover set of usable reflection values (figure 20). Plots that did not meet the following conditions were selected out:

1. Available brown rust score
2. Complete set of (16) reflection values
3. 0% NoValue pixels

During the statistical analysis, it was attempted to reduce the external variability by including the lodging and brackling scores of the plots. Not all plots were scored for lodging and/or brackling either, so for the purpose of further external variability reduction those plots had to be filtered out as well (figures 19 and 20).

Table View						
AttributeManager_20_OUTPUT - AttributeManager_20_OUTPUT						
	Plot_code	Brown_rust	Lodging	Brackling	mean_1	mean_2
1675	RIRIW7MV001002				9254.76973684...	9199.46
1676	RIRIW7MV067003				9829.03282275...	9749.60
1677	RIRIW7MV066003				9414.04824561...	9329.87
1678	RIRIW7MV065003				9413.16666666...	9345.16
1679	RIRIW7MV064003	3		3	10208.8205689...	10123.7
1680	RIRIW7MV063003	2		1	8887.23841059...	8734.77
1681	RIRIW7MV062003	3		1	8981.74945054...	8799.12
1682	RIRIW7MV061003	4		2	8433.16666666...	8287.51
1683	RIRIW7MV060003	3		1	8326.94323144...	8143.12
1684	RIRIW7MV059003	3		2	7842.61504424...	7690.55
1685	RIRIW7MV058003	3		3	6476.73845453...	6247.00

Figure 19 | Not all plots contained a full set of brown rust, lodging and/or brackling scores.

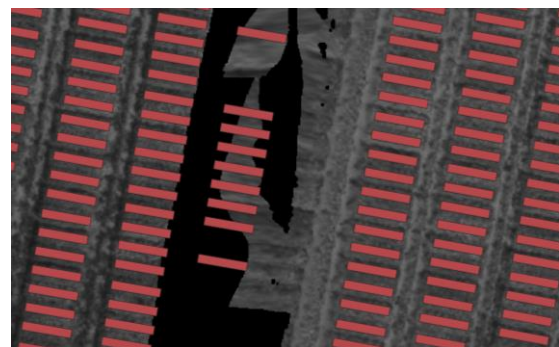


Figure 20 | Several plots were not fully covered by the hyperspectral imagery (this figure concerns the imagery of the flight executed on the 14th of June 2017).

6.2 STATISTICAL ANALYSIS

The statistical analysis is structured by the research questions of this study. For each of the three sub-research questions the relevant explanation and statistical steps are described in the following paragraphs. The first two were addressed using the hyperspectral data of the first flight, the third sub-research question

6.2.1 SUB-RESEARCH QUESTION ONE

What is the classification accuracy of existing spectral vegetation and disease indices on winter barley brown rust?

As described in paragraph 5.6, spectral vegetation indices are robust and simple tools to extract quantitative information on the amount of vegetation or greenness for every pixel in an image (Chuvieco 2016). In the pre-processing phase, reflections have been averaged over each of the 2639 plots that proved to be useful for this thesis study – in other words, the plots that survived the pre-processing phase. For answering the first research question, the average reflections of the plots in the RED, RED edge and NIR spectral regions have been used to calculate index values of a selection of indices (tables 4 and 5).

Table 4 | Hyperspectral bands and associated wavelengths used for RED, RED edge and NIR spectral regions used for calculating the index values of the indices indicated in table 5.

Spectral range	Bands	Wavelengths
RED	3, 4, 5, 6	625, 631, 663, 682
RED edge	7, 8, 9, 10	692, 696, 715, 735
NIR	11, 12, 13, 14, 15, 16	764, 793, 833, 862, 872, 887

Table 5 | Explanation of the indices used for addressing the first sub-research question.

Index	Description/calculation	Reference
ND 790/670	<p>Normalized Difference 790/670</p> <p><i>This index is a so-called simple ratio index. For this study, the wavelengths of 790 and 670 were not available. The two bands closest to these wavelengths were used instead. This index is a narrowband vegetation index. Note that the bands of the hyperspectral data used for this study are more or less 10nm of width.</i></p> $\frac{(793nm - 663nm)}{(793nm + 663nm)}$	(Barnes 2000)

NDVI	<p>Normalized Difference Vegetation Index NIR/RED <i>This index is a - particularly in satellite remote sensing - widely used simple ratio index. Values vary between -1 and 1. Positive values above 0,2 indicate living vegetation. The NDVI is typically a broadband vegetation index.</i></p> $\left(\frac{NIR - RED}{NIR + RED} \right)$	(Huete and Jackson 1987)
NDRE	<p>Normalized Difference Red Edge <i>A variation of the NDVI, where the red spectral region is replaced by the red edge spectral region. Compared to the NDVI, the NDRE is less prone to saturation in higher growth stages of dense crops like winter barley. The NDRE has a lower correlation with the LAI and has potential to measure further down the canopy than the NDVI.</i></p> $\left(\frac{NIR - RED_{edge}}{NIR + RED_{edge}} \right)$	(Barnes 2000)
PVI	<p>Perpendicular Vegetation Index <i>An orthogonal based vegetation index that calculates the orthogonal distance to the 'soil line' – this soil line is determined on the basis of the reflection values of the dataset. Variables a and b represent respectively the slope and intercept of this line.</i></p> $\frac{(NIR - a * RED) - b}{(1 + a^2)^{\frac{1}{2}}}$ <p><i>a = 0.8418540867 (slope) b = 2867.559548 (intercept)</i></p>	(Richardson and Wiegand 1978)
SAVI	<p>Soil-Adjusted Vegetation Index <i>This vegetation index takes into account the influence of reflection of the soil. Parameter L represents the soil brightness correction factor; in highly vegetated areas L = 1, for areas lacking green vegetation L = 0. For this study, the default value of 0,5 is used. When L=0, the SAVI is equal to the NDVI.</i></p> $\left(\frac{NIR - RED}{NIR + RED + L} \right) * 1 + L$ <p><i>L = 0,5</i></p>	(Huete 1988)

In the attempt to determine the statistical relationship between the spectral index values and the brown rust scores, a simple linear regression was performed for which the mean reflections per spectral region were used for the calculation of the index values of the indices indicated in table 9.

6.2.2 SUB-RESEARCH QUESTION TWO

What are the possibilities of constructing a spectral disease index (SDI) for winter barley brown rust using band prioritization and decorrelation methods?

This research question was addressed following a list of steps, specified in table 6. The steps are covering a first interpretation of the data, the identification of relevant SVI types and band combinations, the construction of a



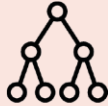



disease index, but also some training and testing with the data. Table 7 shows the method that led to the final results as presented in the next chapter.

Table 6 | Workflow addressing sub-research question two.

	Step description	Notes
1	Calculate descriptive statistics.	(1) R package 'stats v3.6.0' used. (2) Consult Annex H for theoretical background.
2	Specify three SVI types for the purpose of computing correlation and redundancy (lambda-lambda) matrices.	Examples of SVI types; ratio, difference, orthogonal, soil-adjusted, etc.
3	Compute lambda-lambda matrices in R of all trial fields.	R package 'stats v3.6.0' was used.
4	Identify optimal band combinations and SVI type for a hyperspectral disease index.	The lambda-lambda plots are used as a tool to identify these bands and SVI type.
5	Construct three disease indices for the detection of brown rust on winter barley – one per SVI type.	Use the identified optimal band combination for each SVI type.
6	Use the identified optimal SVI type and band combinations to build a model that predicts the brown rust scores of the individual plots. Correlate these predicted scores with the actual brown rust scores to identify the best SVI type.	(1) R packages 'stats v3.6.0' and 'caret v6.0-84' were used. (2) This step is not an essential step to construct a disease index, it rather shows the potential of training this data – ultimately resulting in stronger correlations.

The descriptive statistics are provided in Annex H will give a first interpretation of the data before identifying optimal band combinations for the construction of a spectral – disease – index. Table H1 of Annex H provides a summation and short explanation of the statistics that were calculated for this purpose.

Table 7 | The method leading the results for sub-research question two.

Normalized difference		Orthogonal		Soil-adjusted	
<div>Corr</div> <div>R²</div>		<div>Corr</div> <div>R²</div>		<div>Corr</div> <div>R²</div>	
Select 30 best band combinations		Select 30 best band combinations		Select 30 best band combinations	
 Use index values as variables in prediction model: Method cross-validation Search random Predictors = 30 Folds = 5 Repeats = 5	Construct a normalized difference disease index	 Use index values as variables in prediction model: Method cross-validation Search random Predictors = 30 Folds = 5 Repeats = 5	Construct an orthogonal disease index	 Use index values as variables in prediction model: Method cross-validation Search random Predictors = 30 Folds = 5 Repeats = 5	Construct a soil-adjusted disease index
	 Use index values as variables in prediction model: Method cross-validation Search random Predictors = 1 Folds = 5 Repeats = 5		 Use index values as variables in prediction model: Method cross-validation Search random Predictors = 1 Folds = 5 Repeats = 5		 Use index values as variables in prediction model: Method cross-validation Search random Predictors = 1 Folds = 5 Repeats = 5
	Correlate predicted brown rust scores with actual brown rust scores		Correlate predicted brown rust scores with actual brown rust scores		Correlate predicted brown rust scores with actual brown rust scores
Correlate predicted brown rust scores with actual brown rust scores		Correlate predicted brown rust scores with actual brown rust scores		Correlate predicted brown rust scores with actual brown rust scores	

7. RESULTS

In this chapter, the results of the statistical analysis are presented. The results addressing the two sub-research questions are divided over the paragraphs 7.1 to 7.2. In the first paragraph, the first results clearly show the potential of the information that is present in the hyperspectral data for brown rust disease detection. Paragraph 7.2 will present

7.1 CLASSIFICATION ACCURACY OF EXISTING SPECTRAL VEGETATION INDICES

This paragraph is divided in two parts. The first discusses the spectral signatures per brown rust score, the second discusses the linear regression between existing vegetation indices and the brown rust scores.

7.1.1 INFLUENCE OF BROWN RUST ON MEAN REFLECTANCE

The first results of this study are the mean reflection values per band for the different brown rust scores that were given to the plots by Limagrain inspectors (figure 21). The reflections per band for the brown rust scores for each trial field can be found in Annex G. For all plots, a mean reflection value was calculated; those means were subsequently averaged over the brown rust scores that were given to these plots. From the graph in figure 23, it becomes evident that the reflectances of the plots with different brown rust scores are diverging. Plots with a low brown rust score show the highest reflectances in the NIR bands. In the red edge region, these values 'flip' around; in the red, the highest reflectances are shown by plots with the highest brown rust scores. Relatively few plots received a brown rust score of 1, 7 and 8, which presumably relates to the diverging lines of these scores at the upper and lower wavelengths. Another important factor for the diverging spectral signatures of these brown rust classes is that the dataset is highly heterogenous and has many external variables.

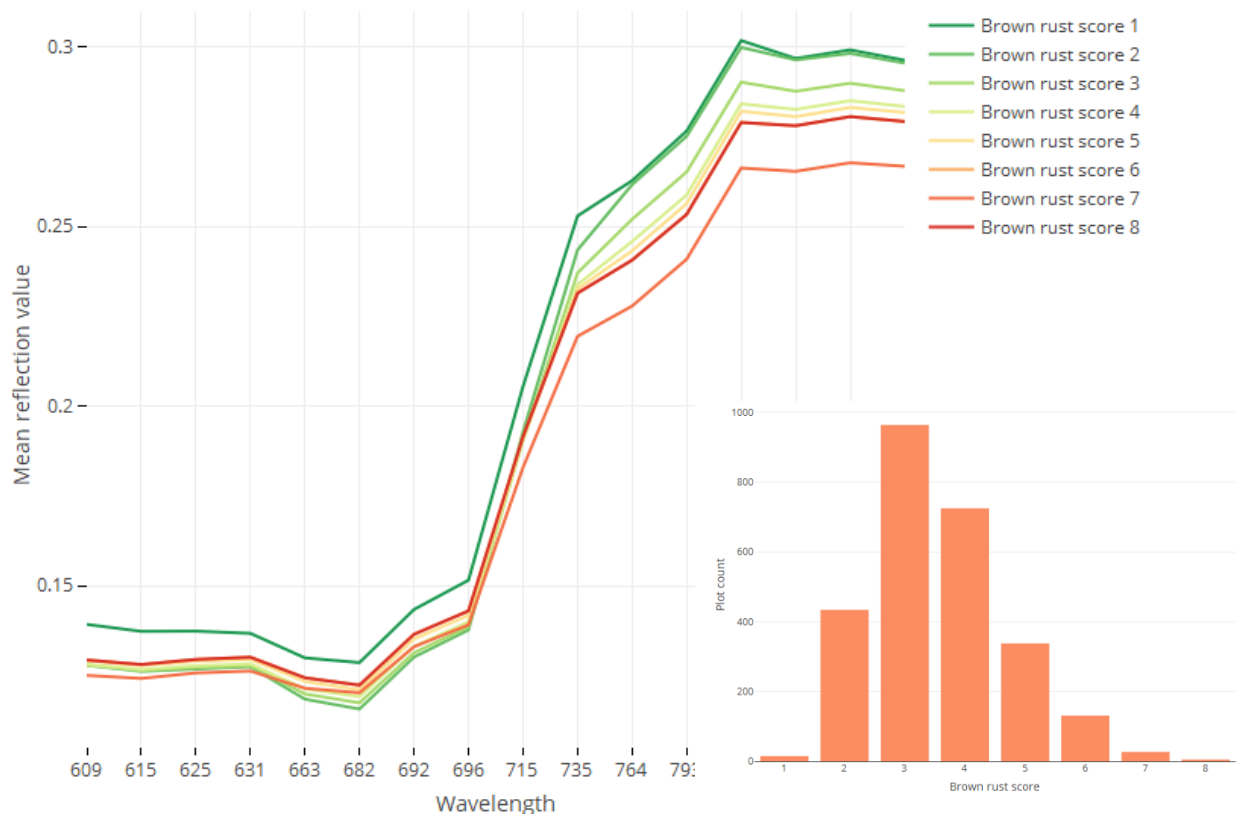


Figure 21 | Mean reflections per band for each of the given brown rust scores; wavelengths are visualized in nm, mean reflectance indicated in variation between 0 and 1. The histogram included in the figure illustrates the amount of observations that were made for each brown rust score visualized in the line graph. The line graph shows that the mean reflectances per brown rust score are 'flipped around' in the near-

infrared region – with an exception for the reflections of the plots scored with a brown rust score that was given relatively few times as reflectances of plots with scores of 1, 7 and 8 diverge from this trend evidently.

7.1.2 BROWN RUST SCORES AND EXISTING VEGETATION INDICES

From the simple linear regression that was performed to study the statistical relationship between the values of the indices and the brown rust scores, the correlation coefficients and coefficients of determination as presented in table 8 resulted. The first column concerns the results of the total population of plots. The following columns concern different plot selections, based on the brackling and lodging scores that were given to these plots. For an overview of all corresponding scatterplots, reference is made to Annex K.

The first column shows the correlation coefficients (R) and coefficients of determination (R^2) that were calculated using the full number of plots that ‘survived’ the pre-processing phase. In order to gain better insight in the influence of the two external variables brackling and lodging, calculations have been performed on a selection of the lowest scores – plots scored with 1 – as well. All plots have been scored on brackling, however merely 1490 of them were scored on lodging. To make better comparisons, calculations have been performed on a plot selection of plots that were scored on lodging as well – see the fourth column.

Table 8 | Correlation coefficients, coefficients of determination and root mean square errors of the indices and brown rust scores. Results are shown for six different plot selections – see column headers. Note that all plots were scored for brackling, therefore no separate selection was necessary for calculations.

Plot selection	All plots	Plots with a brackling = 1 score	Plots scored on lodging	Plots with a lodging = 1 score	Plots with a lodging = 1 and brackling = 1 score
Plot count	2637	552	1490	923	28

Index	Correlation coefficient (R)				
ND 793/663	-0.260868	-0.1687804	-0.2165886	-0.2680686	-0.1519575
NDVI	-0.2447097	-0.1654338	-0.2102741	-0.2605754	-0.132526
NDRE	-0.244919	-0.1660667	-0.2247058	-0.2400066	-0.09969654
PVI	-0.3406554	-0.2809728	-0.2178211	-0.4046482	-0.2992048
SAVI	-0.2447122	-0.163625	-0.2102753	-0.349921	-0.132529
Average R					-0.220769895
SD of Rs					0.066545544

Index	Coefficient of determination (R^2)				
ND 793/663	0.06805210	0.02848683	0.04691062	0.07186077	0.02309107
NDVI	0.05988284	0.02677247	0.04421519	0.06789952	0.01756314
NDRE	0.05998532	0.02757814	0.05049271	0.05760318	0.09939999
PVI	0.11604610	0.07894574	0.04744603	0.1637401	0.08952353
SAVI	0.05988405	0.02677315	0.04421571	0.1224447	0.01756394
Average R^2					0.044684372
SD of R^2 s					0.031800344

Index	Root mean square error (RMSE)				
ND 793/663	3.387553	2.531691	3.660867	3.581784	2.292085
NDVI	3.41603	2.567139	3.689242	3.609612	2.33088

NDRE	3.467002	2.626527	3.741888	3.658392	2.399267
PVI	3.603639	2.770303	3.882055	3.799775	2.559559
SAVI	3.530351	2.688193	3.807195	3.727494	2.469463
Average RMSE					2.915537
SD of RMSEs					0.112429

From the results, it is evident that the correlation coefficients and coefficients of determination look best for plots scored with 1 for lodging (table 8). From the six indices, the PVI performs best on all plot selections. The PVI values of plots scored with 1 for brackling are least significant, the lower count – 522 – of plots that were used in calculations might be of influence in this fact. Notably, despite the low count of 28, plots that were scored 1 for both lodging and brackling show better R and R²s than those of all plots scored with 1 for brackling. Better results are retrieved when the variability of lodging is decreased to a minimal – as a score of 1 is in theory the lowest score; these plots are assumed not to be affected by the considered variable.

The R² values are overall low, meaning the data is not closely fitted to the regression line (figure 22). The best performing index is the PVI and the best plot selection is the selection on plots scored with 1 for lodging – roughly 16% of the variance is explained by the brown rust score. For the total plot selection of 2637 plots, this is almost 12%.

Since the R² cannot determine whether estimates of the coefficients and predictions are biased, the residual plots of figure 23 are visually assessed. Residuals are the difference between observed values and the values predicted by the regression model. The residual scatter plot and histogram show the spreading of the residuals from the regression performed on the PVI values and brown rust scores belonging to plots scored with 1 for lodging. From the scatterplot, there is hardly any heteroskedasticity notable and the distribution shows no trends – meaning the variance is constant and there is no drift. The histogram to the left proves the distribution of residuals is approaching normal, which is desirable and means the data is not biased.

The root mean square error (RMSE; table 8) is interpreted as the standard deviation of the unexplained variance – which is the variance between the two variables. The RMSE is in the same unit as the reflectances. Lower values indicate a better fit of the regression line. Interestingly, the plot selections with fewer plots – those with a brackling score of 1 and those with both a score of 1 for brackling and lodging – have the lowest RMSEs for all indices. The highest RMSEs are found for the plots scored with 1 for lodging – the fifth column. When comparing the individual indices, the NDVI has the lowest RMSEs with an average of 3.21. The PVI has the highest RMSEs with an average of 3.40.

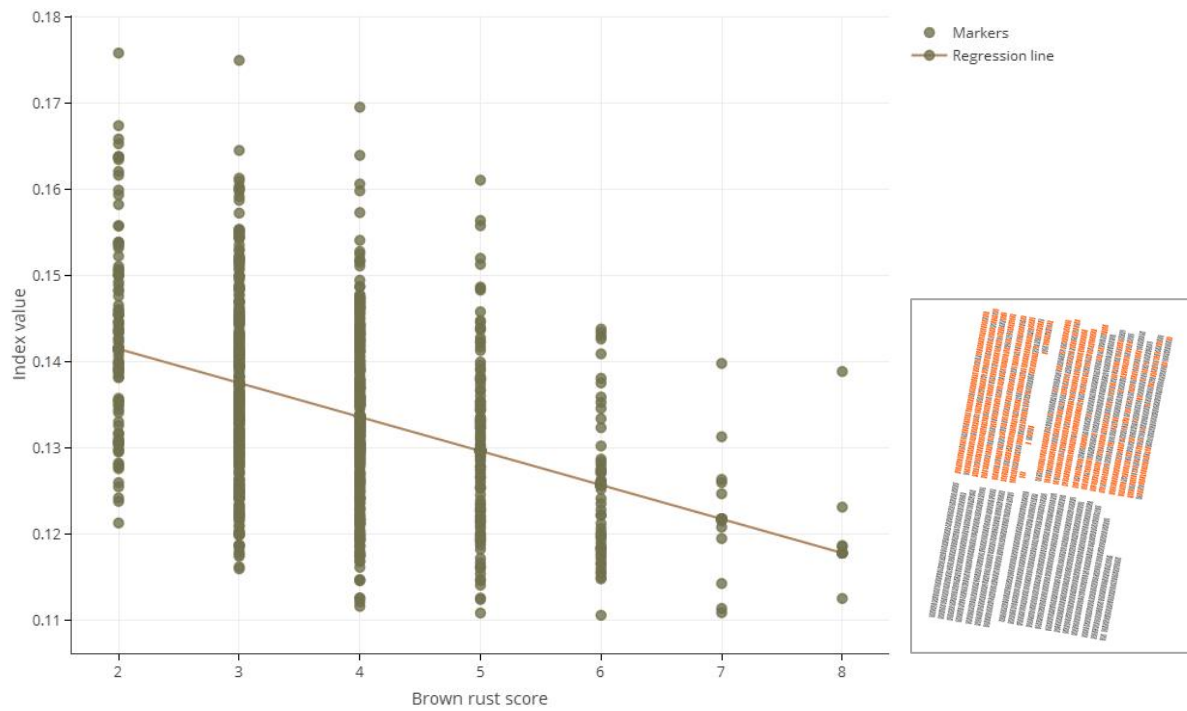


Figure 22 | Scatterplot of the PVI values against the brown rust scores of plots scored with a score of 1 for lodging. The concerning plots are indicated in orange on the overview map that is provided with the graph. The markers of the scatterplot show a reasonable spread, however a trend is clearly visible along the regression line.

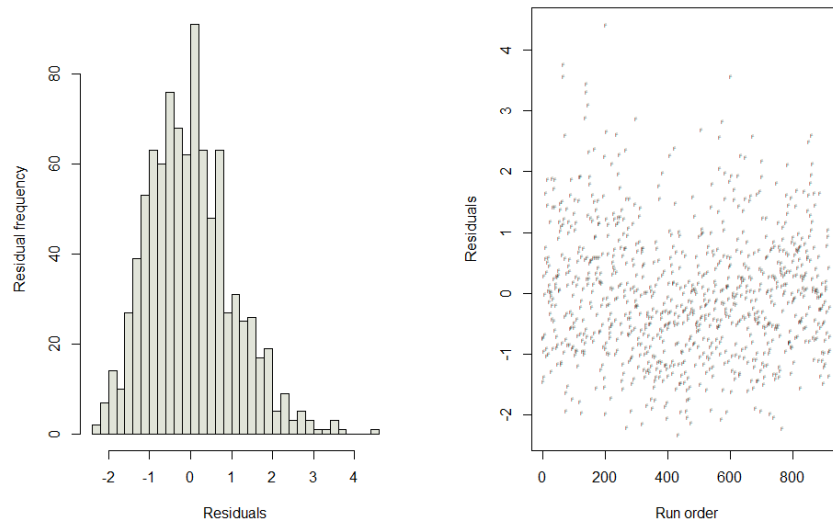


Figure 23 | Histogram and scatterplot of the residuals, meaning the observed – fitted values, of the regression model on the PVI values and brown rust scores of the plots scored with 1 for lodging.

7.2 CONSTRUCTING A SPECTRAL DISEASE INDEX (SDI) FOR WINTER BARLEY BROWN RUST

This research question was addressed by creating lambda-lambda matrices to the methods of Aasen, Gnyp et al. (2014). Three lambda-lambda or redundancy plots were made, for three different types of narrowband indices; normalized difference (1), orthogonal (2) and soil-adjusted (3). The matrices show the R^2 values between the index values based upon the index calculations using the bands indicated on the x- and y-axis and the brown rust scores.

Figures I1-I3 of Annex I are heatmap visualizations of the correlations between the brown rust scores and each possible band combination – for this particular hyperspectral dataset – per index type. Figures 26-28 are the corresponding redundancy matrices. Table 9 illustrates how the index values were calculated and thus how the values in the correlation and redundancy matrices (figures I1-I3 of Annex I and 24-26) should be interpret.

Table 9 | Calculation of the narrowband index values used to make the correlation plots visualized in figures 24-26 and the lambda-lambda plots of figures 27-29 . Band X refers to the band number on the horizontal axes of these figures, band Y refers to the bands indicated on the vertical axes.

	Type of index	Calculation
1	Normalized difference <i>- Derived from the NDVI -</i>	$\left(\frac{\text{band } Y - \text{band } X}{\text{band } Y + \text{band } X} \right)$
2	Orthogonal <i>- Derived from the PVI – a = 0.8765432 b = -0.04202</i>	$\frac{(\text{band } Y - a * \text{band } X) - b}{(1 + a^2)^{\frac{1}{2}}}$
3	Soil-adjusted <i>- Derived from the MSAVI2 –</i>	$\left(\frac{2 * \text{band } Y + 1 - \sqrt{(2 * \text{band } Y + 1)^2 - 8 * (\text{band } Y - \text{band } X)}}{2} \right)$

The lambda-lambda plots show per index type for which band combinations the redundancy is high and for which combinations it is low. From these matrices, we can derive the best performing wavelengths for each index type. The normalized difference index using the wavelengths of 872 and 793 nm, has with 0.137 the highest R^2 of all. The optimal formula per index type is given in table 10.

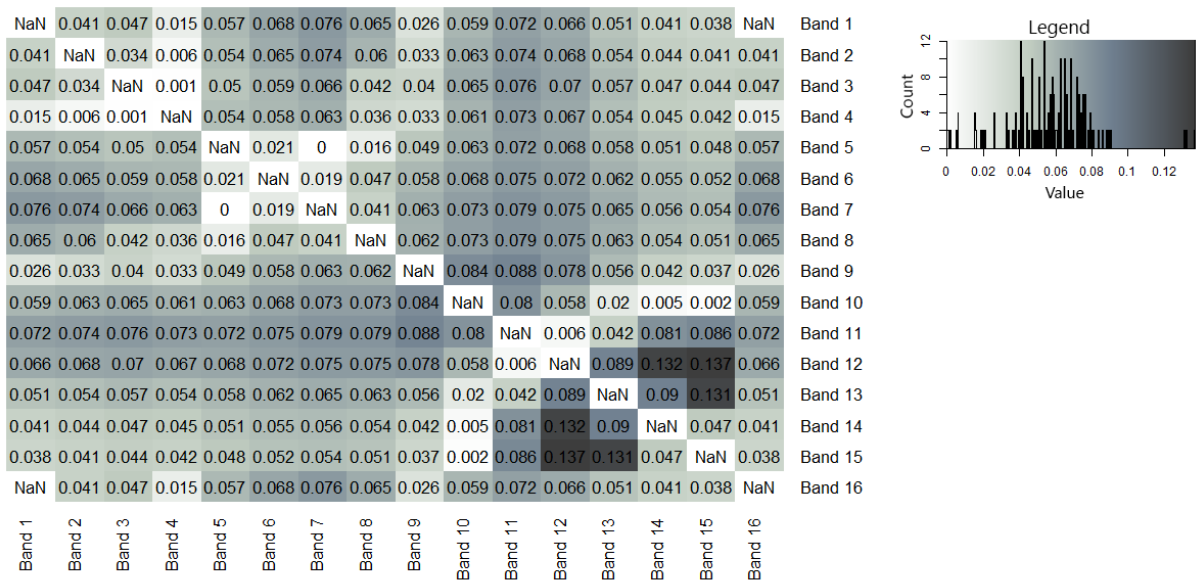


Figure 24 | Lambda-lambda (coefficient of determination R^2) contour plot showing the R^2 values of the normalized difference (ND) index values \sim brown rust scores. This plot is created using the 16 band hyperspectral data retrieved at the 14th of June 2017. The axes are provided with the narrowband wavelengths and band numbers. The legend shows the spreading of the R^2 values. All band combinations with the value 'NaN', show no correlation with the brown rust scores, and therefore have no R^2 value either.

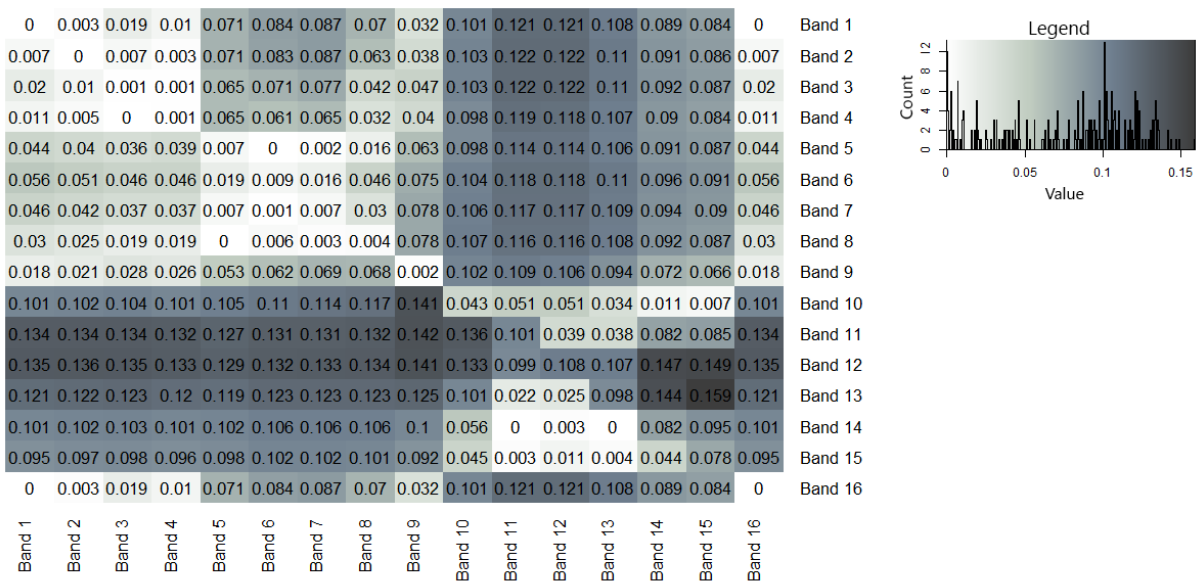


Figure 25 | Lambda-lambda (coefficient of determination R^2) contour plot showing the R^2 values of the orthogonal index values \sim brown rust scores. This plot is created using the 16 band hyperspectral data retrieved at the 14th of June 2017. The axes are provided with the narrowband wavelengths and band numbers. The legend shows the spreading of the R^2 values.

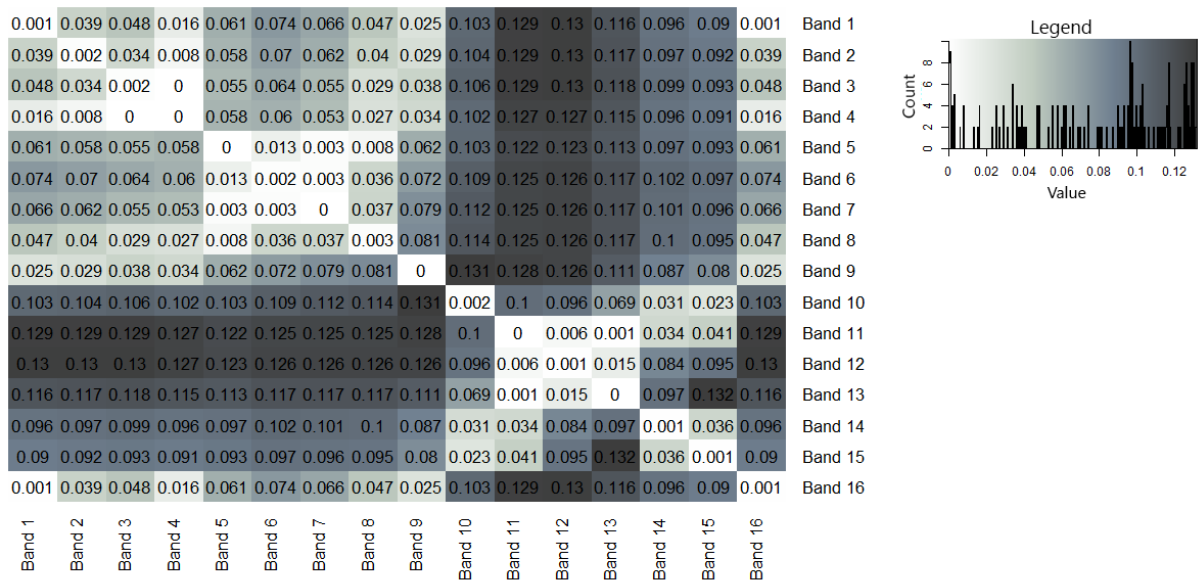


Figure 26 | Lambda-lambda (coefficient of determination R^2) contour plot showing the R^2 values of the soil-adjusted index values ~ brown rust scores. This plot is created using the 16 band hyperspectral data retrieved at the 14th of June 2017. The axes are provided with the narrowband wavelengths and band numbers. The legend shows the spreading of the R^2 values.

Table 10 | Optimal indices according to the lambda-lambda matrices as visualized in the figures 29-31.

1	Normalized difference	$\frac{(793nm - 872nm)}{(793nm + 872nm)}$
2	Orthogonal $a = 0.8765432$ $b = -0.04202$	$\frac{(833nm - a * 872nm) - b}{(1 + a^2)^{\frac{1}{2}}}$
3	Soil-adjusted	$\left(\frac{2 * 833nm + 1 - \sqrt{(2 * 833nm + 1)^2 - 8 * (833nm - 872nm)}}{2} \right)$

The three optimal indices can further be compared by adding their index values in a predictive model. In Annex M, the results of these three models are presented. The Pearson correlation coefficient of the predicted brown rust scores and actual brown rust scores is with 0.323 the highest where the orthogonal index values are used as a predictor. For normalized difference the correlation is 0.249 and for soil-adjusted it is 0.198.

In addition to the training and testing done for each index type with one predictor based on the optimal band combination, a coarser approach was taken as well. For each index type, the index values calculated using the 30 best band combinations – with the highest VI ~ brown rust R^2 values as visualized in figures 24-26 – were used as variables to create a random forest repeated cross validation model. The correlations between the predicted brown rust scores of the test set and the actual brown rust scores are given in Annex I. The Pearson correlation between the predicted brown rust values and the actual brown rust values using the orthogonal index values is with 0.517 the highest of the three. The orthogonal index of the second row in table 10 is the best performing index in this study, and therefore comes the closest to a SDI for winter barley brown rust.

8. DISCUSSION

In this section, final marks about this thesis study are drawn before presenting the conclusion in the next chapter.

8.1 KEY FINDINGS & INTERPRETATIONS

In the research problem definition and background of this thesis document, the relevance of identifying crop traits is broadly described. In crop science and for breeding companies, maximization of the crop yield and development of genotypes characterized with increased yield potential are respectively the main goals. Phenotyping efforts are a critical component in these developments. The potential role of UAV-RSPs, equipped with the relevant – in case of this study hyperspectral – sensors in rapid high-throughput crop phenotyping – ‘phenomics’ – is proven but not yet researched thoroughly. The case study of this thesis focuses on the potential of UAV-derived, 16-band hyperspectral data in the classification of winter barley plots on brown rust infection.

The results of this research indicate that there is a relationship between spectral reflectance of winter barley and the severity of the brown rust infection of this crop (figure 21). In other words, the question whether UAV-derived data could be relevant in the detection and categorization of winter barley brown rust can be answered in the affirmative. The relevance of UAV-RSP-based classification relative to conventional classification techniques has proven to be dependent of several factors.

First step of this study was to interpret the mean reflectances of the plots for each brown rust score. Comparison of the mean reflectances of healthy and brown rust infected sugar beet leaves found by Mahlein, Steiner et al. (2012, figure 7) with the mean reflectances resulting from this thesis’ study (figure 21), indicate both similarities and differences. First of all, both figures show a clear distinction of healthy and infected crop in the same spectral region. The figures show a higher absorption in the red for uninfected crops, this is explained by a decrease of the blue and red absorbing chlorophyll content after a brown rust infection. In the NIR however, the reflections differ. In both figures, the reflection is higher but only the results of this study show that the reflections ‘flip’ around in the red edge region. The brown rust infected leaves then have the highest absorption in the NIR and ‘healthy’ leaves the lowest; in the study of in the study of Mahlein, Steiner et al. this is not the case – healthy leaves show the highest absorption in both the red and NIR. Kept in mind should be that the studies concern different set-ups – respectively operational and experimental – and different crops. As reflection in the NIR is known to not only be dominated by leaf internal structure, leaf anatomy and epidermal surface but also the structure of the canopy, a difference in reflectance is not inexplicable. Most importantly, in both studies the distinction in reflectances for healthy and unhealthy crops can be made clearly in the same spectral regions.

Subsequently, the mean spectral reflectances of the different plots filled with the winter barley crop and the brown rust scores given to these plots by breeders – the validation data – were compared. For these plots, the index values of commonly used vegetation indices demonstrate a moderate linear relationship with the brown rust scores. The PVI shows with a moderate value of -0.405 the best Pearson correlation coefficient, for a plot selection of plots given a score of 1 for lodging – an external variable that evidently appeared to influence the reflectance of the crop during this study. Attempted was to correct for both lodging and brackling in determining the correlations. However, overall lodging seemed to be of greater influence as an external variable on the reflection values than brackling.

By consulting lambda-lambda or redundancy matrices for different types of vegetation indices – difference, orthogonal and soil-adjusted (figures 24-26), relevant band combinations for the construction of a specific disease index were identified. Of course, bearing in mind that the available hyperspectral bands for this thesis study is not quite extensive – in previous studies to rust diseases on vegetation, important wavelengths in the green and blue were identified as well (Liu, Gu et al. 2015, Heim, Wright et al. 2019). The matrices demonstrated that averagely, the soil-adjusted index values show the strongest R and R² values with the brown rust scores, however the best individual R² value of 0.159 is found for the orthogonal index using the wavelengths 833 and

872 nm. For each index type, an index based upon the optimal band combination was constructed. After training the data, the brown rust scores predicted using the orthogonal index values showed the strongest correlation with the actual brown rust scores (Annex M), which was expected.

With the use of index values from the best 30 band combinations, for each of the three index types another random forest prediction model was constructed (Annex L). Again, the model based on the orthogonal index values performed best; the Pearson correlation between the brown rust scores predicted by this model and the actual brown rust scores was 0.517. The models were based upon the entire dataset as they appeared to not perform well when merely the index values of plots scored with 1 for lodging were included – this would have been to reduce external variability and has led to more optimistic results in correlating the PVI to the brown rust scores for sub-research question one. Reason for the poorer predictions could be a critical decrease in amount of observations. It is likely that a model based on a dataset covering the index values of more winter barley plots with this lodging score would actually perform better than a model based on a dataset not corrected for this external variable.

The results of this thesis overall meet the expectations. As a fungal disease affects a crop on a physiological level and therefore has an effect on the pigments and structure of the organism, it was expected that the brown rust scores would correlate with the index values derived from the mean reflections for each plot. Given the modest size of the dataset and regarding the external variables uncontrolled circumstances, the found correlations are within the expected values. Strong correlations in studies like this are merely found when external variability is carefully addressed and the hyperspectral dataset is larger.

8.2 IMPLICATIONS

The findings of this thesis study support the existing literature regarding spectral disease indices and plant diseases. The correlations found during this thesis study are moderate. Given the circumstances under which the study was performed, these correlations are enough evidence that brown rust on winter barley can be detected using remote sensing techniques – or more specifically; using spectral vegetation indices.

Though this research did not succeed to identify the specific wavelengths for a well-performing, accurate disease index for winter barley brown rust possible, it is not an insignificant contribution to this purpose. First of all, the spectral signatures characteristic for the different stages of this fungal disease give a clear first impression of which spectral regions could well be relevant for further research to this topic. Secondly, from the redundancy matrices presented in the results of the second research question, the best band combinations for the particular hyperspectral dataset of this study could be retrieved. This information is a proper starting point for future research. Lastly, the prediction models using the index values as predictors show promising results as correlations for each index type became stronger.

8.3 LIMITATIONS

There are several major factors influencing the reliability of the results, most are related to the data collection. Firstly, the hyperspectral data itself has some restrictions. The two hyperspectral datasets used, consisted of a modest number of 16 bands in the spectral range covering wavelengths in the red, red edge and near-infrared region. However, without known cause, the sensor settings of the second flight are divergent – causing different wavelengths to be assigned to the bands. Also, due to the limited spectral range, the methodological choices in relation to vegetation indices used for this study were constrained to indices covering bands within the red to near-infrared spectral range; indices using for example bands in the blue could not be included.

Regarding the validation data, for this research the provided brown rust scores have been assumed to be unbiased and accurate. All brown rust scorings were performed by a breeding company on the same day. However, if different employees have participated in this task – how skilled they may be, the scorings might be

slightly biased. Performing these kind of disease assessments is a skill, which is not mastered at the same level by everyone. Naturally, this would affect the statistical analysis.

The hyperspectral data used and the validation data were collected two weeks apart. Ideally, this would have been on the same day, as both the growth stage of the crop and disease itself develop over time – fortunate, the two moments of data collection fall within the same development stage of the fungus. Thereby, the external variability increases as the moment of data collection of both datasets is further apart – think for example of the influence of lodging and brackling.

The external variability is a point of attention itself. The number of factors influencing the mean reflection values for the different bands per plot – starting point for the analysis performed in this research – is large. For example, the spectrally measurable physiological changes typical for an infection with brown rust, may very well have other causes – including other diseases. These causes should be ruled out as much as possible in further studies to this subject.

9. CONCLUSION

This thesis study aimed to determine the relevance of phenotyping efforts using UAV-RSPs relative to conventional phenotyping efforts for the detection of winter barley brown rust. With the correlations found during this research – though moderate – it can be concluded that UAV-RSPs have the potential of becoming very important for the detection of winter barley brown rust in the future. Index values of existing vegetation indices – the NDVI, PVI and SAVI – showed moderate Pearson correlations with the validation brown rust scores. Further analysis on the potential of the available 16 narrow bands has led to stronger correlations. From the lambda-lambda – redundancy – matrices, the best 30 band combinations were read; after training the data using the index values of indices based on these band combinations, it appeared that the orthogonal index values performed best. After training the data with the 30 best performing orthogonal indices, the predicted brown rust scores of the test set and brown rust scores from the validation data had a correlation coefficient of 0.517.

Though the results are promising, there currently are conditions that do not contribute to the potential of UAV-RSPs in the detection of winter barley brown rust. Most have to do with the pre-processing and research set-up. Concerning the pre-processing of the data, much attention should be paid to automation of outlier detection and the positioning of shapefiles or polygons on the imagery of the crop plots. The winter barley plots are not in a straight grid, meaning that the positioning of the shapefiles for this thesis was a manual task. If the positioning of a shapefile would be a few centimetres off, the mean reflection is influenced by bare soil pixels – this would affect the statistical analysis negatively. Writing an algorithm for automatic plot detection is necessary to bring phenotyping using UAV-RSPs into practice – this is a study on itself. Note that for this research, merely the mean reflections per winter barley plot were used for the analysis. Future research might best include a study to the spreading of reflection values within each plot, this would help characterizing the spreading of the disease over time as well.

Regarding the research set-up, factors that help improving the results of further research on this topic are evident. Most importantly, the size of the hyperspectral dataset should be increased, both in number of bands – or at least spectral regions – and years covered. The latter is very important; as Aesen, Gnyp et al. (2014) stated, in one single correlation or redundancy matrix, a band combination or range might appear to be insignificant for index construction. However, after combining multiple matrices from different years, bands may start to show the information they actually contain. From a multi-temporal dataset, several vegetation indices and regression models can be derived. During this thesis, it was not possible to combine multiple matrices, which has been a limiting factor during the analytical phase. The size of the dataset in spectral bands is important as well. In order to actually formulate a specific disease index such as a winter barley brown rust index, the search for information on more wavelengths than those that were available for this particular study should be continued. Attention should be paid to pre-setting the sensor bands of the hyperspectral camera to relevant – in this case lower – wavelengths. The first suggestion based on previous literature would be to use the highest possible band under 1000 nm as in the study of Mahlein, Steiner et al. (2010), the differences in reflection values between healthy and rust infected crop would increase. Secondly, their research showed a difference as well around 465 nm, meaning that for further research on disease detection, preferably both the green and blue spectrum are represented as well. A spectroradiometer could help identifying significant wavelengths as well for this particular matter.

In addition to the above mentioned, the external variability should be reduced as much as possible. Perhaps, first there should be done more research on the external variability itself. Strongly influencing external variability might originate from the object – in this case a crop – itself. For example, the different genotypes were not given much attention in this study, while their spectral signatures may vary. On top of that, there are other factors that may cause the same spectrally measurable physiological symptoms or changes as implied by the fungal disease brown rust. Another origin for external variability is the circumstances under which the data is collected. Within an hour, weather conditions can change as such – in any case the position of the sun – that it affects the data.

Regarding the validation data, this would in future research better be collected at the time of the UAV-flight, or at least not two weeks from this moment. The same accounts for the collection of data on for example lodging, brackling or other external variables that future researchers wish to account for. For example, if the scoring of lodging and brackling was performed too early, the influence of these variables may have changed at the time of the flight – the scorings then are no longer accurate. Regarding the collection of the validation data; if this task is performed by more than one person, this should be documented. As involving multiple employees – each bringing their own bias – might result in increased variance within the data, knowing which employee scored which group of plots is essential to explain this variance. An even better option would be to test the reproducibility of the employees performing the assessments (Steddom, Bredehoeft et al. 2005).

Lastly, accounted should be for potential other causes for the spectrally measurable symptoms that are identical to those of a brown rust infection – think of loss in water content and decreased photosynthesis. Other causes may for example be other diseases, but also weather .

This thesis' research offers a first step in the identification of important wavelengths and index types for the purpose of classifying brown rust on winter barley. The spectral regions that have proven to be important, match with the spectral regions identified found relevant in previous research (Mahlein 2010). Furthermore, this research helped identify important facets for future research to this topic.

10. REFERENCES

- Aasen, H., M. L. Gnyp, Y. Miao and G. Bareth (2014). "Automated Hyperspectral Vegetation Index Retrieval from Multiple Correlation Matrices with HyperCor." *Photogrammetric Engineering & Remote Sensing* **80**(8): 785-795.
- Araus, J. L. and J. E. Cairns (2014). "Field high-throughput phenotyping: the new crop breeding frontier." *Trends in Plant Science* **19**(1): 52-61.
- Bajwa, S. and S. Kulkarni (2011). *Hyperspectral Data Mining*.
- Bannon, D. (2009). "Cubes and slices." *Nature Photonics* **3**: 627.
- Baret, F. and G. Guyot (1991). "Potentials and limits of vegetation indices for LAI and APAR assessment." *Remote Sensing of Environment* **35**(2): 161-173.
- Barnes, E. M. C., T.R.; Richards, S.E.; Colaizzi, P.D.; Haberland, J.; Kostrzewski, M.; Waller, P.; Choi, C.; Riley, E.; Thompson, T.; Lascano, R.J.; Li, H.; Moran, M.S. (2000). Coincident detection of crop water stress, nitrogen status and canopy density using ground based multispectral data *Proceedings of the Fifth International Conference on Precision Agriculture*. Madison, USA, 2000 ASA-CSSA-SSSA.
- Berryman, C. A., D. Eamus and J. F. Farrar (1991). "Water relations of leaves of barley infected with brown rust." *Physiological and Molecular Plant Pathology* **38**(6): 393-405.
- Blackburn, G. A. (1998). "Quantifying Chlorophylls and Carotenoids at Leaf and Canopy Scales: An Evaluation of Some Hyperspectral Approaches." *Remote Sensing of Environment* **66**(3): 273-285.
- Broge, N. H. and J. V. Mortensen (2002). "Deriving green crop area index and canopy chlorophyll density of winter wheat from spectral reflectance data." *Remote Sensing of Environment* **81**(1): 45-57.
- CABI. (2018). "Plantwise Technical Factsheet - barley brown rust (*Puccinia hordei*)." from <https://www.plantwise.org/KnowledgeBank/Datasheet.aspx?dsid=45803>.
- Chang, C. I. S., T.L.; Du, Q. (1997). Eigen-analysis based band prioritization approach to band selection for hyperspectral image classification. R. S. S. a. I. P. Laboratory. Baltimore County.
- Chein, I. C., D. Qian, S. Tzu-Lung and M. L. G. Althouse (1999). "A joint band prioritization and band-decorrelation approach to band selection for hyperspectral image classification." *IEEE Transactions on Geoscience and Remote Sensing* **37**(6): 2631-2641.
- Chuvieco, E. (2016). *Fundamentals of satellite remote sensing : an environmental approach*. Boca Raton, CRC Press, Taylor & Francis Group.
- Daughtry, C. S. T., C. L. Walthall, M. S. Kim, E. B. de Colstoun and J. E. McMurtrey (2000). "Estimating Corn Leaf Chlorophyll Concentration from Leaf and Canopy Reflectance." *Remote Sensing of Environment* **74**(2): 229-239.
- David, D., J.-B. Jose, J. Hamlyn, S. Xavier and F. Robert (2014) "Proximal Remote Sensing Buggies and Potential Applications for Field-Based Phenotyping." *agronomy* **4**, 349-379 DOI: 10.3390/agronomy4030349.
- Elvidge, C. D. and Z. Chen (1995). "Comparison of broad-band and narrow-band red and near-infrared vegetation indices." *Remote Sensing of Environment* **54**(1): 38-48.
- EPPN. (2017). "Why do we need plant phenotyping?" Retrieved 26 September 2018, 2018, from <http://www.plant-phenotyping-network.eu/>.
- Furbank, R. T. and M. Tester (2011). "Phenomics--technologies to relieve the phenotyping bottleneck." *Trends in plant science* **16**(12): 635-644.
- Gilabert, M. A., J. González-Piqueras, F. J. García-Haro and J. Meliá (2002). "A generalized soil-adjusted vegetation index." *Remote Sensing of Environment* **82**(2): 303-310.
- Guijun Yang, J. L., Chunjiang Zhao, Zhenhong Li, Yanbo Huang, Haiyang Yu, Bo Xu, Xiaodong Yang, Dongmei Zhu, Xiaoyan Zhang, Ruyang Zhang, Haikuan Feng, Xiaoqing Zhao, Zhenhai Li, Heli Li, Hao Yang (2017). "Unmanned Aerial Vehicle Remote Sensing for Field-based Crop Phenotyping: Current Status and Perspectives." *Frontiers in Plant Science* **8**(1111).
- Heim, R. H. J., I. J. Wright, A. P. Allen, I. Geedicke and J. Oldeland (2019). "Developing a spectral disease index for myrtle rust (*Austropuccinia psidii*). " *Plant Pathology* **68**(4): 738-745.
- Hillnhütter, C., A. K. Mahlein, R. A. Sikora and E. C. Oerke (2011). "Remote sensing to detect plant stress induced by *Heterodera schachtii* and *Rhizoctonia solani* in sugar beet fields." *Field Crops Research* **122**(1): 70-77.
- Huete, A., K. Didan, T. Miura, E. P. Rodriguez, X. Gao and L. G. Ferreira (2002). "Overview of the

radiometric and biophysical performance of the MODIS vegetation indices." Remote Sensing of Environment **83**(1): 195-213.

Huete, A. R. (1988). "A soil-adjusted vegetation index (SAVI)." Remote Sensing of Environment **25**(3): 295-309.

Huete, A. R. and R. D. Jackson (1987). "Suitability of spectral indices for evaluating vegetation characteristics on arid rangelands." Remote Sensing of Environment **23**(2): 1-232.

Jones, H. G., R. Serraj, B. R. Loveys, L. Xiong, A. Wheaton and A. H. Price (2009). "Thermal infrared imaging of crop canopies for the remote diagnosis and quantification of plant responses to water stress in the field." Functional Plant Biology **36**(11): 978-989.

Joshua, N. C., D. Genevieve, G. Anthony, C. Randy and M. Susan (2013) "Next-generation phenotyping: requirements and strategies for enhancing our understanding of genotype-phenotype relationships and its relevance to crop improvement." Theoretical and Applied Genetics **126**, 867-887 DOI: 10.1007/s00122-013-2066-0.

Kerr, J. T. and M. Ostrovsky (2003). "From space to species: ecological applications for remote sensing." Trends in Ecology & Evolution **18**(6): 299-305.

Lalic, A. N., Dario; Kovacevic, Josip; Drezner, Georg; Babic, Darko; Abicic, Ivan; Dvojkovic, Kresimir (2006). "Genetic gain and selection criteria effects on yield and yield components in barley (*Hordeum vulgare* L.)." Periodicum Biologorum **112**(3).

Liu, Q., Y. Gu, S. Wang, C. Wang and Z. Ma (2015). "Canopy Spectral Characterization of Wheat Stripe Rust in Latent Period." Journal of spectroscopy **2015**(2): 18-18.

Mahlein, A.-K., E.-C. Oerke, U. Steiner and H.-W. Dehne (2012). "Recent advances in sensing plant diseases for precision crop protection." European Journal of Plant Pathology : Published in cooperation with the European Foundation for Plant Pathology **133**(1): 197-209.

Mahlein, A.-K., U. Steiner, C. Hillnhütter, H.-W. Dehne and E.-C. Oerke (2012) "Hyperspectral imaging for small-scale analysis of symptoms caused by different sugar beet diseases." plant methods **8**, 3 DOI: 10.1186/1746-4811-8-3.

Mahlein, A. (2010). Detection, identification, and quantification of fungal diseases of sugar beet leaves using imaging and non-imaging hyperspectral techniques. Doctor Dissertation, Rheinischen Friedrich-Wilhelms-Universität.

Mahlein, A. K. (2016). "Plant disease detection by imaging sensors - Parallels and specific demands for precision agriculture and plant phenotyping." Plant Disease **100**(2): 241-254.

Mahlein, A. K., T. Rumpf, P. Welke, H. W. Dehne, L. Plümer, U. Steiner and E. C. Oerke (2013). "Development of spectral indices for detecting and identifying plant diseases." Remote Sensing of Environment **128**: 21-30.

Mahlein, A. K., U. Steiner, H. W. Dehne and E. C. Oerke (2010). "Spectral signatures of sugar beet leaves for the detection and differentiation of diseases." Precision Agriculture **11**(4): 413-431.

Melville, A. S. S. C. (1979). Brown rust of barley. Edinburgh, Ministry of Agriculture, Fisheries and Food.

Milton, E. J., M. E. Schaepman, K. Anderson, M. Kneubühler and N. Fox (2009) "Progress in field spectroscopy." Remote Sensing of Environment **113** (2009) Suppl.1.

Mirosavljević, M., N. Pržulj, P. Canak, V. Momčilović, V. Aćin, B. Jocković, N. Hristov and N. Mladenov (2015) "Relationship between grain yield and agronomic traits in winter barley." ratarstvo i povrtarstvo **52**, 74-79 DOI: 10.5937/ratpov52-7860.

Moshou, D., C. d. Bravo, J. West, S. Wahlen, A. McCartney and H. Ramon (2004). "Automatic detection of 'yellow rust' in wheat using reflectance measurements and neural networks." Computers and Electronics in Agriculture **44**(3): 173-188.

Peng, G., P. Ruiliang, G. S. Biging and M. R. Larrieu (2003). "Estimation of forest leaf area index using vegetation indices derived from Hyperion hyperspectral data." IEEE Transactions on Geoscience and Remote Sensing **41**(6): 1355-1362.

Pettorelli, N., J. O. Vik, A. Mysterud, J.-M. Gaillard, C. J. Tucker and N. C. Stenseth (2005). "Using the satellite-derived NDVI to assess ecological responses to environmental change." Trends in Ecology & Evolution **20**(9): 503-510.

Preet, P. S. B., S.; Jayadeva (2015). Feature Selection for classification of hyperspectral data minimizing a tight bound on the VC dimension. I. I. o. T. D. D. o. C. S. Department of Electrical Engineering, Indian Institute of Technology Delhi.

Przulj, N., V. Momcilovic, M. Mirosavljevic and J. Simic (2014). "Effect of growing season and variety on quality of spring two-rowed barley." Genetika **46**(1): 59-73.

Qi, J., A. Chehbouni, A. R. Huete, Y. H. Kerr and S. Sorooshian (1994). "A modified soil adjusted

vegetation index." Remote Sensing of Environment **48**(2): 119-126.

Richards, J. H. X., J. (2006). Remote Sensing Digital Image Analysis, Springer-Verlag Berlin Heidelberg.

Richardson, A. J. W., C.L. (1977). Photogrammetric Engineering and Remote Sensing **43**(12): 1541-1552.

Richardson, J. A. and L. C. Wiegand (1978). Distinguishing Vegetation from Soil Background Information.

Sankaran, S., L. R. Khot, C. Z. Espinoza, S. Jarolmasjed, V. R. Sathuvalli, G. J. Vandemark, P. N. Miklas, A. H. Carter, M. O. Pumphrey, N. R. Knowles and M. J. Pavék (2015). "Low-altitude, high-resolution aerial imaging systems for row and field crop phenotyping: A review." European Journal of Agronomy **70**: 112-123.

Steddom, K., M. W. Bredehoeft, M. Khan and C. M. Rush (2005). "Comparison of Visual and Multispectral Radiometric Disease Evaluations of Cercospora Leaf Spot of Sugar Beet." Plant Disease **89**(2): 153-158.

Te-Ming, T., C. Chin-Hsing, W. Jiunn-Lin and I. C. Chein (1998). "A fast two-stage classification method for high-dimensional remote sensing data." IEEE Transactions on Geoscience and Remote Sensing **36**(1): 182-191.

Thenkabail, P., I. Mariotto, M. Gumma, E. M. Middleton, D. R. Landis and K. Fred Huemmrich (2013). Selection of Hyperspectral Narrowbands (HNBS) and Composition of Hyperspectral Twoband Vegetation Indices (HVI) for Biophysical Characterization and Discrimination of Crop Types Using Field Reflectance and Hyperion/EO-1 Data.

Thenkabail, P. S., E. A. Enclona, M. S. Ashton, C. Legg and M. J. De Dieu (2004b). "Hyperion, IKONOS, ALI, and ETM+ sensors in the study of African rainforests." Remote Sensing of Environment **90**(1): 23-43.

Thenkabail, P. S., E. A. Enclona, M. S. Ashton and B. Van Der Meer (2004a). "Accuracy assessments of hyperspectral waveband performance for vegetation analysis applications." Remote Sensing of Environment **91**(3-4): 354-376.

Thenkabail, P. S. and J. G. Lyon (2012). Hyperspectral remote sensing of vegetation. Boca Raton, FL, CRC.

Thenkabail, P. S., R. B. Smith and E. De Pauw (2000). "Hyperspectral Vegetation Indices and Their Relationships with Agricultural Crop Characteristics." Remote Sensing of Environment **71**(2): 158-182.

Thomas, S., M. T. Kuska, D. Bohnenkamp, A. Brugger, E. Alisaac, J. Behmann, A. K. Mahlein and M. Wahabzada (2018). "Benefits of hyperspectral imaging for plant disease detection and plant protection: a technical perspective." Journal of Plant Diseases and Protection **125**(1): 5-20.

UN. (2017, 21 June 2017). "World Population Prospects: The 2017 Revision." Retrieved 26 September 2018, from <https://www.un.org/development/desa/publications/world-population-prospects-the-2017-revision.html>.

Verhoef, W. (1984). "Light scattering by leaf layers with application to canopy reflectance modeling: The SAIL model." Remote Sensing of Environment **16**(2): 125-141.

White, J. W., P. Andrade-Sanchez, M. A. Gore, K. F. Bronson, T. A. Coffelt, M. M. Conley, K. A. Feldmann, A. N. French, J. T. Heun, D. J. Hunsaker, M. A. Jenks, B. A. Kimball, R. L. Roth, R. J. Strand, K. R. Thorp, G. W. Wall and G. Wang (2012). "Field-based phenomics for plant genetics research." Field Crops Research **133**: 101-112.

Yan, W. and M. S. Kang (2003). GGE biplot analysis : a graphical tool for breeders, geneticists, and agronomists. Boca Raton, Fla., CRC Press.

Zhang, J.-C., R.-I. Pu, J.-h. Wang, W.-j. Huang, L. Yuan and J.-h. Luo (2012). "Detecting powdery mildew of winter wheat using leaf level hyperspectral measurements." Computers and Electronics in Agriculture **85**: 13-23.

Zhang, J., R. Pu, W. Huang, L. Yuan, J. Luo and J. Wang (2012). "Using in-situ hyperspectral data for detecting and discriminating yellow rust disease from nutrient stresses." Field Crops Research **134**: 165-174.

Zohary, D. (1988). Domestication of plants in the old world : the origin and spread of cultivated plants in west Asia, Europe, and the Nile Valley / Daniel Zohary and Maria Hopf. Oxford [Oxfordshire] ; New York, Clarendon Press.

GLOSSARY

Bias

The distance that a statistic describing a given sample has from reality of the population of the sample was taken from.

Biased estimator

In the case of a biased estimator, the sampling distribution is not evenly distributed around the true parameter. The estimator is consistently over- or underestimating. Respectively resulting in a high bias or low bias; the sampling distribution is 'biased' and does not come close to the true sampling distribution. A biased estimator is not desired in statistics.

Coefficient of determination

Abbreviated R^2 . A value usually between 0 and 1, where the latter indicates a perfect fit of the regression predictions on the data. Values outside this range might imply a wrongly chosen model. The predictors are calculated by least-squares regression.

Correlation coefficient (Pearson)

Abbreviated R. A value between 1 (meaning a perfect positive correlation) and -1 (a strong perfect negative correlation; variables move in a perfect opposite direction). Values around 0 represent the weakest correlations. In remote sensing, correlation coefficients are used to determine the strength of a relationship between two bands.

Correlogram

Graph/visualization of a correlation matrix.

Covariance

How values in one band vary with respect to the values of another spectral band. If they vary both in a positive direction for example, they are correlated. Always a comparison between multiple bands. The covariance of a band with itself is the variance.

Dimensionality reduction

A process in which the number of random variables – in remote sensing these would be bands – of consideration is reduced. This is done by obtaining a set of principal variables – which are a subset of the complete set of variables, containing to a large extent the structure and information that is carried by the complete set of variables.

Eigenvalues

Variances of synthetic bands or principal components. These values – the lambda's – are of decreasing value; lambda one is larger than lambda two and so on.

Eigenvectors

Eigenvectors define the direction of the axes of the synthetic bands. So the first eigenvector defines the direction of the first synthetic band or principal component. Eigenvectors should be uncorrelated and perpendicular to each other.

Feature extraction

A dimensionality reduction method involving the

transformation of original hyperspectral data into a projected space, with the risk of crucial and critical information to be compromised and distorted (Chein, Qian et al. 1999).

Feature ranking

The construction and evaluation of an objective matrix based on various criteria such as information divergence, MVPCA and MI (Chein, Qian et al. 1999).

Feature selection

A dimensionality reduction method striving at the discovery of a subset of features which capture the fundamental characteristics of the data, while processing sufficient capacity to discriminate between classes (Chein, Qian et al. 1999).

Fisher's discriminant analysis

Also known as minimum-misclassification canonical analysis (MMCA),

Fitted value

Also known as predicted values; the mean response value that is predicted by a statistical model after the input of the value of the predictor.

Genotype

The combination of characteristics as determined in the genetic material.

Greenness

A composite signal of leaf chlorophyll content, leaf area, canopy cover and canopy structure. This index has a high sensitivity to spatial and temporal variations in greenness. However, it does not help in attempts to differentiate between the possible causes of these variations – may it be for example a change in LAI or leaf chlorophyll content (Chuvieco 2016).

Ground truth

Also known as reference map; in remote sensing it refers to information collected on location.

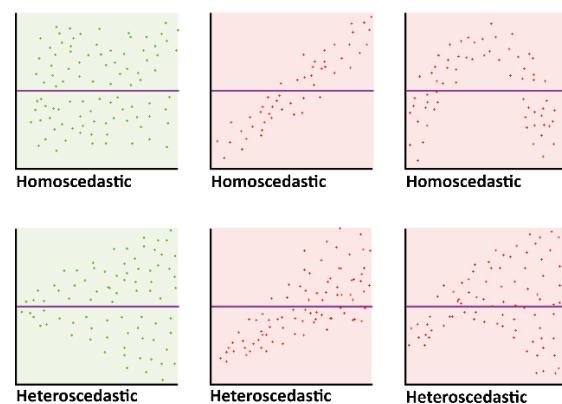


Figure i | Scatterplots of unbiased and biased heteroscedastic and homoscedastic distributed variables. Green graphs concern unbiased data, the red graphs are from biased datasets.

Heteroskedasticity

When the variance of errors given the independent variable of X is not constant. The variance depends on X_i as X_i increases, the magnitude of errors increases.

Homoskedasticity

In case of heteroskedasticity, the variance of errors given the independent variable X is constant. In other words, all errors made by the model are basically constant as X increases.

Hughes effect

Also known as the Hughes phenomenon, peaking paradox or the curse of dimensionality. In 1968, Hughes showed through statistical analysis how the accuracy of a classifier is dependent of the number of training examples/pixels. Many researchers tried to void or reduce the Hughes effect as it has an effect on classification techniques.

Unlike broadband – e.g. Landsat – data, hyperspectral narrowband imagery can have up to hundreds or thousands of spectral bands. This larger amount of spectral bands is very advantageous for complex classification purposes. However, the amount of training pixels required to maintain a decent statistical confidence and functionality for classification purposes grows exponentially with the number of spectral bands. Statistical integrity (1) and class accuracy (2) require enough training pixels to train the classifier (1) and an equally large number of training pixels for each class (2).

Hyperspectral camera

Camera that obtains data (it records spectra) with the aim to identify objects, materials or locate processes. With hyperspectral imaging, contiguous spectral bands are measured. See Annex A, figure A for an illustration.

Information divergence

Measurement of the difference between two – nonnegative – matrices.

Lambda to lambda plot

Redundancy matrices, calculations of correlations between all wavelength pairs of the dataset; the calculated value represents the degree of redundancy between the two wavelengths (Aasen, Gnyp et al. 2014).

Loadings

All elements of the eigenvectors.

Lodging

The bending of a crop's stem around ground level, it is a permanent displacement that makes it difficult or impossible to harvest the crop. Difference is made between stem and root lodging. The latter is caused by a failing root system, whereas stem lodging can be caused by high winds and heavy rainfall.

Linear orthogonal transformation

A principal component analysis is an example of a linear orthogonal transformation. The result of a linear orthogonal transformation of spectral bands is a set of uncorrelated variables or 'synthetic bands', a linear combination of all input spectral bands. These bands contain 'new' spectral information in a decreasing order from band 1 to band n . The last synthetic

bands are very noisy, they contain very little spectral information.

In case of a two dimensional analysis, this type of transformation consists of a translation (1), where the origin of the axis system is moved to the centre of all pixel values and a rotation (2) in such a way that the first axis will point into the direction of the largest variation and the second axis into the direction of second largest variation.

Multispectral camera

Camera that obtains data within specific wavelength ranges – which might be separated by filters or by the use of instruments that are sensitive to particular wavelengths – so it measures spaced spectral bands. See Annex A, figure A for an illustration.

Hyperspectral narrowband

Imaging of hyperspectral bands with a narrow (usually 3-10 nm) bandwidth. The amount of bands in a hyperspectral image varies; from hundreds to thousands.

Neckling

Situation where the ears (of the winter barley stem) drop off.

Null hypothesis

The null hypothesis states that there is no relationship between two variables. Generally this hypothesis is a default assumption until the opposite is proved.

Orthomosaic

An aerial photograph which is geometrically corrected (or "orthorectified") in such a way that the scale is uniform, meaning that the photo does not have more distortions than a map. Also known as orthophoto, orthophotograph or orthoimage.

Phenotype

The combination of characteristics that are formed with the influence of external factors on the phenotype (EPPN 2017).

Phenotyping

Accurate and rapid acquisition of phenotypic information of plants or cells in different environments.

Phenomics

Rapid high-throughput crop phenotyping

Principal Component Analysis

Also known as the Karhunen-Loeve Transform, a decorrelation technique that is widely used for data compression and interpretation. It transforms data coordinates in such a fashion that the first principal component vector is along the direction of maximum variance. It then maximizes the variance in successive components (Chein, Qian et al. 1999, Richards 2006). Principal Component Analysis is done for the purpose of data reduction (1), visual interpretation – as the first three synthetic bands or principal components provide most of the information and contain more than 95% of the variation – (2) and improvement of image analysis – e.g. redundancy can decrease the separability of classes. See the definition of *linear orthogonal transformation* as well.

Random Forest

Random forest – or ‘random decision forest’ – is a powerful supervised machine learning algorithm. It is suited for performing both progression and classification tasks. It operates by constructing a multitude of decision trees during training and – in classification – giving the mode of the different classes as the output class; in regression this would be the mean prediction of the individual trees.

Real-time kinematic (RTK)

Real-time kinematic (RTK) positioning is a satellite navigation technique used to enhance the precision of position data derived from satellite based positioning systems (global navigation satellite systems, GNSS) such as GPS, GLONASS, Galileo, and BeiDou.

Redundancy

The amount of variance of a variable that is explained by another independent variable. The higher the redundancy, the higher the ability to predict. In remote sensing, redundancy reduction of spectral bands is highly desirable.

Regression analysis

Estimating the relationship among multiple variables by the use of statistical processes.

(Regression) error

In regression, errors and residuals are easily confused as they are closely related to each other. The error defines how much the observed value deviates from the true value, for the definition of the residual, see ‘Residual’ below in the glossary.

Regression line

On the regression line, a trend is represented that describes how the response variable – y-axis – changes as the independent variable on the x-axis changes.

Regression residual

Also known as the prediction errors. The difference between an observed value of the dependent variable and the predicted value is a residual. Each data point has a residual. The residual is calculated as follows: observed value - predicted value. The sum and the mean of the residuals both equal to zero. Residuals are measured to determine how far the values are from the regression line.

Residual

In statistics, a residual is the difference between the observed value and the mean value that is predicted by a model for that observation. In regression, residual values are useful as they indicate to which extent in a certain model is accounted for in the variation in observed data.

Root mean square error

Root Mean Square Errors (RMSEs) measure how spread out the residuals around the regression line are; it is the square root of the variance of the residuals. The RMSE has the same unit as the response variable and shows how close observed values are to the models predicted values. A lower RMSE indicates a better fit.

Spectroscopy

In spectroscopy, the absorption and emission of light – and other radiation – by the matter of interest is studied with relation to the dependency of these processes on the radiation wavelength.

Signal to noise ratio

In this ratio, the level of a desired signal is compared to the level of background noise. When a ratio is higher than 1:1, this indicates the presence of more signal than noise.

Stalk lodging

The breakage of the stalk below the ear (crop).

Standard deviation

Tells something about the spread around the mean value. Technological (plant) traits

Unbiased estimator

In this case, the sampling distribution is evenly distributed around the true parameter; it is not over- or underestimating. The sampling distribution comes close to or equals the true distribution. An unbiased estimator is desired in statistics.

Variance

The spread of values around the mean value of a certain band. Also explained as the difference of every pixel value with the mean value of the band.

Wavelength

The distance between cycles within an electromagnetic wave.

Winter barley

Biennial variation of the cultivated grain *Hordeum vulgare*, which blooms in the second half of May.

ABBREVIATIONS

AGAY

All growth stages, all years

CFS

Correlation based Feature Selection

CSLI

Cercospora Leaf Spot Index

DEM

Digital elevation model

DSM

Digital surface model

FLIR

Forward looking infrared (radar); radiometer

Fv

Grains volume fraction

GNDVI

Green Normalized Vegetation Index

HDI

Hyperspectral vegetation index

ICA

Independent component analysis

IR

Infrared (spectral band/region)

LAI

Leaf Area Index

LiDAR

Light Detection and Ranging

MI

Mutual information

LWI

Leaf Area Index

MMCA

Minimum-misclassification canonical analysis
(also known as Fisher's discriminant analysis)

MRMR

Minimum Redundancy Maximum Relevance

MSAVI(2)

Modified Soil-Adjusted Vegetation Index (2)

MSNRPCA

Maximum-SNR PCA

MVPCA

Maximum-variance principal component analysis

NaN

Not a number

NDSI

Normalized Difference Snow Index

NDVI

Normalized Difference Vegetation Index NIR/RED

NDRE

Normalized Difference Red Edge

NIR

Near-Infrared (spectral band/region)

NSI

Nitrogen Stress Index

OHM

Object height model

OSP

Orthogonal-subspace projection

PCA

Principal component analysis

PPP

Public Private Partnership

PP

Projection pursuit

PRI

Photochemical Reflectance Index

PVI

Perpendicular Vegetation Index

R

Coefficient of correlation

R²

Coefficient of determination

R(ED)

Red (spectral band/region)

RGB

Red Green Blue (spectral bands/regions)

RMSE

Root Mean Square Error

RTK

Real-time kinematic (positioning)

SAIL

Scattered by arbitrary inclined leaves

SAVI

Soil-Adjusted Vegetation Index

SDI

Spectral Disease Index

SGAY

Single growth stage, all years

SGSY

Single growth stage, single year

SNR or S/N

Signal-to-noise ratio.

SR

Simple Ratio

SVI

Spectral Vegetation Index

SVM

Support Vector Machine

TSAVI

Transformed Soil-Adjusted Vegetation Index

UAV

Unmanned aerial vehicle

UAV-RSP

Unmanned aerial vehicle remote sensing platform

VI

Vegetation Index

WENR

Wageningen Environmental Research

WUR

Wageningen University & Research

ABBREVIATIONS OF STATISTICAL TERMS

n	Sample size
SD	Standard deviation
S²	Variance
cov(X,Y)	Covariance
R	(Pearson) correlation coefficient
R²	Coefficient of determination

11. LIST OF FIGURES

Figure 1 Relationship between the environment, genotype and phenotype.	4
Figure 2 WENR flying with the UAV-RSP above the winter barley plots at the location of Rilland (Limagrain)... 7	7
Figure 3 Healthy winter barley versus brown rust infected leaves (source: Bayer Crop Science, FarmingUK.com).	8
Figure 4 Phylogenetic relationships among seven crop plants among which barley (<i>Hordeum vulgare</i>). Tree is built based on information from the Taxonomy database of the National Center for Biological Information (ncbi.nlm.nih.gov/taxonomy).	10
Figure 5 Leaves infected with barley brown rust (Bayer Crop Science).	11
Figure 6 A leaf's lost ability to maintain favourable water status attributed by tears in the cuticle - which has a protective and hydrophobic function when intact (source: author).	12
Figure 7 Spectral signatures of sugar beet in healthy or diseased condition (source: Anne-Katrin Mahlein, Institute of Sugar Beet Research, University of Göttingen). Divergent reflectances marked with red circles.	12
Figure 8 Illustrative example of hyperspectral and multispectral imaging (source: author).	13
Figure 9 Example of an hyperspectral image cube with two spatial dimensions (x, y) and multiple wavelengths (z) (Bannon 2009).	13
Figure 10 Typical spectral signatures of healthy (green) vegetation, senescent (brown) vegetation and the soil. The R and NIR regions are indicated; most vegetation indices are based on these two bands (Chuvieco 2016).	14
Figure 11 Structure of vegetation spectra plotted in the R-NIR reflectance space (Source: Alfredo Huete). The peak vegetation – indicating very dense green vegetation – and the soil line are marked in red. Note that direction of the soil line depends on the dataset.	14
Figure 12 Multi-scale model integrating observations of the plant-pathogen interaction from the microscope up to airborne imaging (Thomas, Kuska et al. 2018).	18
Figure 13 These graphs show the spectral signatures from different nitrogen levels of a dataset of stem elongation stage in 2012 (left) and lambda by lambda correlation plots for biomass (right). High values (dark color) indicate that the wavelength which is set as the independent variable has high predictive value over the dependent wavelength. The red rectangles in the lower right graph indicate the main differences of before and after the detector offset in the correlation plots (Aasen, Gnyp et al. 2014).	21
Figure 14 Plots of biomass against the NDI values derived from the MCMS and direct approach together with their regression models: (a) tillering stage (b) stem elongation stage, (c) heading stage and across all stages (d) (Aasen, Gnyp et al. 2014).	22
Figure 15 Location of the winter barley plots at Rilland, Zeeland (source: Aurea Imaging).	24
Figure 16 Timeline marked with the collection of hyperspectral data (green) and validation brown rust, lodging and brackling scores (orange). The main development phases of the brown rust disease is indicated below the timeline.	24
Figure 17 LiDAR imagery of the winter barley plots, produced by WENR the 26 th of June. On this imagery, the flattening effects of lodging and brackling become evident. Naturally, affected plots containing lodged or brackled crops have a very divergent spectral signature.	25
Figure 18 Illustration of the Excel sheet with validation data provided by Limagrain Nederland BV. The brown rust scores are given in the second to last column of this screenshot.	26
Figure 19 Not all plots contained a full set of brown rust, lodging and/or brackling scores.	28

Figure 20 Several plots were not fully covered by the hyperspectral imagery (this figure concerns the imagery of the flight executed on the 14th of June 2017).	28
Figure 21 Mean reflections per band for each of the given brown rust scores; wavelengths are visualized in nm, mean reflectance indicated in variation between 0 and 1. The histogram included in the figure illustrates the amount of observations that were made for each brown rust score visualized in the line graph. The line graph shows that the mean reflectances per brown rust score are ‘flipped around’ in the near-infrared region – with an exception for the reflections of the plots scored with a brown rust score that was given relatively few times as reflectances of plots with scores of 1, 7 and 8 diverge from this trend evidently.	32
Figure 22 Scatterplot of the PVI values against the brown rust scores of plots scored with a score of 1 for lodging. The concerning plots are indicated in orange on the overview map that is provided with the graph. The markers of the scatterplot show a reasonable spread, however a trend is clearly visible along the regression line.	35
Figure 23 Histogram and scatterplot of the residuals, meaning the observed – fitted values, of the regression model on the PVI values and brown rust scores of the plots scored with 1 for lodging.	35
Figure 24 Lambda-lambda (coefficient of determination R^2) contour plot showing the R^2 values of the normalized difference (ND) index values ~ brown rust scores. This plot is created using the 16 band hyperspectral data retrieved at the 14 th of June 2017. The axes are provided with the narrowband wavelengths and band numbers. The legend shows the spreading of the R^2 values. All band combinations with the value ‘NaN’, show no correlation with the brown rust scores, and therefore have no R^2 value either.	37
Figure 25 Lambda-lambda (coefficient of determination R^2) contour plot showing the R^2 values of the orthogonal index values ~ brown rust scores. This plot is created using the 16 band hyperspectral data retrieved at the 14 th of June 2017. The axes are provided with the narrowband wavelengths and band numbers. The legend shows the spreading of the R^2 values.	37
Figure 26 Lambda-lambda (coefficient of determination R^2) contour plot showing the R^2 values of the soil-adjusted index values ~ brown rust scores. This plot is created using the 16 band hyperspectral data retrieved at the 14 th of June 2017. The axes are provided with the narrowband wavelengths and band numbers. The legend shows the spreading of the R^2 values.	38

12. LIST OF TABLES

Table 1 Examples of biophysical and biochemical variables present in crops which are measurable through hyperspectral remote sensing (Mahlein 2010).....	16
Table 2 Results of MCMS (grey) and direct approach (white). For both calibration and validation are given: the coefficient of determination (R^2), standard error of the estimate (SEE) and the root mean square error (RMSE). The exponential regression model results are only achieved mentionable for the ‘Across all stages’ dataset (Aasen, Gnyp et al. 2014).	23
Table 3 The sensor settings for both Rikola flights above Rilland in June of 2017 are divergent; reflectance is measured at different wavelengths. Closely spaced wavelengths of the two flights are highlighted – they are of particular interest in attempting to study the spatio-temporal development of the disease (SRQ3).	25
Table 4 Hyperspectral bands and associated wavelengths used for RED, RED edge and NIR spectral regions used for calculating the index values of the indices indicated in table 5.	28
Table 5 Explanation of the indices used for addressing the first sub-research question.	28
Table 6 Workflow addressing sub-research question two.	30
Table 7 The method leading the results for sub-research question two.....	31
Table 8 Correlation coefficients, coefficients of determination and root mean square errors of the indices and brown rust scores. Results are shown for six different plot selections – see column headers. Note that all plots were scored for brackling, therefore no separate selection was necessary for calculations.	33
Table 9 Calculation of the narrowband index values used to make the correlation plots visualized in figures 24-26 and the lambda-lambda plots of figures 27-29 . Band X refers to the band number on the horizontal axes of these figures, band Y refers to the bands indicated on the vertical axes.....	36
Table 10 Optimal indices according to the lambda-lambda matrices as visualized in the figures 29-31.	38

13. APPENDICES

ANNEX A

Public Private Partnership

Limagrain Nederland BV, Aurea Imaging and the WUR (WENR) collaborate in the context of the developments regarding phenotyping using UAVs in a PPS with an expected time span of four years. The genetic material and reference data provided through the breeding trials executed by Limagrain Nederland BV allow for validation of products derived during remote sensing studies by Aurea Imaging and the WUR.

Table A1 | Parties involved in the Public Private Partnership 'Next generation phenotyping'.

Organization	Location	Involved
Limagrain Nederland BV	Rilland, Zeeland	Piet Reyns, Eva Ampe
Aurea Imaging	Zaventem (België)	Bert Rijk
WUR + WENR	Wageningen, Gelderland	Sander Mûcher, Henk Kramer, Lammert Kooistra, Gert Kooistra, Rick van de Zedde

The first has primarily been aimed at the optimisation of the production of good quality images with hyperspectral, multispectral, LiDAR, RGB and thermal imaging systems - see Table 3 - and first interpretations of the data (quality).

Table A2 | Imaging technologies used for data acquisition during the PPP between the WUR, Aurea Imaging and Limagrain Nederland BV.

Technology	Aurea	WUR
LiDAR	-	RiCopter
Hyperspectral camera	-	RICOLA
Multispectral camera	Sequoia	MUMSY
Thermal camera	FLIR Tau2 640 radiometric	WORKSWE LL WIRIS (tba)
RGB	senseFly S.O.D.A. 20 MP	RiCopter, Phantom 3

For each site, the list of deliverables as defined in Table 5 were formulated. During the first year, these deliverables were improved on their shortcomings and Real Time Kinematic (RTK) or Post Processed Kinematic (PPK). The second year, drone flights were repeated and the data obtained and the focus shifted to the plant traits – while improvements on RTK/PPK and shortcomings continued.

Table A3 | Deliverables and trait focus per technology used in during the PPP.

Technology	Deliverables	Trait focus
LiDAR	DEM, DSM	Biomass, height, lodging
Hyperspectral camera	Georeferenced hyperspectral data cubes	Biomass, disease (brown rust)
Multispectral camera	Multispectral mosaics (including NIR region)	Varying plant responses to a deficiency of nutrients, water stress, diseases (brown rust)
Thermal camera	Thermal images	Diseases (brown rust), water stress, stomatal conductance (leaf temperature)
RGB	RGB coloured LiDAR points, spatially high resolution mosaics with high RTK positioning	Ground cover, plant count, greenness (visible properties)

The years three and four have initially been reserved for the focus on more advanced analysis of complex traits.

Crops of interest in this PPP are maize grain, silo corn and winter barley, all grown at multiple plots in the region of Schouwen (maize grain and silo corn), the municipality of Rilland (winter barley) and the municipality of Reusel (silo corn).

ANNEX B

Main advantages and disadvantages of manual sampling, sampling using ground-based platforms and UAV-RSP sampling (Guijun Yang 2017).

Table B1 | Sampling advantages and disadvantages of manual sampling, ground-based platforms and UAV-RSPs.

Manual Sampling		Ground-based platforms		UAV-RSPs	
+	-	+	-	+	-
Use of human eye	Slow	Fast(er)	No unique “fit for all” platform to phenotype diverse crops	Fast	UAV operation often limited by sensor payload (size/weight), operating altitude and flight time.
	Destructive	Less or non-destructive	Non-simultaneous measurement of plots	Non-destructive	
	Laborious	Non-laborious	Compaction of soil	Non-laborious	
	Costly procedures	Less costly, however cost-effectiveness for rapid field phenotyping still an issue	Vibrations resulting from uneven terrain surfaces	Low operational costs	
			Still issues on adjustment to row and plant spacing, inconsistencies in plot sizes and plant height	Flexible, convenient operation	
		Plot-level data captured with GPS		On-demand access to data	
	Does not allow for phenomics	Allows for phenomics, which may better account for environmental variations		Allows for phenomics, which may better account for environmental variations	
		High spatial resolution		High spatial resolution	
	No benefit from current developments in data-processing algorithms/tool	Allows to benefit from current developments in data-processing algorithms/tools		Allows to benefit from current developments in data-processing algorithms/tools	

Applications of high-resolution aerial sensing in field phenomics (Sankaran, Khot et al. 2015).**Table C1 |** Applications of high-resolution sensing in field phenomics (Sankaran, Khot et al. 2015).

Application	Symptoms/ Parameters	Indicators	Techniques
Plant water stress	<ul style="list-style-type: none"> Reduced stomatal closure Decreased photosynthesis Decreased growth Exacerbation of heat stress (reduced transpirational cooling) 	<ul style="list-style-type: none"> Temperature in leaves (to determine plant tolerance to water stress) Biomass (determine plant growth) 	<ul style="list-style-type: none"> Thermal infrared sensing Multispectral imaging Near-infrared imaging (determine reduced biomass due to water stress)
Plant nutrient deficiency (1) and heat stress (2)	<p>(1)</p> <ul style="list-style-type: none"> Lower chlorophyll content Lower growth rate Tissue necrosis Higher disease susceptibility <p>(2)</p> <ul style="list-style-type: none"> Osmotic stress, stomatal closure Decreased stomatal conductance Increased leaf temperature Decreased photosynthesis 	<ul style="list-style-type: none"> Temperature in leaves Correlation between NSI (nitrogen stress index) and grain yield Correlation between crop senescence index and NDVI Plant primary responses to salinity and heat stress Canopy temperature changes 	<ul style="list-style-type: none"> Visible to near-infrared spectral reflectance (changes in photosynthetic and stomatal conductance) Thermal imaging, possibly combined with RGB imaging (detect plant primary responses to salinity and water stress and canopy temperature changes)
Plant biotic stress	Depending on the diseases/pests development and symptoms	<ul style="list-style-type: none"> Disease severity Susceptibility to diseases of different varieties Assessing/monitoring pathogen in atmosphere 	<ul style="list-style-type: none"> Multispectral imaging (high-resolution) Correlate simple vegetation indices (NDVI, LWI, CLSI) with the disease severity Correlate thermal imaging and PRI to disease severity
Plant growth parameters	<ul style="list-style-type: none"> Emergence + number of emerging plants Plant vigor LAI Biomass Plant maturity Height Grow width Canopy closure 		<ul style="list-style-type: none"> Estimate GNDVI using multispectral imaging (to study emergence/spring) Using false color multiband image to determine (number of) emergence

**Crop yield
potential
assessment**

- Plant flowering date
- Number of heads (seeds) per plant
- Size, volume, weight of plant at time of harvest
- Canopy vigor

Correlating the parameters to the crop yield

- Correlating canopy vigor/winter survival/spring stand to yield potential using GNDVI
- Quantification of large field plots through multispectral imaging

ANNEX D



Figure D1 | The Rikola Snapshot Hyperspectral Camera (source: Senop)

Specifications of the Rikola Snapshot Hyperspectral Camera (Senop)

The Rikola hyperspectral camera was used to obtain the datasets used in this thesis study; it is a spectral system providing snapshot images in the visible and near-infrared spectral range. The pixels it produces are true image pixels – so no interpolation is used. It is a lightweight – 720 grams – and robust camera. The system is currently used in agriculture, forestry, water research and for medical and forensic purposes. For full specifications, see the technical data provided by Senop in the table below.

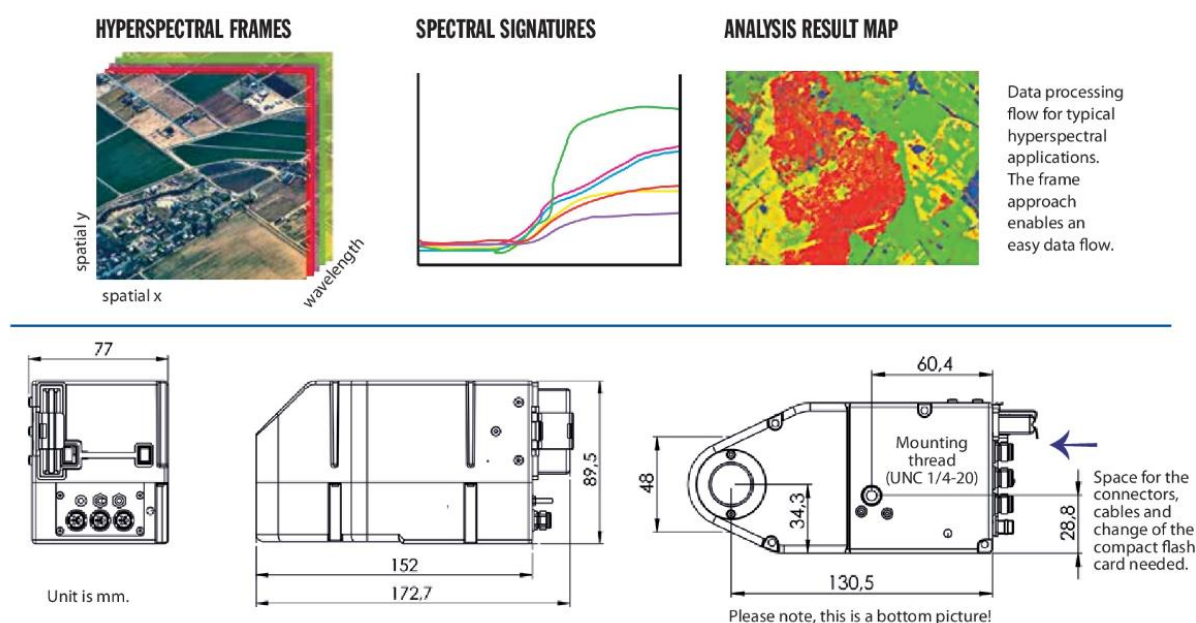


Figure D2 | Technical illustrations of the Rikola camera as provided by its producer Senop.

Table D1 | Specifications of the Rikola Snapshot Hyperspectral camera.

Parameter	Specified value	Remarks
Horizontal FOV	36,5°	
Vertical FOV	36,6°	
F-number	~ 28	
Focal length	~ 9 mm	Camera has fixed optics
Ground pixel	6,5 cm at 100 m altitude	
Default Spectral Range	500-900 nm	Other ranges: 400—700, 450-800 and 550-900
Spectral Resolution	~10 nm, FWHM	Over the range of 500-830 nm

Spectral step	~1 nm	Peak wavelength can be selected by ± 1 nm accuracy
Calibration Unit	Spectral radiance	
Spectral Bands	~ 380° max	The band amount is programmable. The used band amount can be selected between 1-380 for the default range
Image Sensor	CMOS	Pixel size is 5,5 μ x 5,5 μ
Dynamic Range	12 bits	
Exposure Time	0,12-3000 ms	Adjustable
Frame Rate	30 frames/sec	Frame rate with 10 ms exposure time and 1010 - 648 pixels image size
Operational Voltage	7-9 V	7,5 V is recommended
Power Consumption	5,3 W average 10,0 W momentarily	
Weight	~ 720 gram	Without battery, GPS and relative irradiance sensor

Visualizations of the brown rust, lodging and brackling scoring of the plots.

Limagrain employees have scored the plots manually. Low scores represent low severity and high scores a high severity. In theory, scores from 1 to 10 could have been given – however for this Noted should be the not all plots were scored on lodging; merely the EV field (northern/upper part).

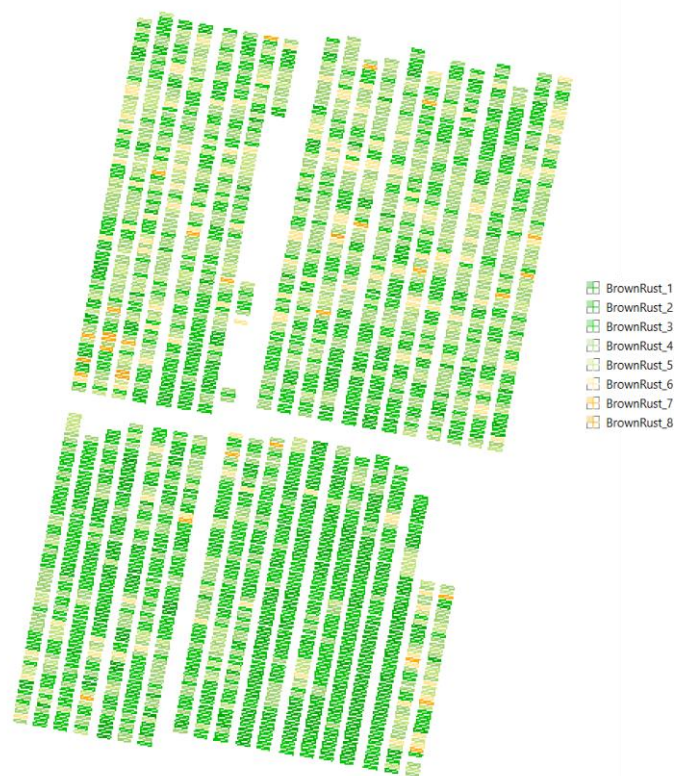


Figure E1 | Brown rust scoring of the winter barley plots at the Limagrain location of Rilland. The scoring was performed at the 30th of May 2017. In total,



Figure E2 | Brackling scoring of the winter barley plots at the Limagrain location of Rilland. The scoring was performed in the period of the 29th of June and the 3rd of July 2017.



Figure E3 | Lodging scoring of the winter barley plots at the Limagrain location of Rilland. The scoring was performed at the 13th of June 2017. Note that merely the upper half of the field was scored for lodging.

ANNEX F

Overview of the different trial fields with winter barley on the Limagrain location of Rilland.

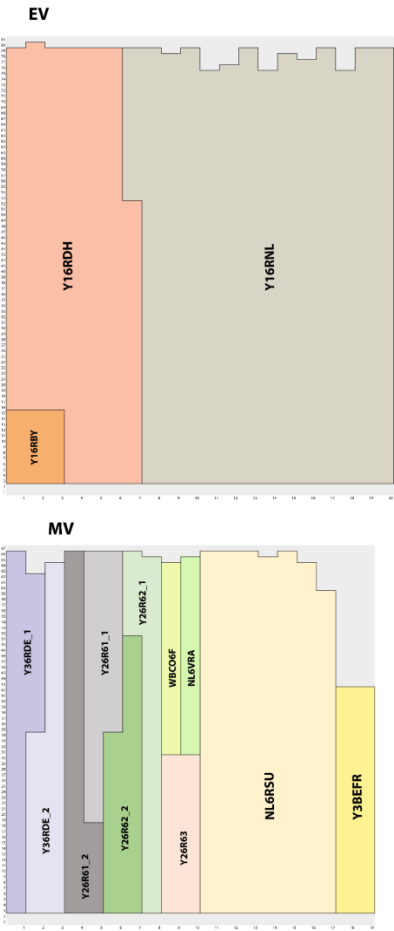


Figure F1 | Top view of the trial fields within the winter barley field. Each trial field is filled with a particular genotype. Plot codes are based on the numbers indicated at the x- and y-axis of the EV and MV fields.



Figure F2 | Top view of the winter barley plots at the Limagrain location of Rilland.

ANNEX G

Reflections per band for brown rust scores for each trial field.

Noted should be the plot count per brown rust score for each of the trial fields. These counts are given below the graphs in a table and help interpret the data. For example, the trial field of Y16RBY has a low total plot count of 39 – which is relatively low, therefore the reflection values of a singular plot have a large effect on the mean values as presented in the graph of this field (figure G1).

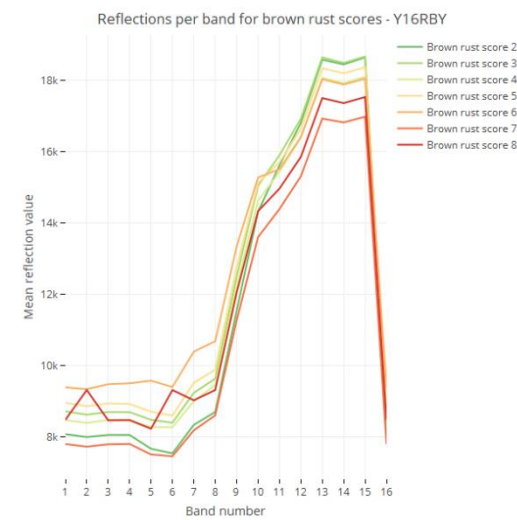


Figure G1 | Y16RBY. Total plot count: 39.

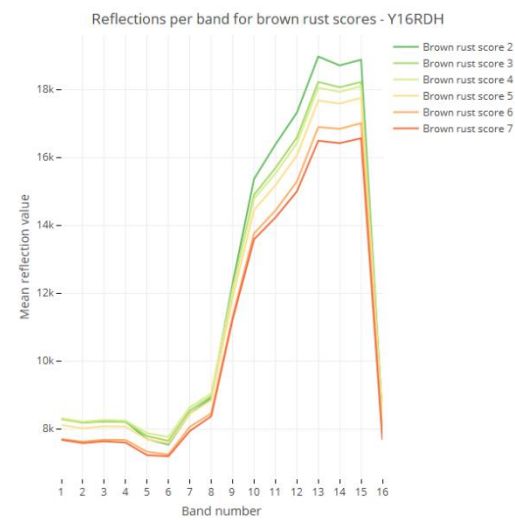


Figure G2 | Y16RDH. Total plot count: 445.

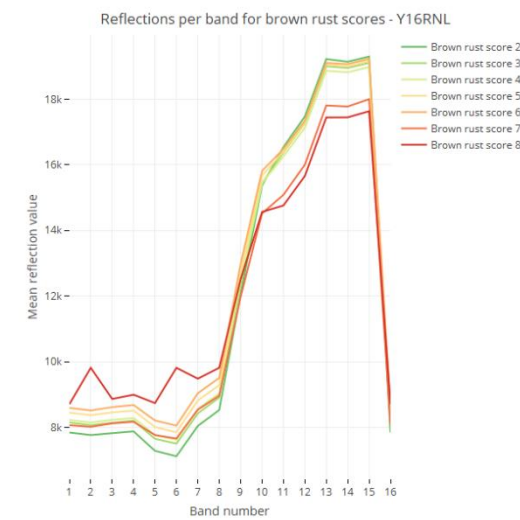


Figure G3 | Y16RNL. Total plot count: 921. Note: merely one plot was scored with a brown rust score of 8.

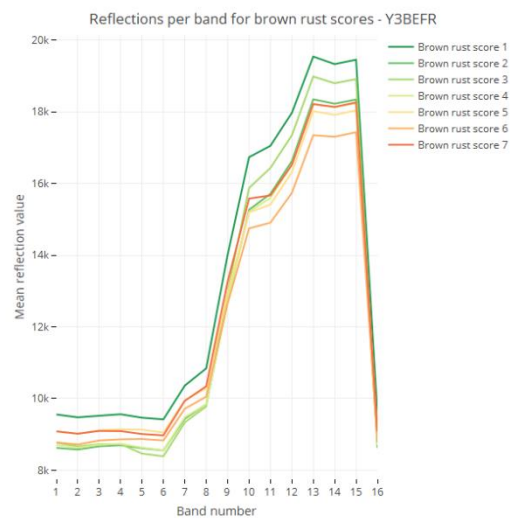


Figure G4 | Y3BEFR. Total plot count: 79

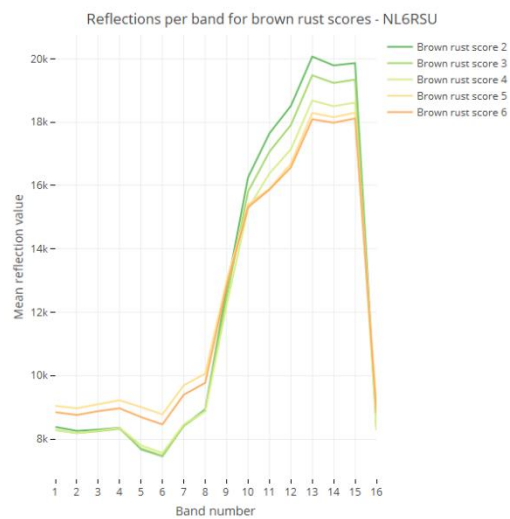


Figure G5 | NL6RSU. Total plot count: 416.

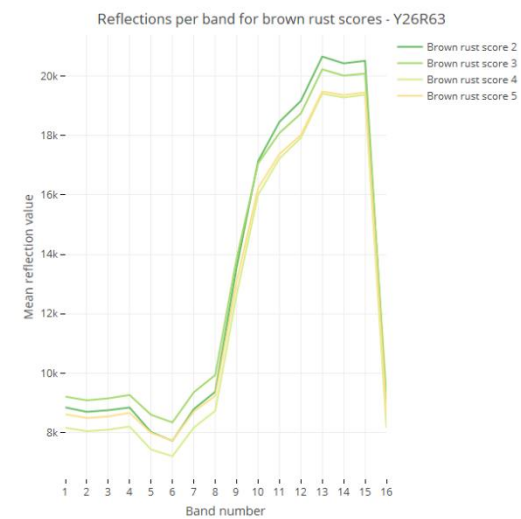


Figure G6 | Y26R63. Total plot count: 56.

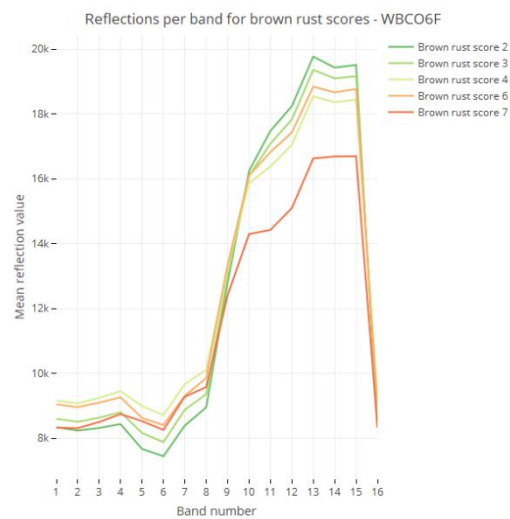


Figure G7 | WBCO6F. Total plot count: 35.

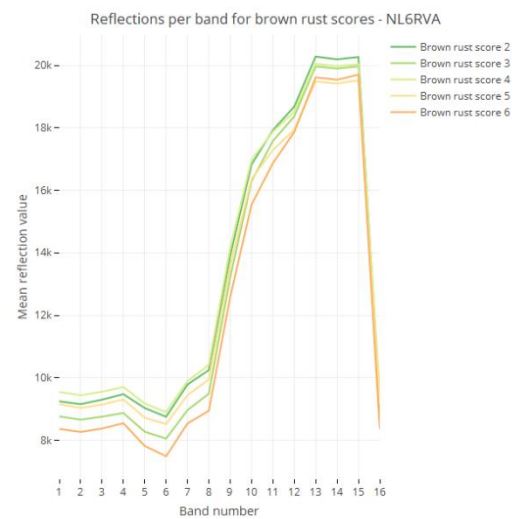


Figure G8 | NL6RVA. Total plot count: 34.

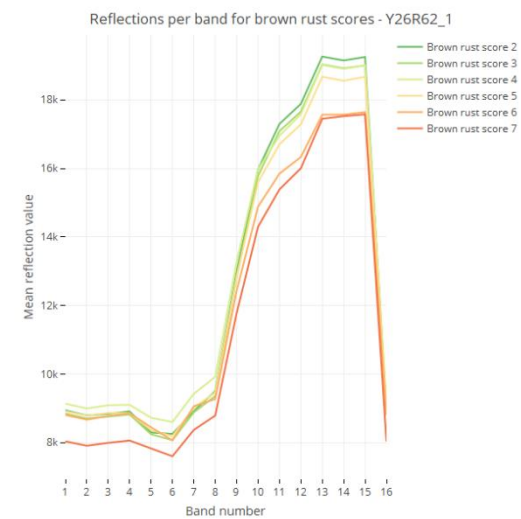


Figure G9 | Y26R62_1. Total plot count: 49.

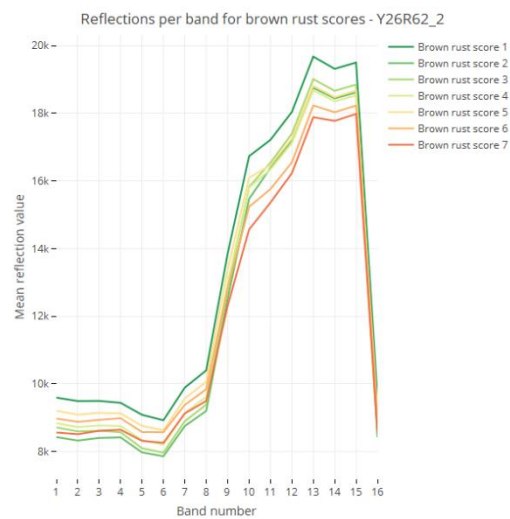


Figure G10 | Y26R62_2. Total plot count: 80.

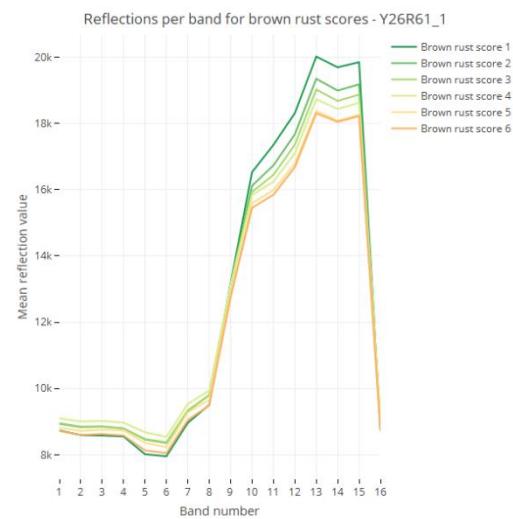


Figure G11 | Y26R61_1. Total plot count: 80.

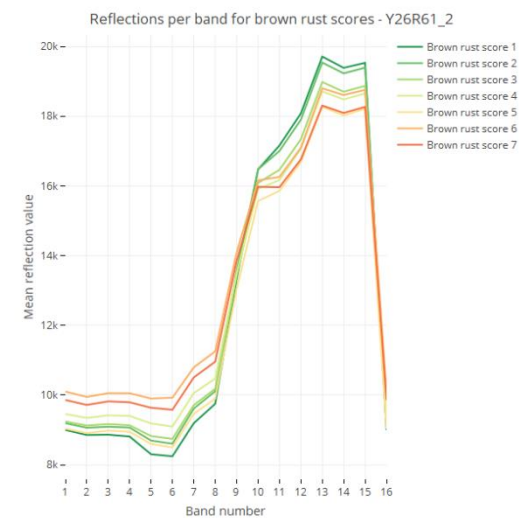


Figure G12 | Y26R61_2. Total plot count: 80.

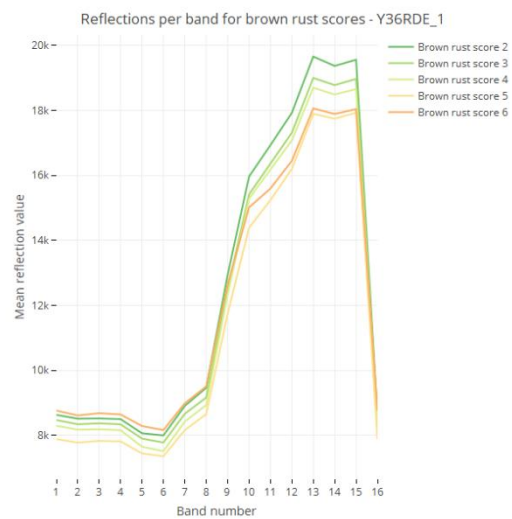


Figure G13 | Y36RDE_1. Total plot count: 94.

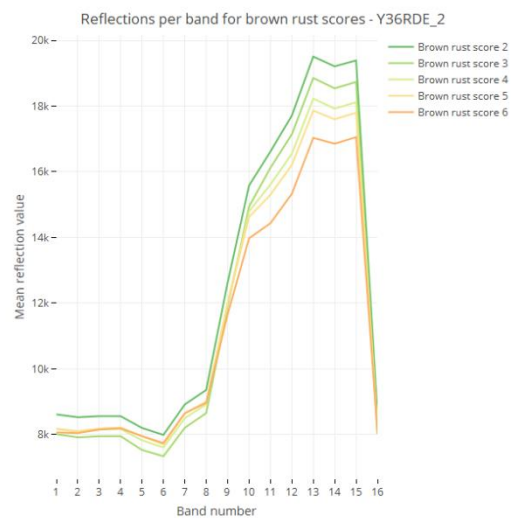


Figure G14 | Y36RDE_2. Total plot count: 92.

Table G1 – Counts of the brown rust scores per trial field.

Plot code			Plot code			Plot code			Plot code			Plot code			Plot code		
Y16RBY	Brown rust score	Plot count	Y3BEFR	Brown rust score	Plot count	WBCO6F	Brown rust score	Plot count	Y26R62_2	Brown rust score	Plot count	Y36RDE_1	Brown rust score	Plot count	Y36RDE_2	Brown rust score	Plot count
	1	0		1	1		1	0		1	4		1	0		1	0
	2	2		2	7		2	6		2	6		2	11		2	7
	3	13		3	15		3	16		3	40		3	56		3	47
	4	7		4	23		4	11		4	23		4	16		4	23
	5	6		5	19		5	0		5	4		5	10		5	12
	6	2		6	10		6	1		6	2		6	1		6	3
	7	5		7	4		7	1		7	1		7	0		7	0
Plot code	8	4	Plot code	8	0	Plot code	8	0	Plot code	8	0		8	0		8	0
Y16RDH	Brown rust score	Plot count	NL6RSU	Brown rust score	Plot count	NL16VRA	Brown rust score	Plot count	Y26R61_1	Brown rust score	Plot count						
	1	0		1	0		1	0		1	4						
	2	40		2	187		2	6		2	15						
	3	146		3	174		3	18		3	32						
	4	141		4	36		4	8		4	21						
	5	85		5	15		5	1		5	4						
	6	29		6	4		6	1		6	4						
	7	4		7	0		7	0		7	0						
Plot code	8	0	Plot code	8	0	Plot code	8	0	Plot code	8	0						
Y16RNL	Brown rust score	Plot count	Y26R63	Brown rust score	Plot count	NL16VRA	Brown rust score	Plot count	Y26R61_2	Brown rust score	Plot count						
	1	0		1	0		1	0		1	6						
	2	89		2	8		2	6		2	26						
	3	274		3	27		3	18		3	25						
	4	335		4	13		4	8		4	13						
	5	148		5	8		5	1		5	7						
	6	65		6	0		6	1		6	2						
	7	9		7	0		7	0		7	1						
	8	1		8	0		8	0		8	0						

Descriptive statistics

Table H1 | Overview and short explanation of the descriptive statistics calculated for sub-research question two.

1	Mean vector
<p>The mean vector matrix contains the overall means for each spectral band. (These values are required to do the translation in the PCA analysis – the shift of the origin to the centre of all pixel values.)</p> $\mu_k = \frac{\sum_{j=1}^n X_{kj}}{n} = \frac{\text{sum all pixel values}}{\text{number of pixel values}}$ <p style="text-align: right;">(5.1)</p>	
2	Variances
<p>The variances per spectral band are show the spread around the mean value. Note that the division is by $n-1$, this is done so to get an unbiased estimate of the variance.</p> $\sigma_k^2 = \frac{\sum_{j=1}^n (X_{kj} - \mu_k)^2}{(n - 1)} =$ $\frac{\text{difference of every pixel value with the band mean value}^2 \text{ added over all pixels}}{\text{number of pixel values} - 1}$ <p style="text-align: right;">(5.2)</p>	
3	Covariances
<p>How values in one band (k) vary with respect to the values in another spectral band (l).</p> $c_{kl} = \frac{\sum_{j=1}^n (X_{kj} - \mu_k)(X_{lj} - \mu_l)}{(n - 1)} =$ $\frac{\text{difference every pixel value with band } k \text{ mean value} * \text{difference every pixel value with band } l \text{ mean value, added over all pixels}}{\text{number of pixel values}}$ <p style="text-align: right;">(5.3)</p>	
4	Eigenvalues and -vectors
<p>Eigenvalues are simply the factor by which the eigenvector of the transformation – of the original pixel values into principal components – are stretched or squished. Eigenvalues are calculated by subtracting lambda's from the diagonal of the covariance matrix and subsequently taking the determinant (D) from that matrix. In a two-dimensional example, λ_1 and λ_2 are calculated solving the following equation:</p> $\begin{vmatrix} C_{11} - \lambda & C_{12} \\ C_{21} & C_{22} - \lambda \end{vmatrix} = 0$ $(C_{11} - \lambda)(C_{22} - \lambda) - C_{12} * C_{21} = 0$ <p style="text-align: right;">(5.4)</p> <p>(Note that the trace of this matrix, the summation of all the values along the diagonal – the variances – is equal to the trace of the covariance matrix; the total variation is still the same before dimensionality reduction is done.)</p>	

Subsequently, eigenvectors define the direction of the axes of the synthetic bands or principal components. The eigenvector b_i for each synthetic band and solution λ_i is calculated solving the equation below – the example is again of a two-dimensional case:

$$(C - \lambda_i * I) \underline{b}_i = 0$$

$$\begin{pmatrix} C_{11} - \lambda_1 & C_{12} \\ C_{21} & C_{22} - \lambda_1 \end{pmatrix} \begin{pmatrix} b_{11} \\ b_{12} \end{pmatrix} = \begin{pmatrix} 0 \\ 0 \end{pmatrix} \rightarrow b_1$$

$$\begin{pmatrix} C_{11} - \lambda_2 & C_{12} \\ C_{21} & C_{22} - \lambda_2 \end{pmatrix} \begin{pmatrix} b_{21} \\ b_{22} \end{pmatrix} = \begin{pmatrix} 0 \\ 0 \end{pmatrix} \rightarrow b_2$$

(5.5)

Note that I is the unity. Eigenvectors b_1 and b_2 are perpendicular to each other.

5

Correlation coefficients

A value between -1 and 1, representing an strong negative correlation and a strong positive correlation. Values around zero represent the lowest correlations possible – zero means no correlation at all.

$$\rho_{kl} = \frac{c_{kl}}{\sigma_k * \sigma_l} = \frac{\text{covariance}}{\text{standard deviation band } k * \text{standard deviation band } l}$$

(5.6)

6

Residuals

In regression, residuals – also known as prediction errors – are the differences between the observed values of the dependent variable and the predicted variable. The residuals are measured in order to determine how far the values are from the regression line; each value has a residual. Both the mean and the sum of the residuals equals zero. The residual is calculated as follows:

$$e_i = y_i - \hat{y}_i = \text{observed value} - \text{predicted value}$$

(5.7)

	Band 1	Band 2	Band 3	Band 4	Band 5	Band 6	Band 7	Band 8	Band 9	Band 10	Band 11	Band 12	Band 13	Band 14	Band 15	Band 16
Band 1	0,00021	0,00021	0,00021	0,00022	0,00024	0,00024	0,00025	0,00025	0,00025	0,00020	0,00014	0,00013	0,00013	0,00012	0,00012	0,00021
Band 2	0,00021	0,00021	0,00021	0,00022	0,00024	0,00024	0,00025	0,00025	0,00025	0,00020	0,00013	0,00012	0,00012	0,00012	0,00011	0,00021
Band 3	0,00021	0,00021	0,00022	0,00022	0,00025	0,00025	0,00026	0,00026	0,00025	0,00020	0,00013	0,00012	0,00011	0,00011	0,00011	0,00021
Band 4	0,00022	0,00022	0,00022	0,00023	0,00026	0,00025	0,00026	0,00026	0,00026	0,00020	0,00013	0,00012	0,00011	0,00011	0,00011	0,00022
Band 5	0,00024	0,00024	0,00025	0,00026	0,00030	0,00030	0,00031	0,00030	0,00027	0,00019	0,00010	0,00008	0,00008	0,00008	0,00008	0,00024
Band 6	0,00024	0,00024	0,00025	0,00025	0,00030	0,00030	0,00031	0,00031	0,00027	0,00019	0,00009	0,00008	0,00008	0,00008	0,00008	0,00024
Band 7	0,00025	0,00025	0,00026	0,00026	0,00031	0,00031	0,00032	0,00032	0,00029	0,00021	0,00011	0,00010	0,00010	0,00010	0,00009	0,00025
Band 8	0,00025	0,00025	0,00026	0,00026	0,00030	0,00031	0,00032	0,00032	0,00030	0,00022	0,00013	0,00012	0,00012	0,00012	0,00011	0,00025
Band 9	0,00025	0,00025	0,00025	0,00026	0,00027	0,00027	0,00029	0,00030	0,00034	0,00031	0,00025	0,00024	0,00024	0,00023	0,00023	0,00025
Band 10	0,00020	0,00020	0,00020	0,00020	0,00019	0,00019	0,00021	0,00022	0,00031	0,00037	0,00036	0,00035	0,00035	0,00034	0,00033	0,00020
Band 11	0,00014	0,00013	0,00013	0,00013	0,00010	0,00009	0,00011	0,00013	0,00025	0,00036	0,00042	0,00041	0,00041	0,00039	0,00038	0,00014
Band 12	0,00013	0,00012	0,00012	0,00012	0,00008	0,00008	0,00010	0,00012	0,00024	0,00035	0,00041	0,00041	0,00041	0,00039	0,00039	0,00013
Band 13	0,00013	0,00012	0,00011	0,00011	0,00008	0,00008	0,00010	0,00012	0,00024	0,00035	0,00041	0,00041	0,00042	0,00040	0,00039	0,00013
Band 14	0,00012	0,00012	0,00011	0,00011	0,00008	0,00008	0,00010	0,00012	0,00023	0,00034	0,00039	0,00039	0,00040	0,00039	0,00038	0,00012
Band 15	0,00012	0,00011	0,00011	0,00011	0,00008	0,00008	0,00009	0,00011	0,00023	0,00033	0,00038	0,00039	0,00039	0,00038	0,00037	0,00012
Band 16	0,00021	0,00021	0,00021	0,00022	0,00024	0,00024	0,00025	0,00025	0,00025	0,00020	0,00014	0,00013	0,00013	0,00012	0,00012	0,00021

Figure H1 | Matrix with the covariances and variances – on the diagonal – of the mean reflections of the 16 bands.

Eigenvalues	Vector 1	Vector 2	Vector 3	Vector 4	Vector 5	Vector 6	Vector 7	Vector 8	Vector 9	Vector 10	Vector 11	Vector 12	Vector 13	Vector 14	Vector 15	Vector 16
11,779894	-0,281	-0,125	0,215	0,166	0,407	-0,119	0,009	-0,024	0,060	0,028	0,052	0,312	0,170	0,132	0,006	0,707
4,017957	-0,279	-0,138	0,153	0,153	0,295	-0,024	-0,077	-0,068	-0,163	-0,173	0,092	-0,382	-0,384	-0,625	-0,095	0,000
0,095694	-0,277	-0,154	0,080	0,214	0,029	0,235	-0,008	0,063	-0,095	0,132	-0,208	-0,638	0,090	0,481	0,268	0,000
0,053365	-0,275	-0,155	0,051	0,317	-0,371	0,605	0,030	0,292	0,036	0,173	-0,013	0,326	-0,096	-0,157	-0,191	0,000
0,019205	-0,259	-0,221	-0,264	0,166	-0,336	-0,040	-0,157	-0,352	-0,096	-0,646	0,222	0,093	0,102	0,144	0,088	0,000
0,016489	-0,257	-0,226	-0,316	-0,075	-0,121	-0,435	0,281	0,343	-0,345	0,126	-0,026	-0,093	0,176	0,025	-0,447	0,000
0,009204	-0,263	-0,208	-0,248	-0,164	-0,105	-0,071	-0,238	-0,570	0,280	0,520	-0,175	-0,007	-0,013	-0,109	-0,098	0,000
0,003490	-0,270	-0,180	-0,165	-0,301	-0,072	-0,183	0,045	0,357	0,107	0,045	0,021	0,172	-0,312	-0,078	0,679	0,000
0,001392	-0,288	0,001	0,200	-0,542	0,003	0,187	0,248	0,063	0,491	-0,355	-0,101	-0,152	0,106	0,025	-0,265	0,000
0,000988	-0,258	0,217	0,394	-0,470	-0,153	0,094	-0,278	-0,103	-0,570	0,124	0,174	0,097	0,001	0,101	-0,013	0,000
0,000853	-0,200	0,356	0,304	0,238	-0,368	-0,259	0,450	-0,212	0,011	0,050	-0,192	-0,015	0,239	-0,273	0,251	0,000
0,000490	-0,193	0,372	0,100	0,216	-0,161	-0,333	-0,165	0,083	0,251	-0,007	0,033	-0,003	-0,576	0,367	-0,259	0,000
0,000420	-0,191	0,374	-0,180	0,070	0,018	-0,063	-0,594	0,349	0,165	-0,053	-0,077	-0,099	0,452	-0,240	0,036	0,000
0,000343	-0,192	0,370	-0,350	0,007	0,164	0,210	0,299	-0,084	0,075	0,197	0,687	-0,123	0,047	0,027	0,047	0,000
0,000218	-0,191	0,371	-0,406	-0,041	0,296	0,225	0,147	-0,127	-0,274	-0,168	-0,553	0,203	-0,178	0,043	-0,002	0,000
0,000000	-0,281	-0,125	0,215	0,166	0,407	-0,119	0,009	-0,024	0,060	0,028	0,052	0,312	0,170	0,132	0,006	-0,707

Figure H2 | Eigenvalues and eigenvectors of the mean reflections of the 16 bands.

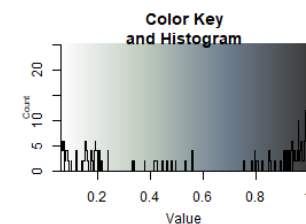
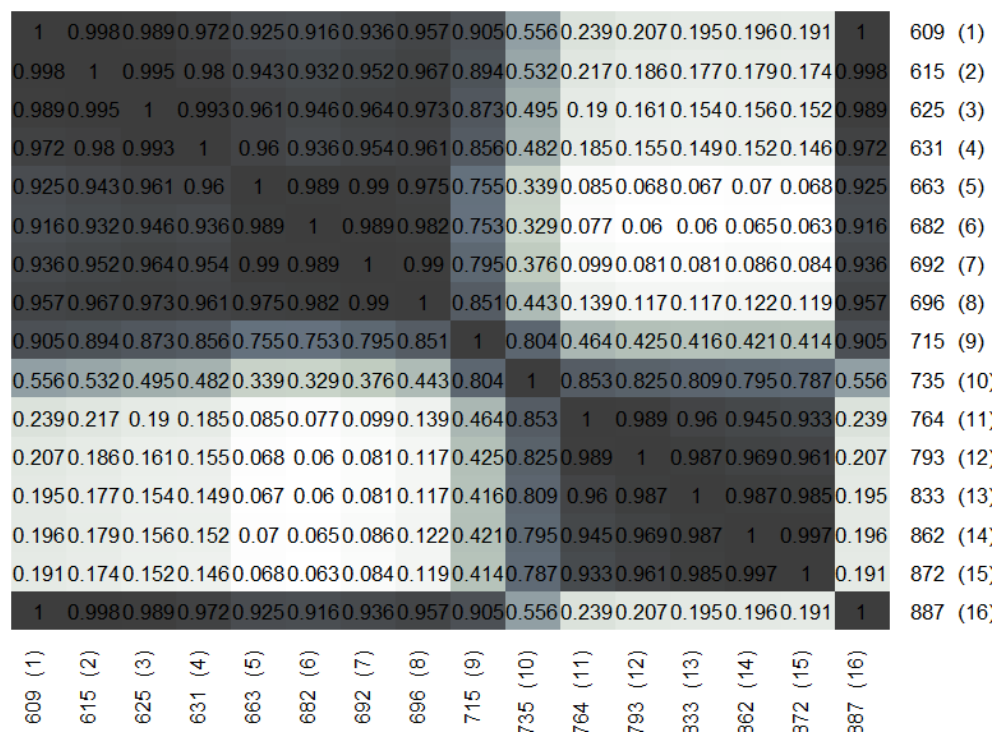


Figure H3 | Lambda-lambda plot of the mean reflections in the 16 bands.

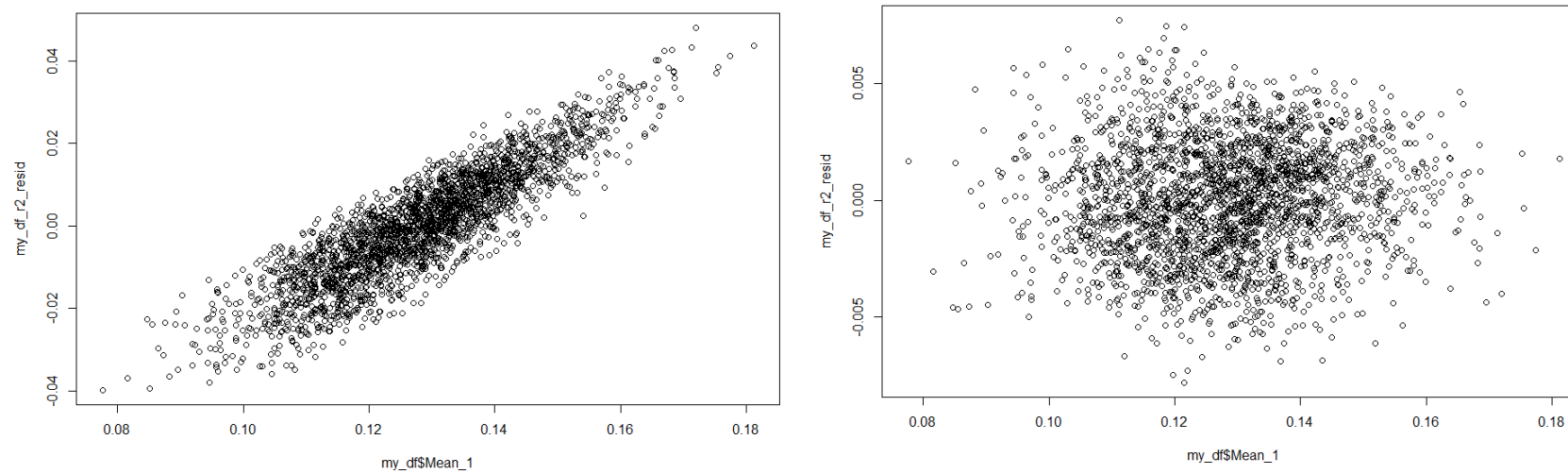


Figure H4 | Residual plots of bands 2 ad 13 (left) and bands 13 and 15 (left).

ANNEX I

Correlation matrices

Correlation plots of the correlations between the normalized difference (figure I1), orthogonal (figure I2) and soil-adjusted (figure I3) index values and the brown rust scores from the validation dataset:

Vegetation index (band X, band Y) ~ Brown rust score

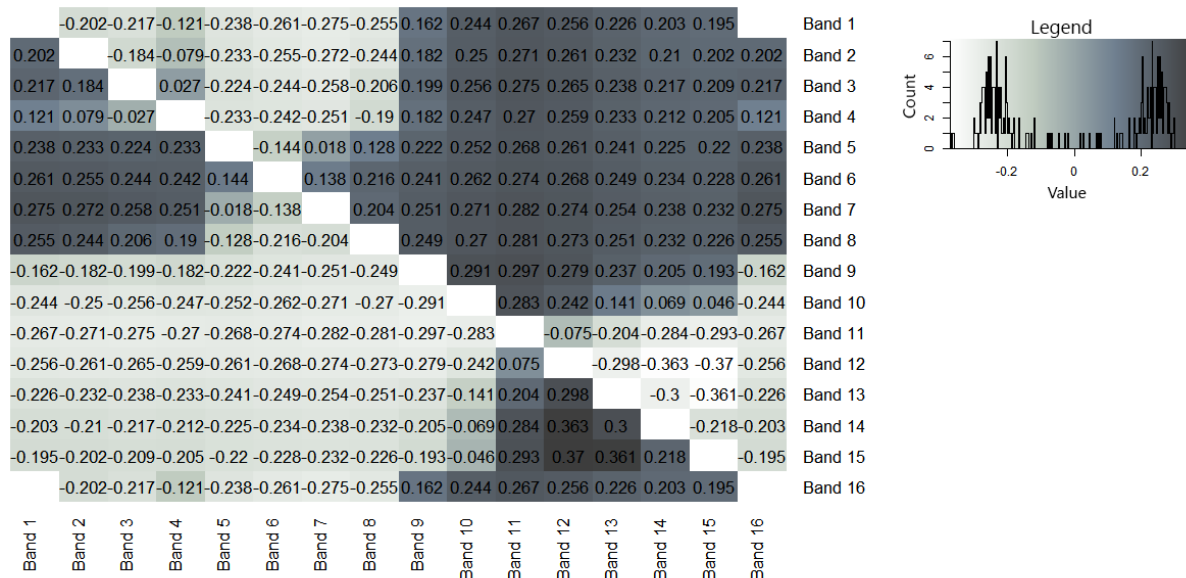


Figure I1 | Correlation plot showing the Pearson correlation values of the normalized difference (ND) index values ~ brown rust scores. This plot is created using the 16 band hyperspectral data retrieved at the 14th of June 2017. The axes are provided with the narrowband wavelengths and band numbers. The legend shows the spreading of the correlation values. Empty values indicate there is no correlation. The strongest correlation with the brown rust scores is achieved when using bands 12 and 15 for calculating the index value; the NIR wavelengths of 793 and 872 nm are assigned to these bands – see table 4.

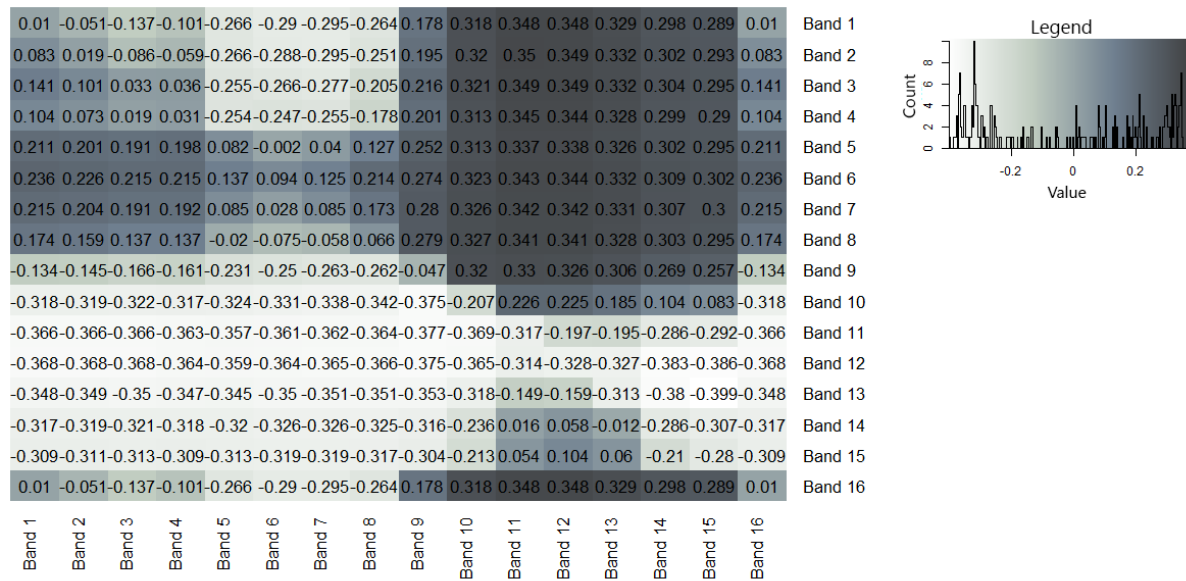


Figure 12 | Correlation plot showing the Pearson correlation values of the orthogonal index values ~ brown rust scores. This plot is created using the 16 band hyperspectral data retrieved at the 14th of June 2017. The axes are provided with the narrowband wavelengths and band numbers. The legend shows the spreading of the correlation values. The legend shows the spreading of the correlation values. The strongest correlation with the brown rust scores is achieved when using bands 2/3 and 11/12 for calculating the index value; the red and NIR wavelengths of 615/625 and 764/793 nm are assigned to these bands – see table 4.

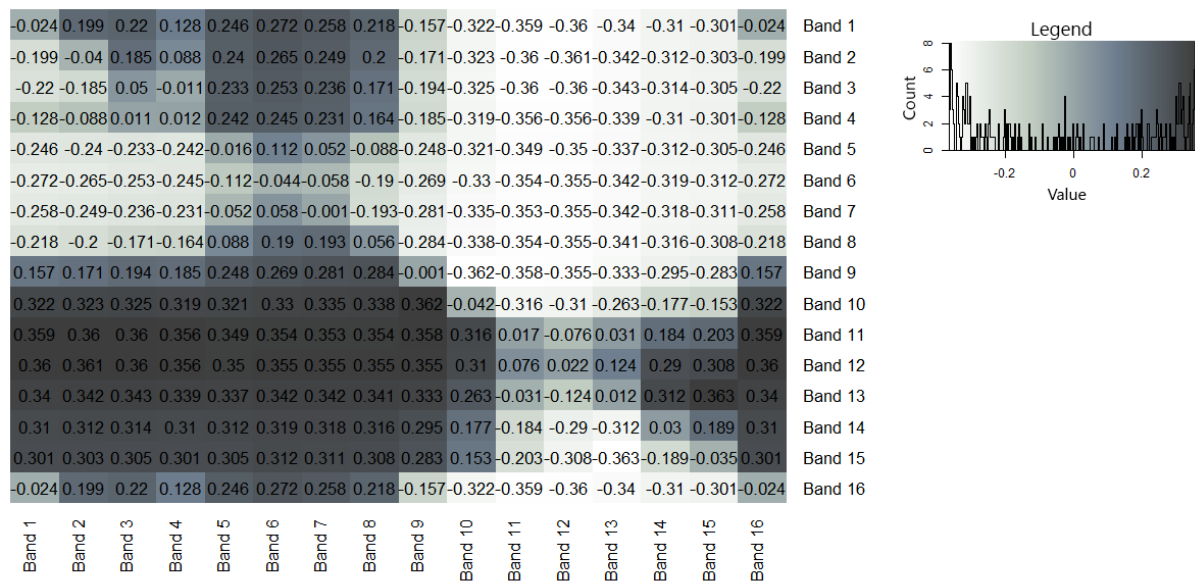


Figure 13 | Correlation plot showing the Pearson correlation values of the soil-adjusted index values ~ brown rust scores. This plot is created using the 16 band hyperspectral data retrieved at the 14th of June 2017. The axes are provided with the narrowband wavelengths and band numbers. The legend shows the spreading of the correlation values. The legend shows the spreading of the correlation values. The strongest correlation with the brown rust scores is achieved when using bands 9 and 10 for calculating the index value; the NIR wavelengths of 715 and 735 nm are assigned to these bands – see table 4.

ANNEX J

Mean reflections of the hyperspectral datasets of flight one and flight two

In order to perceive a first impression of the comparison between the mean reflectances per band and brown rust score of the different flight data, the mean reflectances of both flights are shown in the graphs of figures J1 and J2. Noted should be that during the second flight, merely the left half of the EV and MV fields – see figure F1 of Annex F – were captured by the sensor. In other words, the statistical data of this flight is based upon half of the amount of winter barley plots from the first flight.

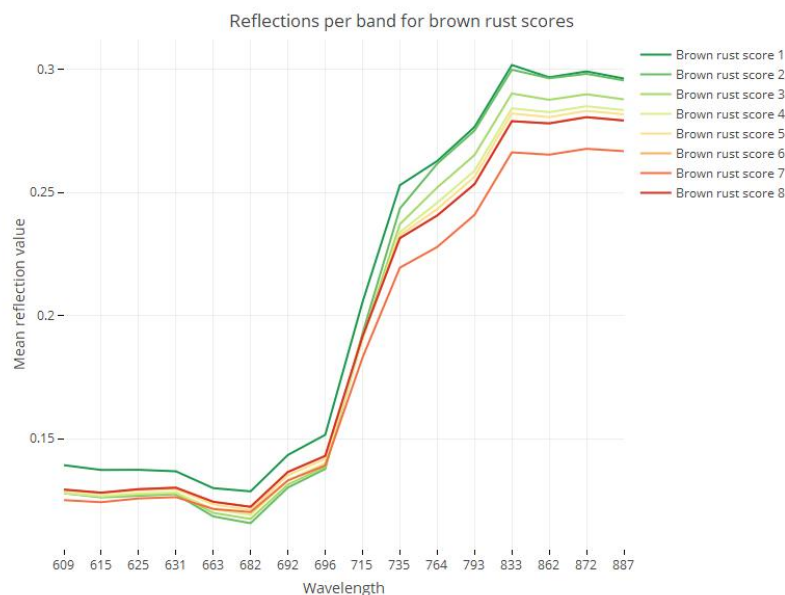


Figure J1 | Mean reflections per band and brown rust score, retrieved during the flight of the 14th of June 2017.

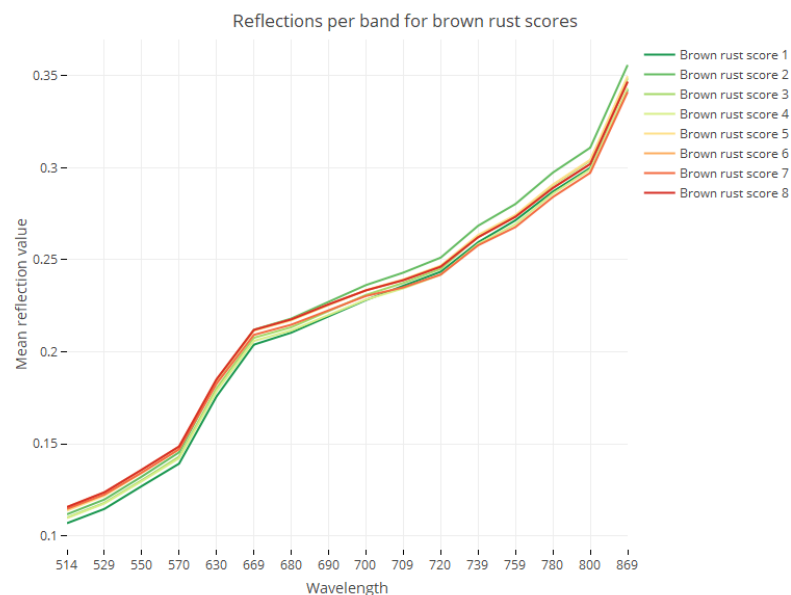


Figure J2 | Mean reflections per band and brown rust score, retrieved during the flight of the 26th of June 2017.

ANNEX K

Scatterplots of the vegetation index values against the brown rust scores.

The regression lines are included in the graphs. An overview map of plots that are included in the graph is given – plots included in the calculations are marked in orange.

Scatterplots which include all 2637 winter barley plots

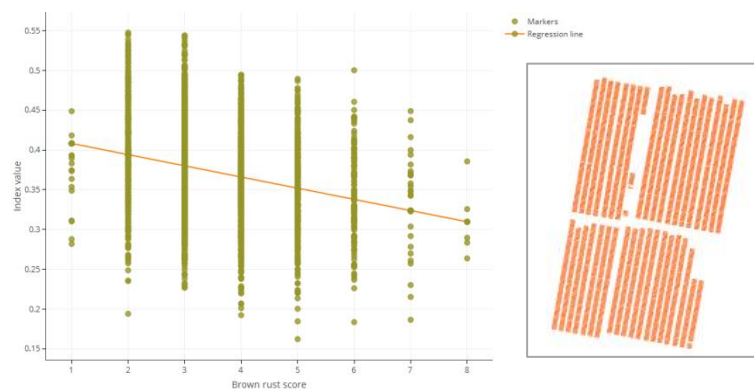


Figure I1 | Scatterplot of the ND 793/663 index values against the brown rust scores of all plots.

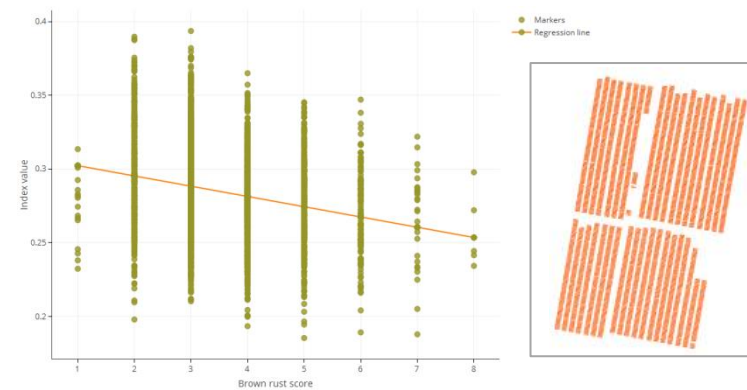


Figure I3 | Scatterplot of the NDVI red edge values against the brown rust scores of all plots.

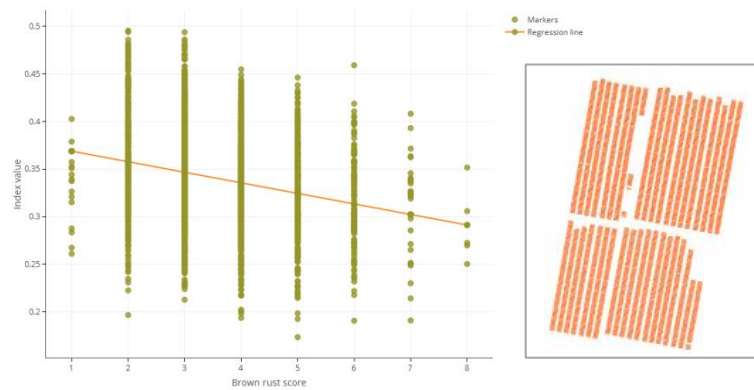


Figure I2 | Scatterplot of the NDVI values against the brown rust scores of all plots.

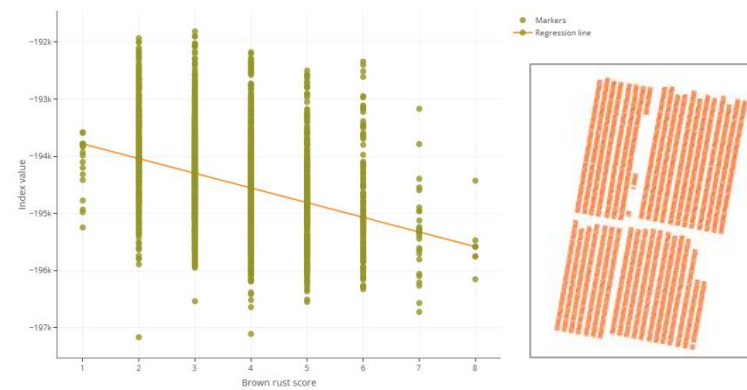


Figure I4 | Scatterplot of the PVI values against the brown rust scores of all plots.

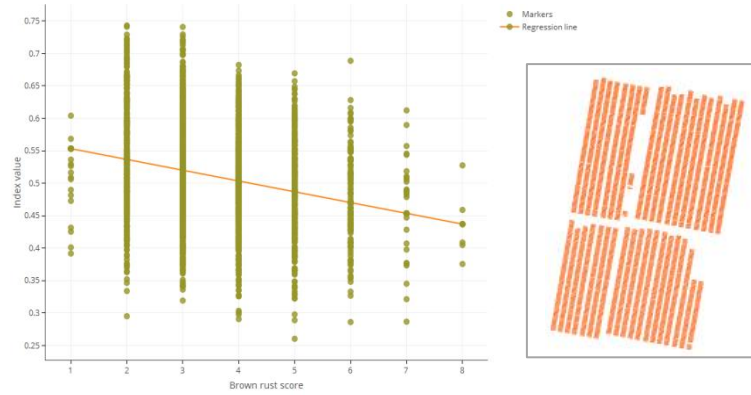


Figure I5 | Scatterplot of the SAVI values against the brown rust scores of all plots.

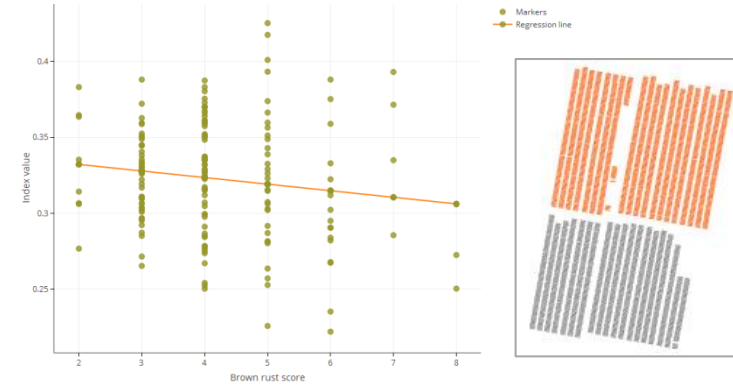


Figure I7 | Scatterplot of the NDVI against the brown rust scores of all plots scored on lodging.

Scatterplots which include the plots scored on lodging

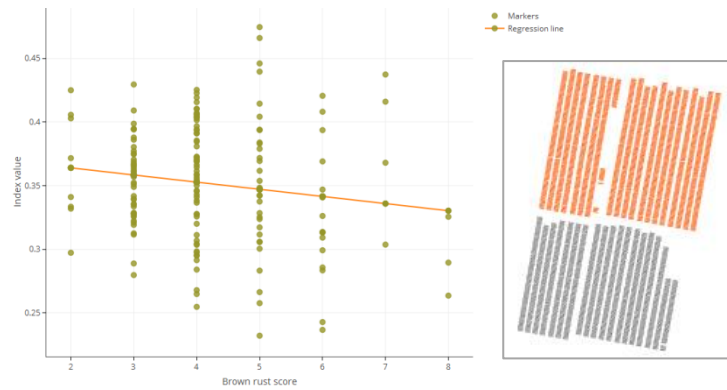


Figure I6 | Scatterplot of the ND 793/663 index against the brown rust scores of all plots scored on lodging.

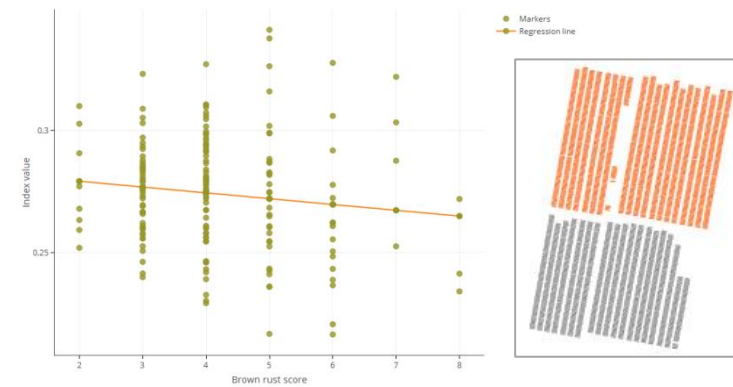


Figure I8 | Scatterplot of the NDVI red edge against the brown rust scores of all plots scored on lodging.

Scatterplots which include all plots scored 1 for lodging

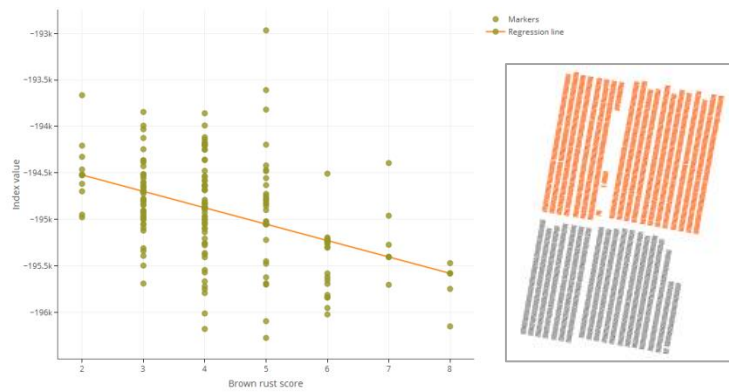


Figure I9 | Scatterplot of the PVI against the brown rust scores of all plots scored on lodging.

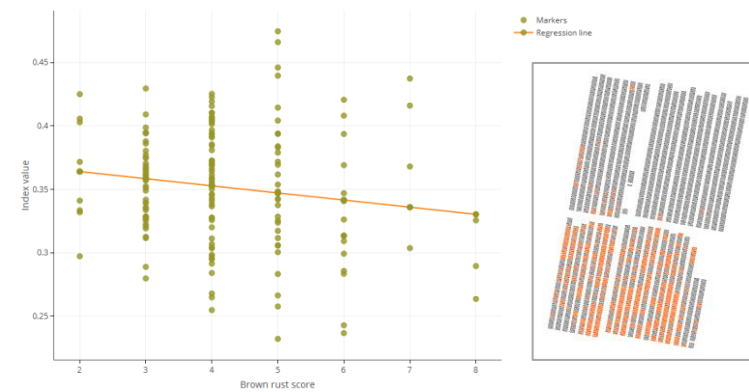


Figure I11 | Scatterplot of the SAVI against the brown rust scores of all plots scored 1 for lodging.

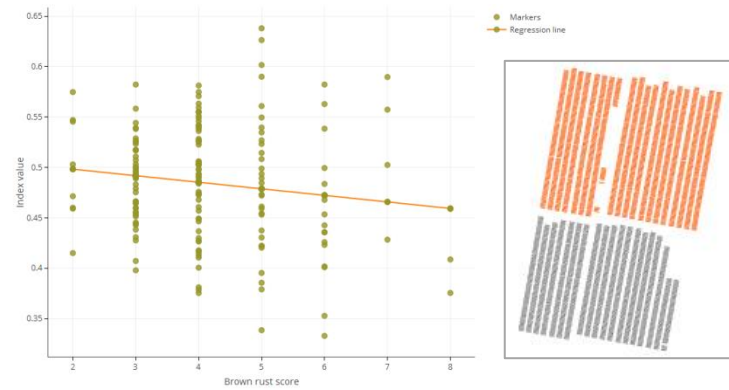


Figure I10 | Scatterplot of the SAVI against the brown rust scores of all plots scored on lodging.

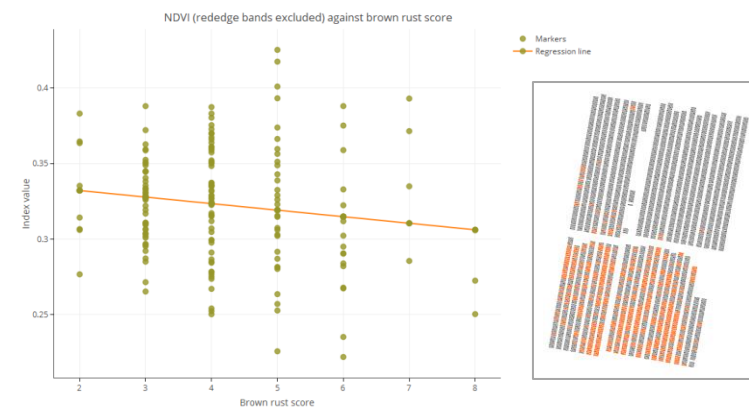


Figure I12 | Scatterplot of the NDVI against the brown rust scores of all plots scored 1 for lodging.

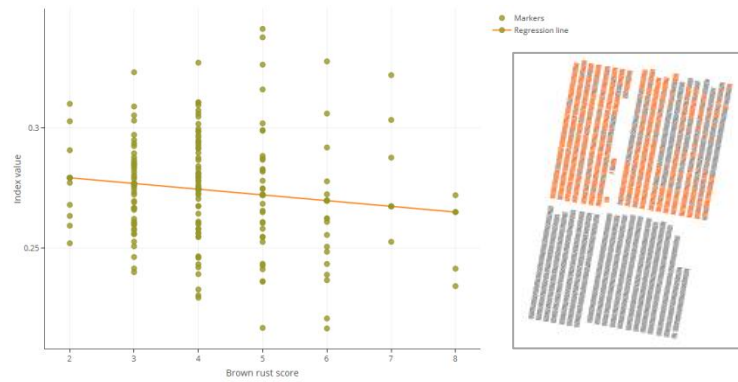


Figure I13 | Scatterplot of the NDVI RedEdge against the brown rust scores of all plots scored 1 for lodging.

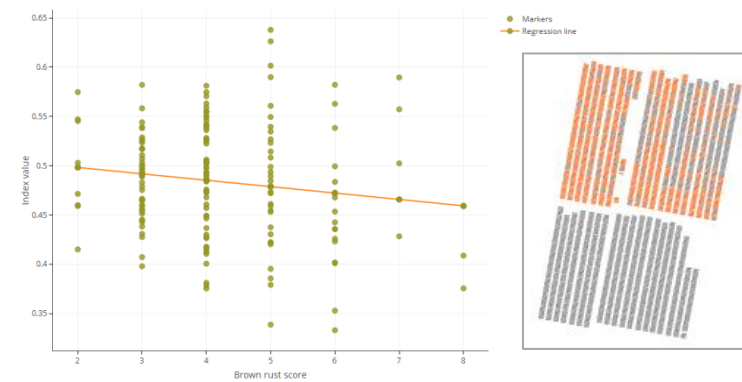


Figure I15 | Scatterplot of the SAVI against the brown rust scores of all plots scored 1 for lodging.

Scatterplots which include all plots scored 1 for brackling

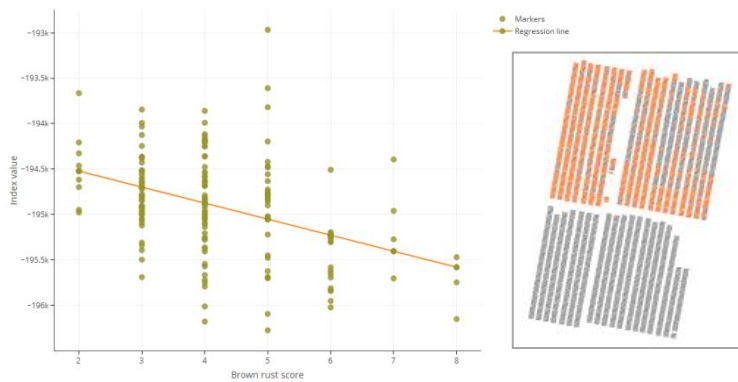


Figure I14 | Scatterplot of the PVI against the brown rust scores of all plots scored 1 for lodging.

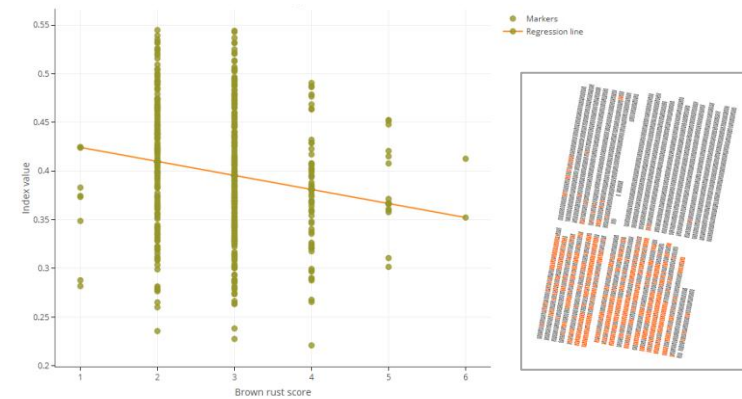


Figure I16 | Scatterplot of the ND 793/663 index against the brown rust scores of all plots scored 1 for brackling.

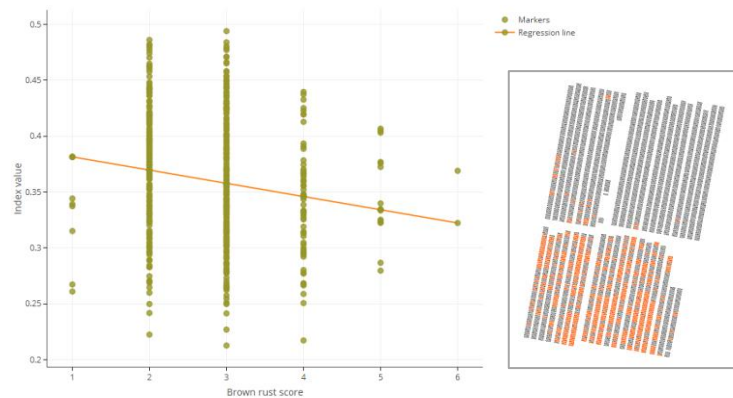


Figure I17 | Scatterplot of the NDVI against the brown rust scores of all plots scored 1 for brackling.

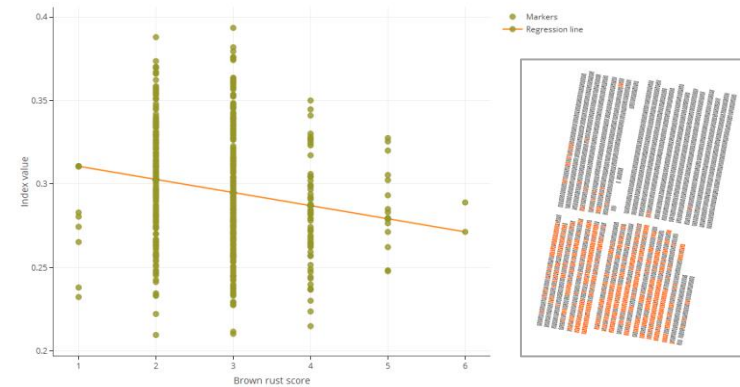


Figure I18 | Scatterplot of the NDVI RedEdge against the brown rust scores of all plots scored 1 for brackling.

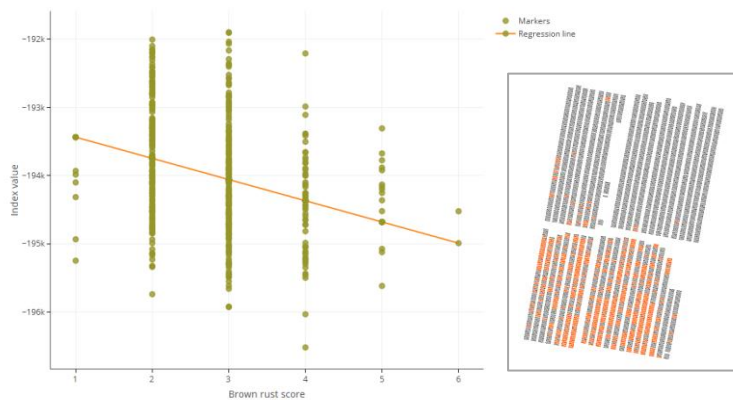


Figure I19 | Scatterplot of the PVI against the brown rust scores of all plots scored 1 for brackling.

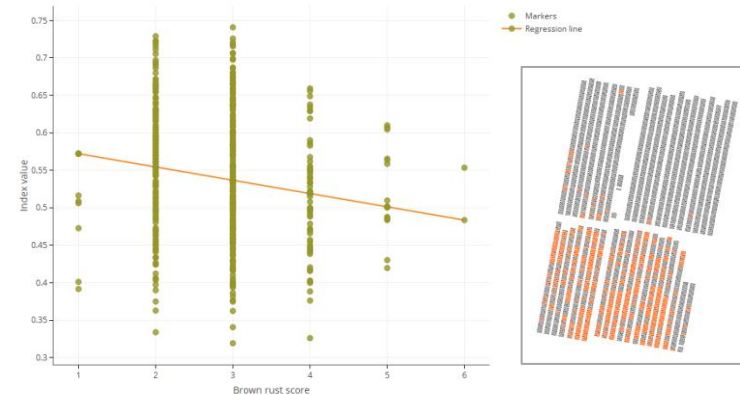


Figure I20 | Scatterplot of the PVI against the brown rust scores of all plots scored 1 for brackling.

Scatterplots which include all plots scored 1 for both lodging and brackling

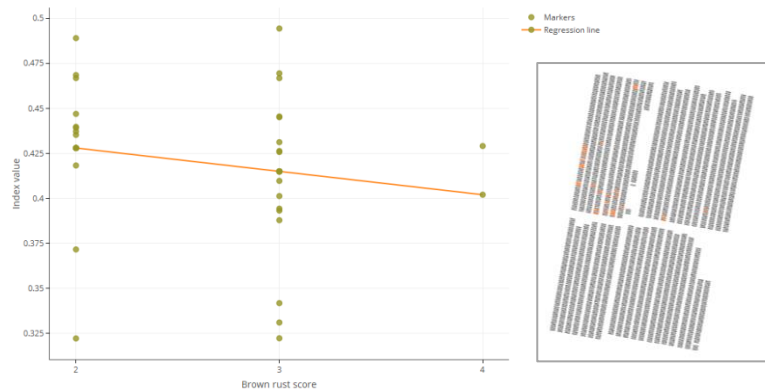


Figure I21 | Scatterplot of the ND 793/663 index against the brown rust scores of all plots scored 1 for both lodging and brackling.

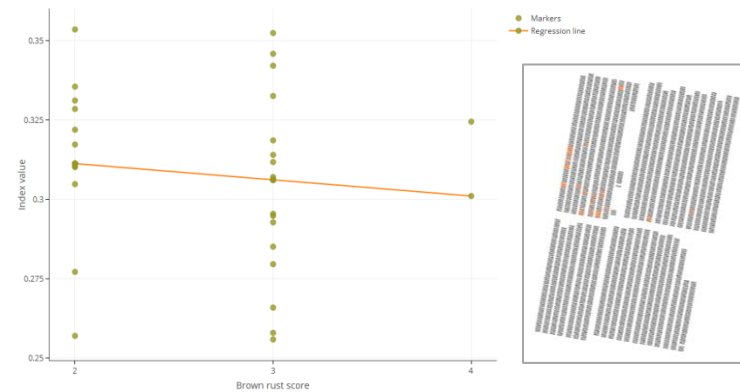


Figure I23 | Scatterplot of the NDVI RedEdge against the brown rust scores of all plots scored 1 on both lodging and brackling.

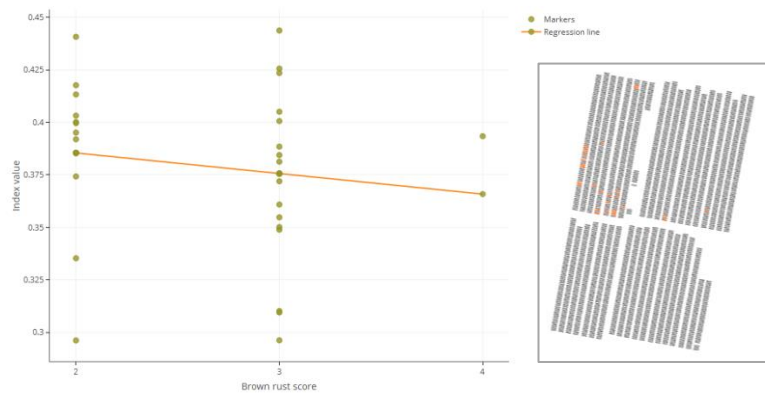


Figure I22 | Scatterplot of the NDVI against the brown rust scores of all plots scored 1 on both lodging and brackling.

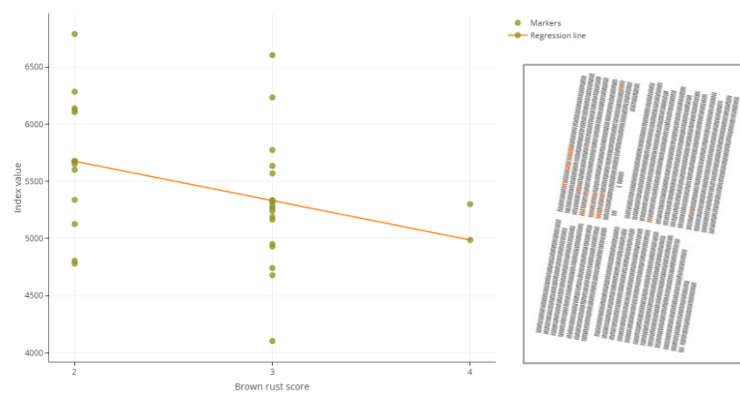


Figure I24 | Scatterplot of the PVI against the brown rust scores of all plots scored 1 on both lodging and brackling.

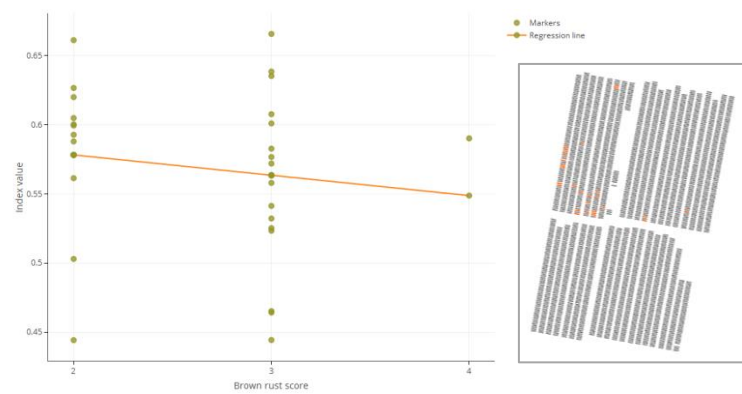
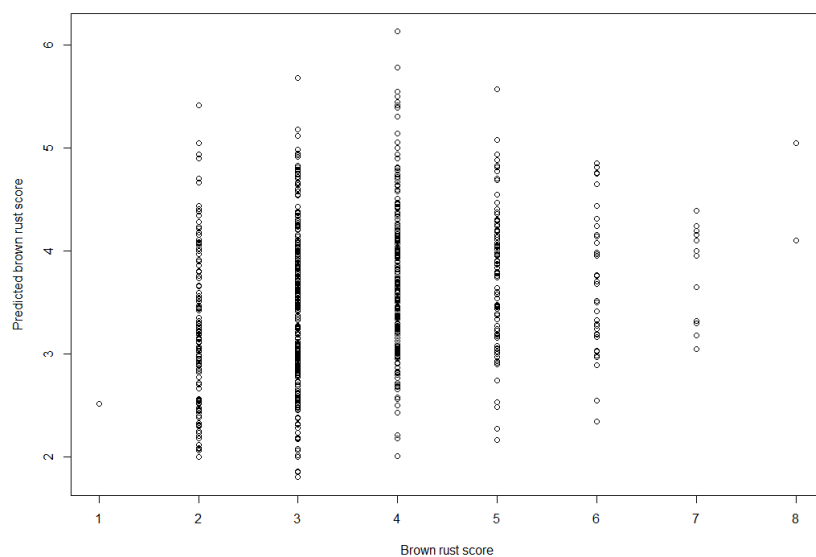


Figure I25 | Scatterplot of the SAVI against the brown rust scores of all plots scored 1 on both lodging and brackling.

ANNEX L

Correlations predicted brown rust scores ~ validation brown rust scores; one predictor

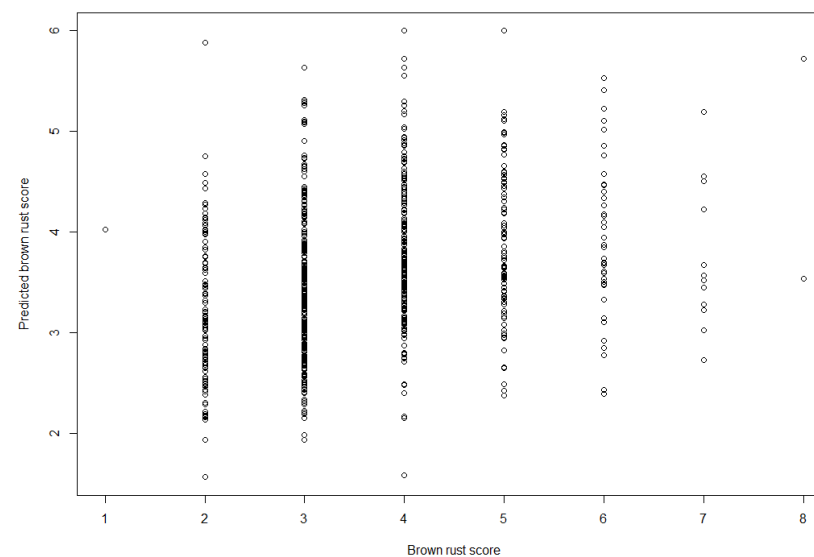
Figures L1-L3 show the correlations between the predicted brown rust scores resulting from a random forest model using the caret() package in R. For each of the three models, a summary is given below the resulting scatterplot and Pearson correlation value. The data was divided in a test set of 757 and a training set of 1774 samples – each feature represents a winter barley plot. The resampling method was a 5 fold, cross-validation. The predictor used for each model is the index type as shown in the first column, calculated according to the formula's as indicated in figure 11.



Resampling results:

RMSE	Rsquared	MAE
1.240401	0.04410295	0.9712456

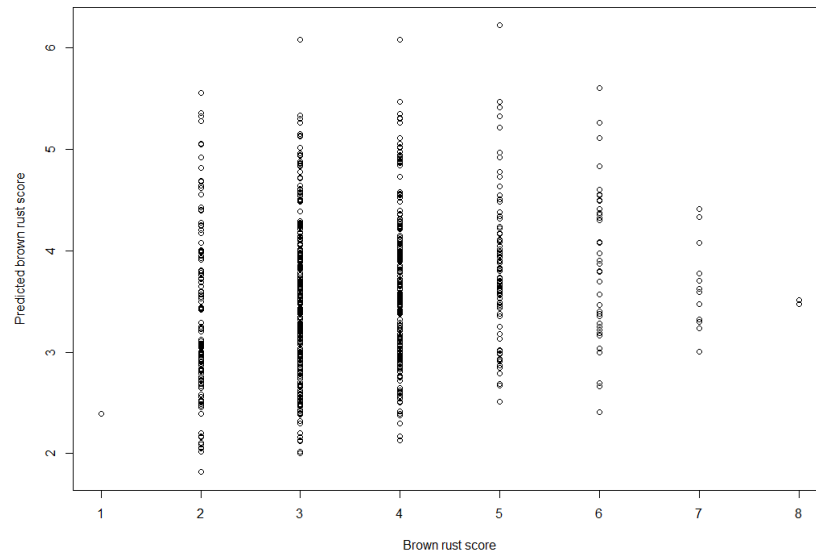
Figure L1 | Normalized difference. Pearson correlation coefficient: 0.2487714.



Resampling results:

RMSE	Rsquared	MAE
1.232706	0.05003601	0.9690183

Figure L2 | Orthogonal. Pearson correlation coefficient: 0.3232609.

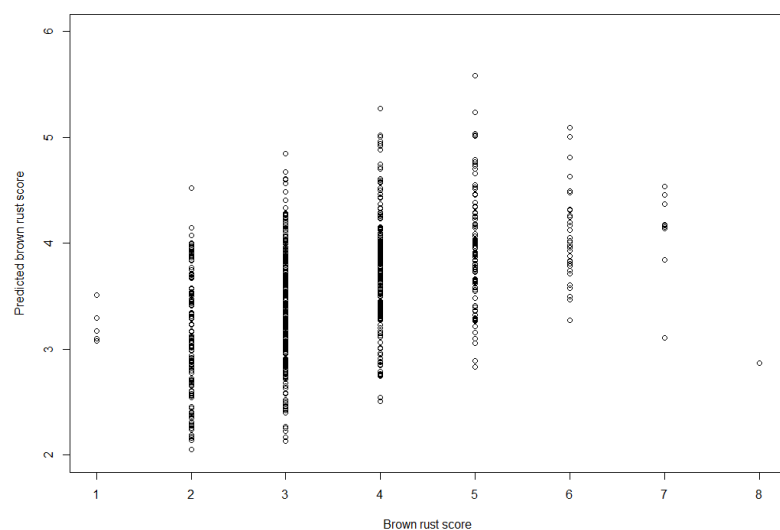


Resampling results:		
RMSE	Rsquared	MAE
1.240401	0.04410295	0.9712456

Figure L3 | Soil-adjusted. Pearson correlation coefficient: 0.1979202

Correlations predicted brown rust scores ~ validation brown rust scores; 30 predictors

Figures M1-M3 show the correlations between the predicted brown rust scores resulting from a random forest model using the caret() package in R. For each of the three models, a summary is given below the resulting scatterplot and Pearson correlation value. The data was divided in a test set of 757 and a training set of 1774 samples – each feature represents a winter barley plot. The resampling method was a 5 fold, cross-validation. The 30 predictors are the index values of the 30 band combinations showing the best R^2 values – for all R^2 values see figures 24-26.

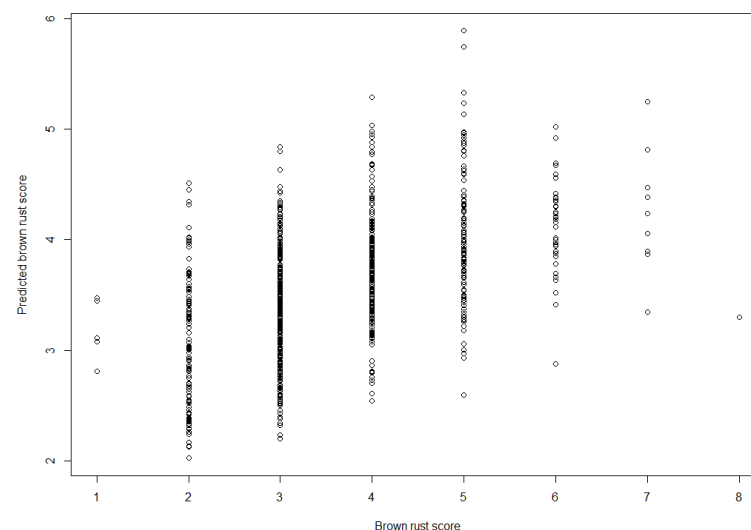


Resampling results across tuning parameters:

mtry	RMSE	Rsquared	MAE
3	1.018094	0.2339434	0.7931552
13	1.017062	0.2367557	0.7920206
16	1.016369	0.2378079	0.7914480

RMSE was used to select the optimal model using the smallest value.
The final value used for the model was mtry = 16.

Figure M1 | Normalized difference. Pearson correlation coefficient: 0.4736703.

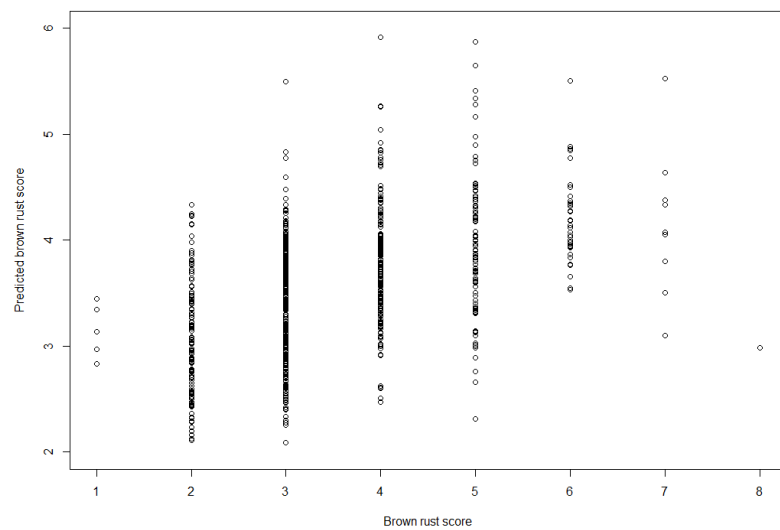


Resampling results across tuning parameters:

mtry	RMSE	Rsquared	MAE
18	0.9936212	0.2710060	0.7724441
22	0.9956034	0.2684926	0.7735685
29	0.9968648	0.2668320	0.7744089

RMSE was used to select the optimal model using the smallest value.
The final value used for the model was mtry = 18.

Figure M2 | Orthogonal. Pearson correlation coefficient: 0.5166168.



Resampling results across tuning parameters:

mtry	RMSE	Rsquared	MAE
11	1.020113	0.2358295	0.7979662
13	1.020466	0.2356145	0.7977443
16	1.021460	0.2347564	0.7977621

RMSE was used to select the optimal model using the smallest value.
The final value used for the model was mtry = 11.

Figure M3 | Soil-adjusted. Pearson correlation coefficient: 0.4780202.

Workflow of the MCMS study

Table N1 | Workflow of the MCMS 2007-2009 rice biomass study by Aasen, Gnyp et al. (2014).

Step	Activity	Phase
1	Export datasets (a) SGSY; 9 datasets (b) SGAY; 3 datasets (c) AGAY; 1 dataset	Correlation Matrix (CM) computation
2	Correct detector offset for all datasets	Correlation Matrix (CM) computation
3	Removal water absorption bands (1330-1480 nm)	Correlation Matrix (CM) computation
4	Restriction of spectral range to a range that is available for all datasets with low signal to noise ratio (in this case 400-1700 nm)	Correlation Matrix (CM) computation
5	(Optionally) set minimum R^2 level	Correlation Matrix (CM) computation
6	(Optionally) set significance level	Correlation Matrix (CM) computation
7	Specify SVI type (ratio, difference, normalized difference)	Correlation Matrix (CM) computation
8	Automatic processing CMs -	HyperCor
9	Import CMs for SGSY (three for each year) into MATLAB®, stack data into a multi-dimensional array	Multi-Correlation Matric Strategy approach
10	Apply an average function as MCMS function (fMCMS) on the datasets to obtain a matrix containing the mean correlation values for all band combinations	Multi-Correlation Matric Strategy approach
11	Extract band combination of the highest mean correlation value (best band combination)	Multi-Correlation Matric Strategy approach
12	Use extracted bands with the SGAY dataset to develop a (both linear and exponential) prediction model (in Microsoft™ Excel 2013) – repeat procedure for all growth stages	Multi-Correlation Matric Strategy approach
13	For model development for the entire growing period, step 12 is applied using the AGAY dataset instead of the SGAY dataset	Multi-Correlation Matric Strategy approach
14	Use CMs of SGAY dataset , extract band combination with highest coefficient of determination for each grow stage	Direct approach
15	Use the extracted band combinations together with SGAY data to develop a linear and exponential model	Direct approach
16	To develop the linear and exponential models across all growth stages, steps 14 and 15 are repeated with the CM of the AGAY dataset	Direct approach
17	Derive the best band combination by calculating the difference between the MCMS and direct approach	Band combination selection
18	Validate models from both the MCMS and direct approach, all models are applied on an independent dataset (in this case from the years 2011 and 2012)	Validation